POLITECNICO DI MILANO
Master of Science in Aeronautical Engineering
Department of Aerospace Sciences and Technologies

ACTIVE HEADREST FOR PROPELLER-INDUCED CABIN NOISE

Thesis Supervisor:
Prof. Gianluca Ghiringhelli

Candidate:
Edoardo Pareti, ID 898411

Academic Year: 2019-2020

A Germano

Ringraziamenti

I miei ringraziamenti vanno in primis alla mia famiglia, quindi ai miei genitori Luigia e Stefano, a mia zia Ernesta ed ai miei nonni Giovanni e Rosetta, ma anche a chi non è potuto esserci, ossia mio zio Germano. Non potrò mai ringraziarlo abbastanza di tutto ciò che ha fatto ed è stato per me. Durante questo percorso, altre persone sono state di fondamentale importanza e vorrei qui ringraziarle: Silvia, Francesca, Francesco, Federico, Eugenio, Luca, Michele e Andrea sono state le mie spalle durante questa esperienza e mi auguro anche in futuro. Infine, vorrei ringraziare tutti i Professori ed Assistenti di Laboratorio che mi hanno aiutato nella realizzazione della Tesi, in particolare il Prof. Ghiringhelli, che mi ha lasciato totale autonomia di scelta ed azione rendendo sicuramente molto più stimolante l'attività di ricerca e simulazione, ed il Prof. Dozio che ha messo a disposizione il suo tempo per fornirmi preziosi spunti per una attività sperimentale purtroppo non realizzatasi a causa della attuale difficile situazione a livello sanitario. Infine, non posso non menzionare la capacità di organizzazione e risposta del Politecnico di Milano di fronte all'emergenza COVID-19. Nonostante le difficoltà di una situazione senza recenti precedenti, il Personale Universitario è stato in grado di garantire in tempi ristretti didattica ed esami di Laurea in forma telematica, venendo incontro alle necessità della maggioranza e mantenendo costantemente informato ogni singolo studente. Ciò mi rende ancora più fiero di essere stato uno studente di questo Istituto.

Sommario

Il controllo del rumore richiede approcci semplici ed economici che forniscano soluzioni industriali capaci di essere competitive negli innumerevoli campi in cui trovano applicazione, che spaziano dall'attenuazione del rumore di grosse apparecchiature industriali a quello interno in veicoli ed edifici. Il rumore in cabina degli aeromobili, in particolar modo le componenti tonali a bassa frequenza tipiche di turboelica e convertiplani, rappresenta un importante motivo di fastidio in quanto causa di difficoltà di comunicazione, senso di fatica e perdita di concentrazione. In questa attività viene presentata e simulata una semplice soluzione di controllo per la cancellazione locale attiva del rumore dell'elica in cabina. Il risultato finale della Tesi è la proposta di una testata sedile attiva ottimizzata in grado di fornire circa 10 dB di attenuazione nell'intorno della testa del pilota. Questa configurazione può rappresentare un' alternativa economica, robusta e flessibile rispetto a riprogettazioni nel velivolo, a tecniche di controllo acustico passive o all'utilizzo di cuffie a cancellazione del rumore.

Abstract

Acoustic noise control requires simple and low-cost approaches in order to provide efficient industrial solutions capable of keeping up with its countless fields of application, ranging from attenuation of large industrial equipment noise to vehicle and buildings interior one. Aircraft cabin noise, in particular low-frequency tonal contributions typical of turboprops and tiltrotors, represent a severe cause of discomfort causing speech intelligibility reduction, fatigue and loss of concentration. In this activity, a simple control solution for local active propeller-induced cabin noise cancellation is presented and simulated. The final result of this Thesis is the proposal for an optimized active headrest configuration capable of around 10 dB attenuation in the vicinity of the pilot's head. This may represent a cheap, robust and flexible alternative with respect to aircraft redesign, passive noise control techniques or pilot's noise cancelling headset.

Contents

List of Figures

Introduction

Acoustic noise control requires simple and low-cost approaches in order to provide efficient industrial solutions capable of keeping up with its countless fields of application, ranging from attenuation of large industrial equipment noise to vehicle and buildings interior one. Aircraft cabin noise, in particular low-frequency tonal contributions, represent a severe cause of discomfort. Even when the internal sound pressure level is below the one for which hearing problems may arise, it significantly reduces speech intelligibility and induces fatigue and loss of concentration [1],[2]. All of this may lead to an increased risk for accidents.

Unfortunately, low-frequency noise is not efficiently reduced by conventional passive control techniques such as acoustic panels or barriers, since the acoustical damping and reflection capabilities of any material tend to drop when the impacting sound frequency is low. As a rule of thumb, passive noise control techniques become effective at frequencies higher then 500 Hz [3]. Active noise control [4] can then be exploited in retrospect to avoid expensive redesigning or unsustainable increases in weight and therefore fuel consumption. It consists in distributing a set of actuators and sensors with the aim of adaptively cancel out a disturbance. In the acoustical field, the actuators are control loudspeakers while the sensors are error and reference microphones. This approach can be used in the structural field as well to actively reduce low and mid-frequency vibrations [5]. The physical basis for this technique is the superposition effect. In presence of a disturbance at one or more sensors, an adaptive control algorithm has the task of driving the actuators for the purpose of generating counter-phase control actions at the cancelling stations, thus giving zero sum in an ideal case.

Turboprop and tiltrotor internal noise typically consists in high narrowband peaks at well-defined frequencies nestled in lower broadband noise. The most relevant contribution is related to the propellers revolutions per minute which

defines the blade passage frequency (BPF). Multiples of the BPF are important tonal contributions in the cabin noise spectra as well [6]. A narrowband noise system for specifically-targeted frequencies attenuation is then certainly required, but in real life applications some other aspects have to be taken into account. First of all, the presence of mismatches between the real and estimated instantaneous frequency of the noise will almost certainly led to a degradation in performances for a simple narrowband system. Moreover, the noise frequency content does not always remain constant in time but it will change if the operational conditions are varied. To compensate for this effects, real time and high precision frequency estimation is required, which translates into the need for reliable non-acoustic sensors and/or frequency estimation algorithms. A slight improvement of the system robustness can be obtained by driving the control with measures coming from one reference microphone. This will also provide some broadband noise cancelling, but comes with an increase in the system complexity as well. In addition, the achievable reduction is not the only relevant performance indicator, but the attenuation region size also plays an important role. For this reason, a multi-channel control algorithm is used in order for the secondary sources to give a certain spatial extension to the area interested by the control as well as to provide the capability of cancelling the first enclosure acoustic modes [9]. The final solution must be as simple as possible for fast implementation on cheap hardware architectures.

A multichannel control scheme for both narrowband and broadband attenuation is proposed in Chapter 2. This solution has progressively been built and tested by taking into account the previously-described practical concerns. A MATLAB acoustic simulation tool for small environments is then presented in Chapter 3. This code is described in its parts and validated to check for its correct implementation and precision by comparing simple analysis outputs with known classical acoustics theory results. Then it has been coupled with the proposed control system in order to test the performances of the solution under more realistic conditions. In Chapter 4 a simulation is defined and performed with the aim of finding an optimized loudspeakers configuration for the minimization of the acoustical pressure in a limited region in the vicinity of a pilot's head. Both noise reduction and attenuation zone size are discussed. Even though the optimization is constrained to a small region, a full overview on an optimal configuration can be given in a rational way as a preliminary activity for subsequent experimental realizations.

Chapter 1

State of art

Active noise control is a well-established industrial solution in many different fields. As stated by Gordon [10], it briefly consists in the application of the wave superposition principle to acoustic noise attenuation problems, and it can be divided into four main categories: one-dimensional field noise, propeller and fan noise, noise in 3D spaces, and personal hearing protection systems. Specific applications are then aircraft noise, ducts and pipes noise, fan noise and helicopter rotor noise, as well as cars cabin noise and buildings interior one.
In particular, for this activity the interest will be focused on periodic disturbances in a 3D reverberant environment. Propeller noise can be divided into two main categories: directly-generated one and turbulence-induced. The first one is highly tonal noise related to the fundamental propeller frequency and its harmonics, while the second one is generated by blade tip turbulence-induced vibrations on the fuselage panels or other structural components. As a consequence, active noise control may directly act on the sound field (ANC) as well as on the dynamical behavior of the vehicle structure (ASAC). Comprehensive simulations then require an accurate knowledge and modelling of the coupling between acoustics and components dynamics, in order to act effectively on the dominant mode which typically defines the primary acoustical field [11].
Noise control in 3D environments is the most intractable area in ANC systems framework due to practical problems such as stability constraints, non-causality and the requirement for limited-dimensions and potentially numerous actuators. Reflections play an important role as well, creating acoustic feedback paths and thus affecting the system stability [12].

Nevertheless, local noise control can still be achieved. Moreover, performances improvement can be obtained by coupling active noise control with conventional passive control techniques, such as acoustic absorbers capable of reflection damping. As a matter of fact, noise attenuation in aircraft and helicopter applications cannot typically rely on one single solution, but is the result of a plethora of different approaches, each one with its own physical basis, fields of application and limits.
In this chapter, a review on both the required acoustics basics ([36]) and the active noise control theory ([8]) is presented, as well as an overview on the aeronautical noise problem and solutions with respect to the frequencies of interest.

1.1 Acoustics basics

1.1.1 The wave equation and Helmoltz equation

Sound is defined as a small pressure perturbation propagating in an elastic media during time. The governing equations of acoustics are the momentum equation and the continuity equation for an inviscid, irrotational Newtonian fluid, obtained under the hypothesis of isentropicity and small field perturbations:

$$\nabla p' = -\rho_0 \frac{\partial \boldsymbol{u}}{\partial t} \tag{1.1}$$

$$\nabla \cdot \boldsymbol{u} = -\frac{1}{\rho_0 c^2} \frac{\partial p'}{\partial t} \tag{1.2}$$

where p' is the acoustical pressure (a small variation of the pressure with respect to the atmospheric one), $\boldsymbol{u} = (u_x, u_y, u_z)^T$ is the particle velocity vector (under the hypothesis of linearization around a condition for which $u_{x,ref} = 0, u_{y,ref} = 0, u_{z,ref} = 0$), and ρ_0 and c are the transmission medium density and speed of sound respectively.
By combining 1.1 and 1.2 the homogeneous 3D wave equation is obtained:

$$\nabla^2 p' = \frac{1}{c^2} \frac{\partial^2 p'}{\partial t^2} \tag{1.3}$$

In presence of a forcing term expressed as an externally-imposed volume velocity $q(\boldsymbol{r}, t)$:

$$\nabla^2 p' - \frac{1}{c^2} \frac{\partial^2 p'}{\partial t^2} = -\rho_0 \frac{\partial q}{\partial t} \tag{1.4}$$

Wave equation 1.4 is typically conveniently solved (both numerically and analytically) in another form. Switching to complex notation, it is possible to assume the (complex) acoustical pressure $\boldsymbol{p'}$ can be written as the product of a complex space-dependent term and a complex time-dependent term :

$$\boldsymbol{p'}(\boldsymbol{r}, t) = \boldsymbol{P}(\boldsymbol{r})\boldsymbol{T}(t) \tag{1.5}$$

obtaining from eq. 1.3 the homogeneous Helmoltz equation

$$\nabla^2 \boldsymbol{P} = -k^2 \boldsymbol{P} \tag{1.6}$$

as well as an equation describing the pressure behavior in time:

$$\frac{\partial^2 \boldsymbol{T}}{\partial t^2} + \omega^2 \boldsymbol{T} = 0 \tag{1.7}$$

ω is the angular frequency while $k = \frac{\omega}{c}$ is the wavenumber, or spatial frequency of the wave.
The time solution will be a linear combination of sine and cosine functions, whose exact form is determined by the initial conditions, while the form of the solution in space will depend on the boundary conditions. In presence of a forcing term, 1.6 becomes:

$$\nabla^2 \boldsymbol{P} + k^2 \boldsymbol{P} = -\int_{V_0} \boldsymbol{f}(\boldsymbol{r_0}) \delta(\boldsymbol{r} - \boldsymbol{r_0}) dV(\boldsymbol{r_0}) \tag{1.8}$$

where $\boldsymbol{r_0}$ and V_0 express the source position and the volume where the source is located respectively. $\boldsymbol{f(r)}$ comes from the assumption that $f(\boldsymbol{r}, t) = -\rho_0 \frac{\partial q(\boldsymbol{r}, t)}{\partial t}$ can be written as an harmonic source, thus $f(\boldsymbol{r}, t) = \boldsymbol{f(r)} e^{-j\omega t}$.
The boundary conditions for equation 1.8 can be generally expressed as

$$\alpha \boldsymbol{P} + \beta \boldsymbol{U} = \gamma \tag{1.9}$$

For $\beta = 0$ it corresponds to a Dirichlet boundary condition, for $\alpha = 0$ to a Neumann boundary condition while for $\gamma = 0$ it is called Robin condition or impedance condition. The complex ratio between the acoustic pressure and the particle velocity is in fact generally defined as the acoustic impedance $\boldsymbol{Z}$:

$$\boldsymbol{Z} = \frac{\boldsymbol{P}}{\boldsymbol{U}} \tag{1.10}$$

Two other important quantities in acoustics are the acoustic energy and intensity. The acoustic energy can be calculated (in absence of dissipation)

as the sum of potential and kinetic energy of the fluid in which the sound propagates. The former is induced by the compression and expansion of the medium while the latter is due to the motion of the fluid:

$$\epsilon = \frac{1}{2}\frac{p'^{\,2}}{\rho_0 c^2} + \frac{1}{2}\rho_0 u^2 \tag{1.11}$$

Where $u = |\boldsymbol{u}|$ is the particle velocity. Acoustic intensity describes how acoustic energy changes in time. From a 3D energy balance:

$$\frac{\partial \epsilon}{\partial t} + \nabla \cdot \boldsymbol{I} = 0 \tag{1.12}$$

Where $\boldsymbol{I} = p'\boldsymbol{u}$ is the acoustic intensity vector. The second term on the left-hand side of equation 1.12 expresses the net outflow acoustical power through the fluid surfaces. In other words, the acoustical intensity is the acoustic energy per unit area in time and space.

1.1.2 Analytical solutions of the wave equation

Different analytical solutions exist for the 3D wave equation 1.3. Two relevant examples in the acoustics theory are the plane wave and the acoustic monopole, which will be referenced in Chapter 3.
A one-dimensional, planar acoustic wave with a certain direction in space at time t is expressed as:

$$\boldsymbol{p}(\boldsymbol{r}, t) = \boldsymbol{A} e^{-j(\omega t - \boldsymbol{k}\cdot\boldsymbol{r})} \tag{1.13}$$

where $\boldsymbol{A}$ is a complex amplitude and $\boldsymbol{k}$ the wavenumber vector. Equation 1.13 satisfies equation 1.3. Plane waves are characterized by constant physical properties (i.e. pressure and velocity) in the plane perpendicular to $\boldsymbol{k}$ at $\boldsymbol{r}$. In other words, their wavefronts (the geometric loci of points vibrating at the same phase) are planes perpendicular to $\boldsymbol{k}$. Moreover, the wave impedence for a planar wave is

$$\boldsymbol{Z} = \frac{\boldsymbol{p}}{\boldsymbol{u_r}} = \rho_0 c \tag{1.14}$$

Eq. 1.14 states that for this kind of solutions the wave impedance is precisely the same as the characteristic impedance of the medium. Thus, in an unbounded fluid, plane waves propagate in the wave number vector direction, independent of the position, frequency, wave number, and wavelength.

Another solution can be obtained writing the acoustic wave equation 1.3 in spherical coordinates, assuming that the pressure is independent of the polar and azimuth angles and only depends on the distance from the origin r:

$$\frac{\partial^2(rp')}{\partial r^2} = \frac{1}{c^2}\frac{\partial^2(rp')}{\partial t^2} \tag{1.15}$$

A solution for equation 1.15 is in fact represented by the acoustic monopole:

$$\boldsymbol{p}(\boldsymbol{r}, t) = \frac{\boldsymbol{A}}{r} e^{-j(\omega t - \boldsymbol{k}\cdot\boldsymbol{r})} \tag{1.16}$$

which tends to infinity for $r \to \infty$, and is inversely proportional to the radius r. Its impedance is

$$\boldsymbol{Z} = \rho_0 c \left[\frac{(kr)^2}{1+(kr)^2} - j\frac{kr}{1+(kr)^2} \right] \tag{1.17}$$

From 1.17, if the distance from the origin is large compared to the wavelength of interest ($kr >> 1$) then the monopole behaves as a plane wave. This is typically referred as "far-field" region. On the other hand, if the position is very close to the origin with respect to the wavelength ($kr << 1$), then the pressure and velocity have a $-90°$ phase difference, meaning that the fluid particle is accelerated by the acoustic pressure. This region is instead referred as "near-field" region. The monopole near-field region is also known as $6dB$ drop region, since the following relationship holds if $r_2 = 2r_1$:

$$10log_{10}\frac{I_{r_2}}{I_{r_1}} = -6\ dB \tag{1.18}$$

Where I_{r_i} is the acoustic energy at radial distance r_i.
This simple acoustic field satisfies the linear wave equation. That implies that the arbitrary superposition of this type of solutions satisfies the governing wave equation as well. We can therefore attempt to construct any type of wave by using the monopole. On the basis of this consideration, other analytical expressions satisfying the 3D acoustics wave equation can be obtained, such as the dipole and the quadrupole [13]. The first one consists in two close monopoles with a phase difference of 180° and is characterized by a directivity pattern in the sound radiation with a maxima along the 0° and 180° directions, and no sound radiation along the 90° and 270° directions. It may be used to represent a loudspeaker pressure field, but at low frequencies the directivity pattern of a typical dynamic loudspeaker looks more like that of a monopole [34]. As a final note, it is less efficient than a monopole with the same source strength at radiating low frequency sounds.

1.1.3 Modal analysis

One very well-known method to find solutions which satisfy eq. 1.8 and 1.9 is the modal analysis. It is based on obtaining $\boldsymbol{P(r)}$ in eq. 1.8 as the linear combination of the solutions $\boldsymbol{\Psi_{l,m,n}}$ of equation 1.6, which are called eigenfunctions. In other words, thanks to superposition:

$$\boldsymbol{P(r)} = \sum_{l,m,n=0}^{\infty} \boldsymbol{a_{l,m,n}\Psi_{l,m,n}(r)} \tag{1.19}$$

The advantage of this method is that a linear combination of the eigenmodes also satisfies the given boundary condition. Assuming a single harmonic source with radial frequency ω and size S exciting an acoustic environment with volume V at the location $\boldsymbol{r_0}$, the modal coefficients $\boldsymbol{a_{l,m,n}}$ expression can be found to be:

$$\boldsymbol{a_{l,m,n}} = \frac{-4\pi S}{V} \frac{\boldsymbol{\Psi^*_{l,m,n}(r_0)}}{\Lambda_{l,m,n}(k^2 - k^2_{l,m,n})} \tag{1.20}$$

The "*" indicates complex conjugate operator. $k_{l,m,n}$ is the eigenvalue associated to eigenfunction $\boldsymbol{\Psi_{l,m,n}}$ while $\Lambda_{l,m,n}$ is the mode normalization factor defined by

$$\frac{1}{V}\int_V \boldsymbol{\Psi_{l,m,n}\Psi^*_{l,m,n}} dV = \Lambda_{l,m,n}\delta_{l,l'}\delta_{m,m'}\delta_{n,n'} \tag{1.21}$$

Where δ indicates the Kronecker's delta function.
Modal analysis is a possible mathematical approach for the solution of closed spaces acoustics in frequency domain: it aims in finding sound waves distribution with regard to their possible spatial distribution for each frequency. It finds application mainly for simple boundary geometries (such as rectangular rooms with rigid walls) to provide analytical solutions for model validation [39]. Another frequency-based method which is instead heavily exploited numerically is based on the Kirchhoff–Helmholtz integral equation described in subsection 1.1.4.

1.1.4 The Kirchhoff–Helmholtz integral equation

Helmoltz equation 1.8, under the assumption of a single point-like unit source at $\boldsymbol{r} = \boldsymbol{r_0}$ becomes:

$$\nabla^2 \boldsymbol{G} + k^2 \boldsymbol{G} = -\delta(\boldsymbol{r} - \boldsymbol{r_0}) \tag{1.22}$$

Where the pressure $\boldsymbol{P}$ has been substituted by the Green's function $\boldsymbol{G}$, which is generally defined as a solution of equation 1.22. By manipulating 1.22 and 1.8 it is possible to obtain:

$$\boldsymbol{P}(\boldsymbol{r}) = \int_{V_0} \boldsymbol{G}\boldsymbol{f}(\boldsymbol{r_0}) dV + \int_{S_0} (\boldsymbol{P}\nabla_0 \boldsymbol{G} - \boldsymbol{G}\nabla_0 \boldsymbol{P}) \cdot \boldsymbol{n_0} dS \tag{1.23}$$

Where S_0 is the domain boundary surface with normal in-going unit vector $\boldsymbol{n_0}$ surrounding the integral volume V_0, and ∇_0 is the gradient operator defined over the boundary surface. The sound pressure at $\boldsymbol{r}$ consists of two components: one is a direct effect from the sound source and the other is due to the reflections from the boundaries. Without internal sound sources (volume-free source, $\boldsymbol{f}(\boldsymbol{r_0}) = 0$), eq. 1.23 becomes:

$$\boldsymbol{P}(\boldsymbol{r}) = \int_{S_0} (\boldsymbol{P}\nabla_0 \boldsymbol{G} - \boldsymbol{G}\nabla_0 \boldsymbol{P}) \cdot \boldsymbol{n_0} dS \tag{1.24}$$

From the linearized Euler equation 1.1 the pressure-velocity relation under single-tone hypothesis holds :

$$\nabla \boldsymbol{P} = -jk\rho_0 c \boldsymbol{U} \tag{1.25}$$

According to Kirchhoff–Helmholtz integral equation 1.24 and relation 1.25, sound can be generated by two boundary mechanisms: the fluctuation of fluid particles which are attached to the surface of a vibrating structure (the second right-hand term) or as pressure changes coming from imposed pressure fluctuation (first right-hand term). The former is generally called "velocity source or velocity sound source", or radiation mechanism, while the latter is called "pressure source or pressure sound source". The Green's function acts as a propagator for boundary pressure and particle velocity to internal ones, and can be selected suitably to comply with Dirichlet or Neumann boundary conditions to find analytical solutions for radiation problems of practical interest, such as the cylindrical piston radiation in an infinite baffle or the radiation from a finite vibrating plate. A typical choice for $\boldsymbol{G}$ is the 3D free-field Green's function:

$$\boldsymbol{G}(r) = -\frac{e^{-jkr}}{4\pi r} \tag{1.26}$$

On the basis of superposition it is possible to describe any sound field using only singular functions that satisfy the governing equation. The simplest known source field is associated to the acoustic monopole at an arbitrary location, so it is possible to assume any sound field can be constructed by appropriately distributing acoustic monopole sources by superposition. Actually, eq. 1.24 can be conveniently seen as the superposition over the surface S_0 of acoustic monopoles and dipoles pressure fields [14]. Numerical approaches like acoustic holography or boundary elements methods (BEM) describe the internal sound field by using Green's function, transforming the information of sound pressure and velocity on the boundary to the ones in the point of interest in the field. They involve the distribution of a function that satisfies the governing equation (i.e. the wave equation) on the boundary. It can be a singular function or a Green's function. The solution then consists in the contribution of each function which satisfies the boundary conditions. BEM method in particular is heavily used in acoustics: it involves the boundary surface division into small elements and then the numerical evaluation of integral 1.24 by means of an interpolation of both the integration surface geometry and the acoustic variables $(\boldsymbol{P}, \boldsymbol{U})$ using the same set of locally-defined shape functions, leading to a linear system. Radiation acoustics problems in which thin structures vibration velocity induces a pressure field inside a closed environment are typically solved in this framework.

1.1.5 Absolute and subjective noise measures

Absolute units in acoustics (Pa, $\frac{m}{s}$) are alongside subjective measures which take into account the large interval of acoustical pressures audible by humans and the frequency response of their auditory system.
Humans do not hear the frequency of sound in absolute scale, but rather relatively, so relative units for both frequencies and amplitudes are normally used. The octave band is a typical relative scale. The band between a certain frequency (f_1) and the frequency that is its double ($f_2 = 2f_1$) is referred to as an "octave". The center frequency (f_0) of each band corresponds to the geometrical center of the band. According to this definition, the center frequency can be any value. However, for convenience, standard center frequencies are used ($31.5Hz$, $63Hz$, $125Hz$, $250Hz$ and so on). Humans can hear sound at a broad range of frequencies as well as at a wide range of amplitudes. The audible frequency range is between $20Hz$ and $20kHz$.

For what concerning the pressure amplitudes, a relative decibel (dB) scale is used to narrow the excursion of the acoustical pressure values:

$$SPL = 10log_{10}\left(\frac{p_{avg}^2}{p_0^2}\right) \tag{1.27}$$

Where $p_0 = 2 \cdot 10^{-5} Pa$ is the human audibility threshold. p_{avg}^2 is the squared acoustical pressure averaged over a period of time equal to T:

$$p_{avg}^2 = \frac{1}{T}\int_0^T p^2(t)dt \tag{1.28}$$

SPL (sound pressure level) can be evaluated directly applying eq. 1.27 or an approximate formula in frequency domain for the squared average pressure:

$$p_{avg}^2 \approx \sum_m \frac{1}{2}|\boldsymbol{P_m}|^2 \tag{1.29}$$

Being $\boldsymbol{P_m}$ the acoustical pressure Fourier transform evaluated at frequency f_m. As a rule of thumb, the minimum SPL variation that can be perceived is around $2-3$ dB. Some pressure sources with the associated SPL are listed in fig. 1.1.
Moreover, human perception of sound is highly influenced by their auditory system frequency response. This results into the fact that to perceive the same level of loudness (measured in *phon*) a different SPL is actually required in function of the frequency. This is expressed by equal loudness curves reported in fig. 1.2. Analogously, SPL measures can be thought as filtered by a suitable frequency function. Typical weighting functions for defining subjective noise pressure levels (namely A-weighting, C-weighting and K-weighting) are given in figure 1.3. In particular, the former defines A-weighted decibels, or $dB(A)$, which are of common use in the literature.

Sound level (dB)	*Source of sound*
180	Rocket engine
170	
160	
150	Jet plane take off
140	Threshold of pain
130	Maximum recorded rock music
120	Thunder cap
110	Autohorn 1 m away
100	Jet fly over at 300 m, construction work, newspaper
90	Motor cycle/8 m away, food blender
80	
70	Vacuum cleaner, ordinary conversation
60	Air conditioning unit, 6 m away; light traffic noise
50	Average living room
40	
30	Library, soft whisper
20	Broadcasting studio
10	Rustling leaf
0	Threshold of hearing

Figure 1.1: SPL associated to various sound sources

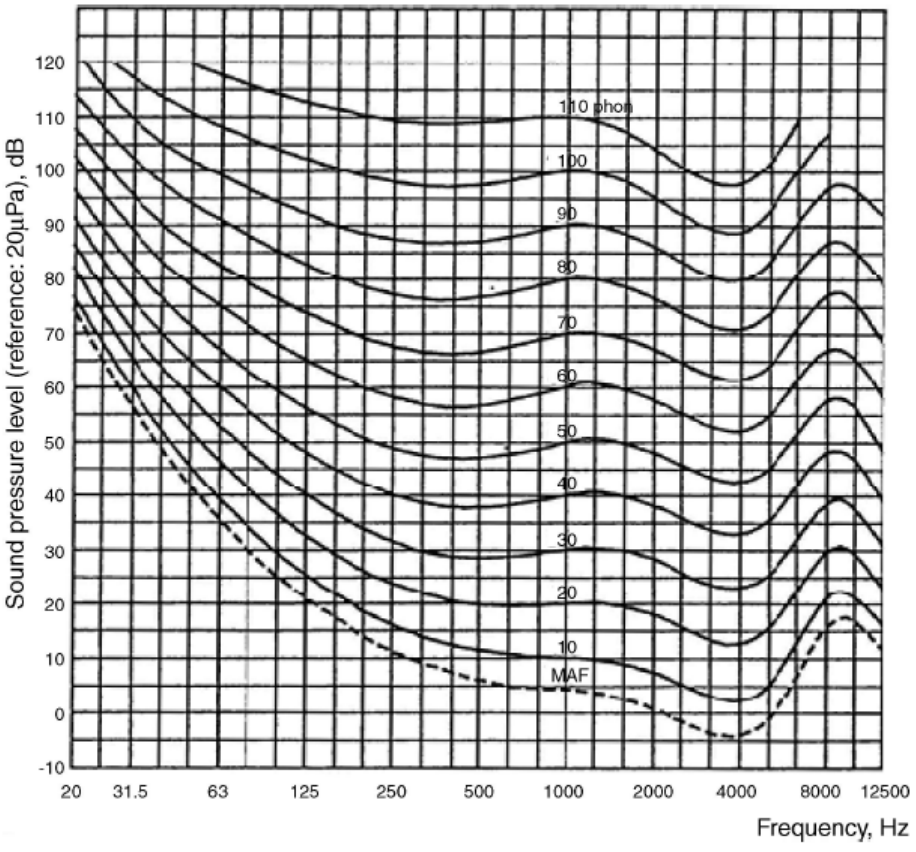

Figure 1.2: Equal loudness curves

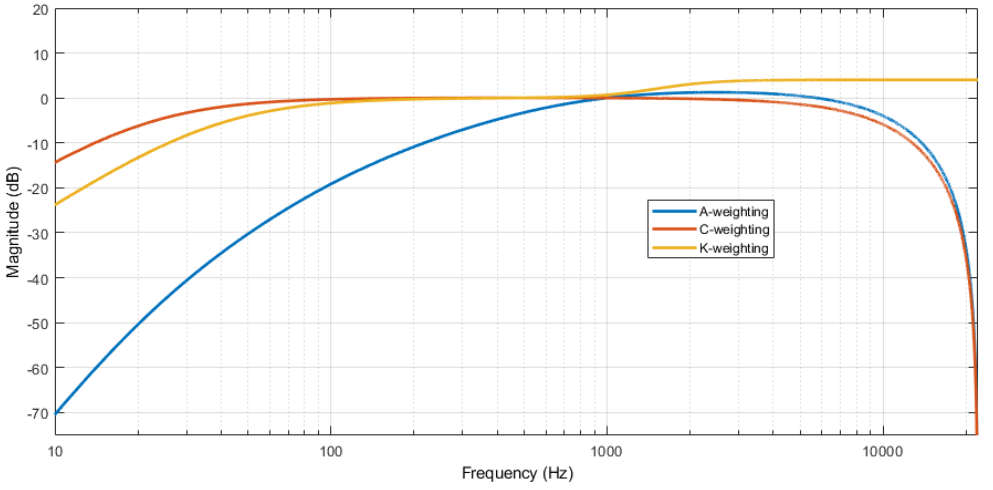

Figure 1.3: Human auditory system weighting functions

1.2 Acoustical noise and vibrations problem in aeronautics

Cabin noise in aircraft and helicopters is due to the presence of direct acoustical paths from the propulsive system (i.e. unavoidable leaks) and fuselage panels radiation. The latter is associated to high frequency vibration in engines or hydraulic components, or the complex interaction between the structure dynamics (links or the panels themselves) and external air excitation. All these phenomena are simultaneous, meaning a wide noise frequency range will be interested. As a consequence, noise reduction involves many different practical solutions on the base of the frequency of interest, each of these with its performances, cost and weight.
In this section, some remarks on the acoustics of closed spaces and noise control techniques for aeronautical applications are presented. In addition, some theoretical results will be used for the definition and validation of an acoustic model presented in Chapter 3.

1.2.1 Acoustics of closed spaces

To describe the acoustics of a closed space, its volume V has to be considered with regard to the sound wavelength λ of interest. If this ratio is sufficiently large, the waves would behave as if in a large space, reaching all possible places. On the contrary, if the volume is small compared to the wavelength, then the wave would appear to be everywhere in the space instantly, since no propagation can physically occur. This defines acoustically large and small spaces. For an acoustically large space relation 1.30 holds:

$$\sqrt[3]{V} >> \lambda \tag{1.30}$$

Acoustic waves tend to have very complicated patterns in large enclosures as time advances. Initially it is possible to observe a direct sound field as waves propagate from the source to the boundaries. Then reflections occur, creating a reverberant field which is typically not hugely dependent upon the location in the space. A diffuse field implies a space in which the sound is likely to be equally distributed irrespective of the position, or alternatively a space that has uniformly averaged acoustic energy independent of the position. Diffuse fields are then reverberant fields that can be typically associated to irregular boundary shapes and impedance distributions in which random reflections occur, averaging the overall pressure in space. The source near field is instead characterized at any time by pronounced space variations (for instance, the $-6dB$ region near to a monopole source).
For spaces satisfying 1.30 (large rooms), under the hypothesis of diffuse sound field and small boundary absorption coefficients, Sabine theory holds, and a single parameter can be used to describe completely the room acoustics. The reverberation time T_{rev} is defined as the time in which the acoustic energy drops by a factor 10^6 after an impulsive source has been introduced in a baricentric position of the room. Sabine found its expression to be:

$$T_{rev} = 0.1611 \frac{V}{\sum_{n=1}^{N} \alpha_n A_n} \tag{1.31}$$

Where N is the total number of room boundary walls, with area A_n and absorption coefficient (the ratio of the absorbed sound power to the incident sound power) α_n.

In acoustically small spaces, on the contrary, the acoustic pressure and velocity can be considered relatively constant, so the entire medium is not dominated by the propagation properties of sound waves but moves with a single phase, and it can be thus regarded as a single-degree vibratory system. A common example in noise control engineering is represented by Helmoltz resonators. They consists in small acoustic resonant spaces composed by a neck of area A and length l, and a cavity of volume V (fig. 1.4). The air in the neck is excited by an external pressure P_{out} and the cavity internal pressure P, and it vibrates with a certain velocity (like a mass-spring system) compressing or expanding the internal air.

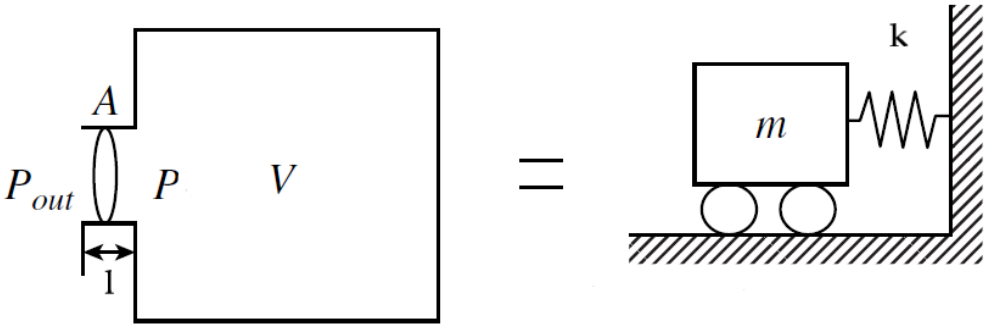

Figure 1.4: Helmoltz resonator simplified model and dynamical equivalence

The constitutive equation is in fact a 2nd order differental equation:

$$\frac{Vl}{Ac^2}\frac{\partial^2 p}{\partial t^2} + p = p_{out} \tag{1.32}$$

And the resonance frequency of the cavity is then

$$\omega_n = c\sqrt{\frac{A}{lV}} \tag{1.33}$$

Eq. 1.32 and 1.33 show that an Helmoltz resonator will be strongly excited at a certain frequency, generating a massive impedance mismatch at ω_n but without the need for a physical wall. A resonator then serves as a notched band stop filter with ω_n as its bandwidth center frequency, making it a possible choice for passive narrowband noise attenuation. Figure 1.5 shows typical configurations for acoustic resonant cavities for noise attenuation.

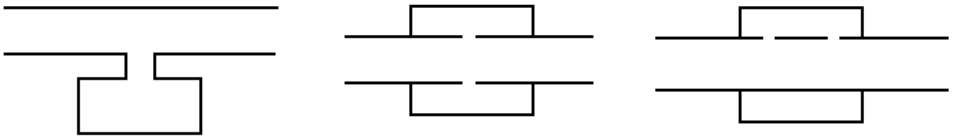

Figure 1.5: Typical Helmoltz resonators configurations for noise attenuation

Helmoltz resonators can be put in series organizing them in panels to efficiently reduce the acoustic energy. It must be remembered that their introduction comes at the price of an undesired increase in weight. They find their application for internal cabin noise reduction for frequencies from $500Hz$ to $2kHz$.

1.2.2 Active and passive noise control techniques

Passive noise control techniques are common solutions for aeronautical applications. They typically consist in exploiting acoustic reflection, absorption or damping properties of some materials.
Acoustic reflection is the base of soundproofing. An important theoretical result for practical considerations on acoustic barriers is the mass law. Considering a planar wave normally impacting over a thin wall harmonically vibrating in the direction perpendicular to its plane (x), as depicted in fig. 1.6, equation 1.34 can be obtained. It express the transmission loss R_{TL} of a locally-reacting wall with only mass , with density ρ and thickness t, defined as a logarithmic measure of the acoustic power that is not transmitted through the surface. So it can express for instance the power that can be reflected by a thin, finite thickness fuselage panel or an acoustic barrier.

$$R_{TL} = 10log_{10}\left[1 + \left(\frac{\rho t\omega}{2\rho_0 c}\right)^2\right] \tag{1.34}$$

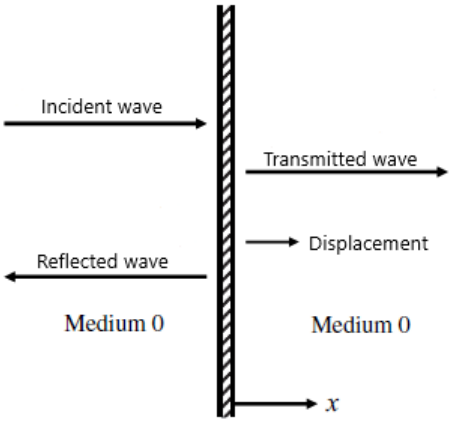

Figure 1.6: Impacting, reflected and transmitted acoustical waves

Equation 1.34 provides an explanation on why low frequency noise coming from external sources is not efficiently reflected back by acoustical barriers. Keeping constant wall density and impacting sound frequency, it is required to increase the thickness (thus the weight) to enhance the transmission loss. This is the reason why active noise control may be preferred at low frequencies with respect to passive one. As a matter of fact, R_{TL} increases by $6dB$ by doubling the frequency (one octave increase in frequency) or the mass per unit length. The transmission loss factor can also be obtained under more general hypothesis, such as planar waves impacting with oblique incidence, partitions with lumped stiffness or non-locally reacting boundaries (for example thin metallic panels in which structural waves propagate in the boundary as the result of internal and external applied pressure) and layers. With respect to the simple case of equation 1.34, stiffness effects in thin panels are relevant at very low and very high frequencies: for a lightly damped wall, in the former case the presence of resonances corresponds to a local decrease in the loss transmission factor, while in the latter case the coincidence effect may occur. Coincidence happens reaching a certain frequency (the so-called critical frequency), when the wavelength of the structural bending wave becomes equal to the wavelength of the impacting sound. When this occurs, it gives rise to a far more efficient transfer of sound energy from one side of the panel to the other leading to a drop in R_{TL} as well. Both resonance and coincidence then degrade the soundproofing properties of an acoustical barrier and must be avoided a priori, during design phase. These considerations are schematized in fig. 1.7.

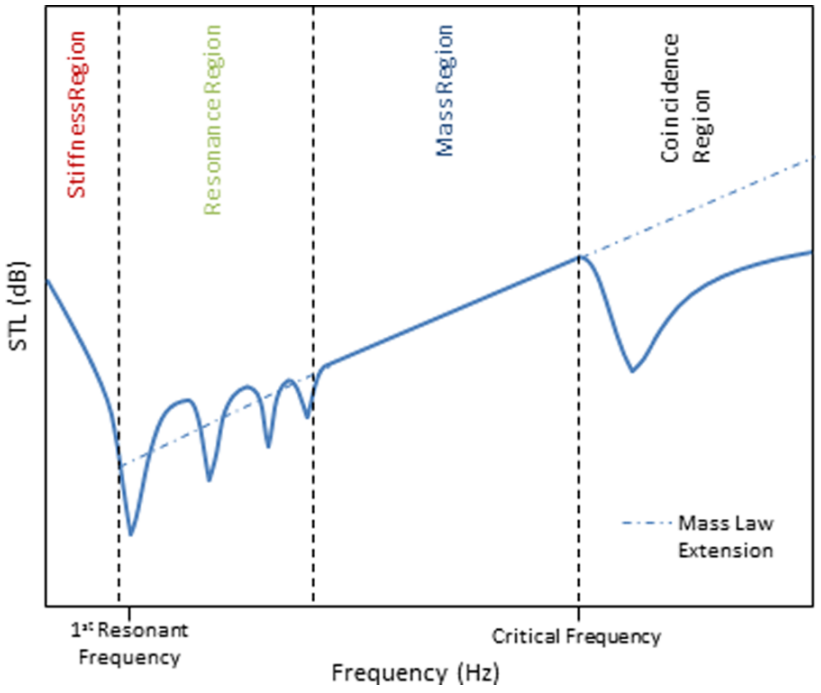

Figure 1.7: R_{TL} behavior with impacting sound frequency

An effective passive solution is double-wall soundproofing, in which air or a porous material is interposed between two thin walls creating a mass-spring-mass system with an higher transmission loss coefficient.
Sound absorption and damping dissipate acoustical energy and vibration energy respectively by converting them into thermal energy. Materials relying on the former effect are typically thick, porous, low density and low stiffness materials (like acoustic foams and fabrics) while the latter is instead typical of viscoelastic materials. They both perform very well as frequencies increases, approximately over $400Hz$. However, at lower frequencies, both the absorption coefficient and loss factor tend to drop [15] [16], reducing their effectiveness as noise control solutions for some applications.
Vibration absorbers (or dynamic absorbers) represent a valid solution for tonal noise reduction with relatively low cost. They basically consist in the coupling of an adequate mass with the vibrating body (primary structure). This results in the creation of some anti-resonance design frequencies.

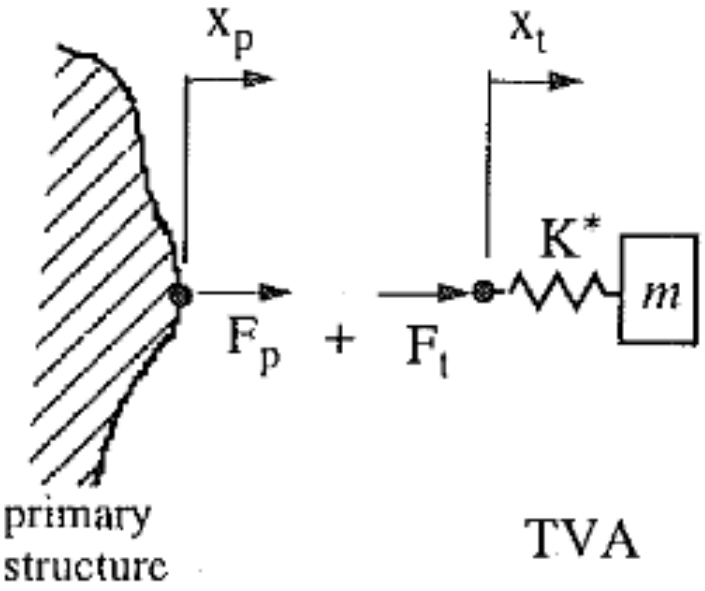

Figure 1.8: Tuned vibration absorber, from [17]

Their application specifically in aeronautical fields has been described for example in [18]. They can work at low frequency as well, but their introduction comes with the price of an increase in weight. For low frequency tonal noise attenuation in presence of viscoelastic damping, the mass of the suspended body m results to be directly proportional to both the vibration attenuation α and the loss factor δ (Sun et al. [17]).

$$m = \alpha\delta\frac{K_S}{\omega_0^2} \tag{1.35}$$

Where ω_0 is the excitation frequency and K_S the spring stiffness. Since some damping must be present to avoid the absorber displacement to reach infinity, high vibration attenuation can be obtained only increasing the mass. Therefore, they typically find their application in avionics. These design philosophies can be applied to internal (trim) panels, which may be realized with suitable soundproofing/absorbing materials or may be suspended to accomplish vibration isolation. Active noise control techniques are also heavily exploited in the automotive and aeronautical fields. They mainly consist in direct anti-phase counter noise generation by means of control loudspeaker in the cabin (active noise cancellation, or ANC) or in the introduction of a cancelling vibration by means of shakers, inertial actuators or piezoceramic patches (structural-acoustic control, or ASAC).

The latter can be exploited for direct control of the fuselage or trim panels vibration, as well as to reduce the radiation of intermediate components (links), and it performs well at mid frequencies, from $500Hz$ to $5kHz$. ANC is instead an effective solution when the frequencies are low, typically under $500Hz$. An example is propeller-induced noise, whose frequency content is narrow and localized at low and specific harmonics. It comes with a small weight increase, but it may result in complex and demanding control configurations as well as poor attenuation performances with respect to passive techniques. This approach will be the interest of the rest of the activity.
Figure 1.9 shows a summary of the possible cabin noise control solutions for helicopter application with their frequency range of interest:

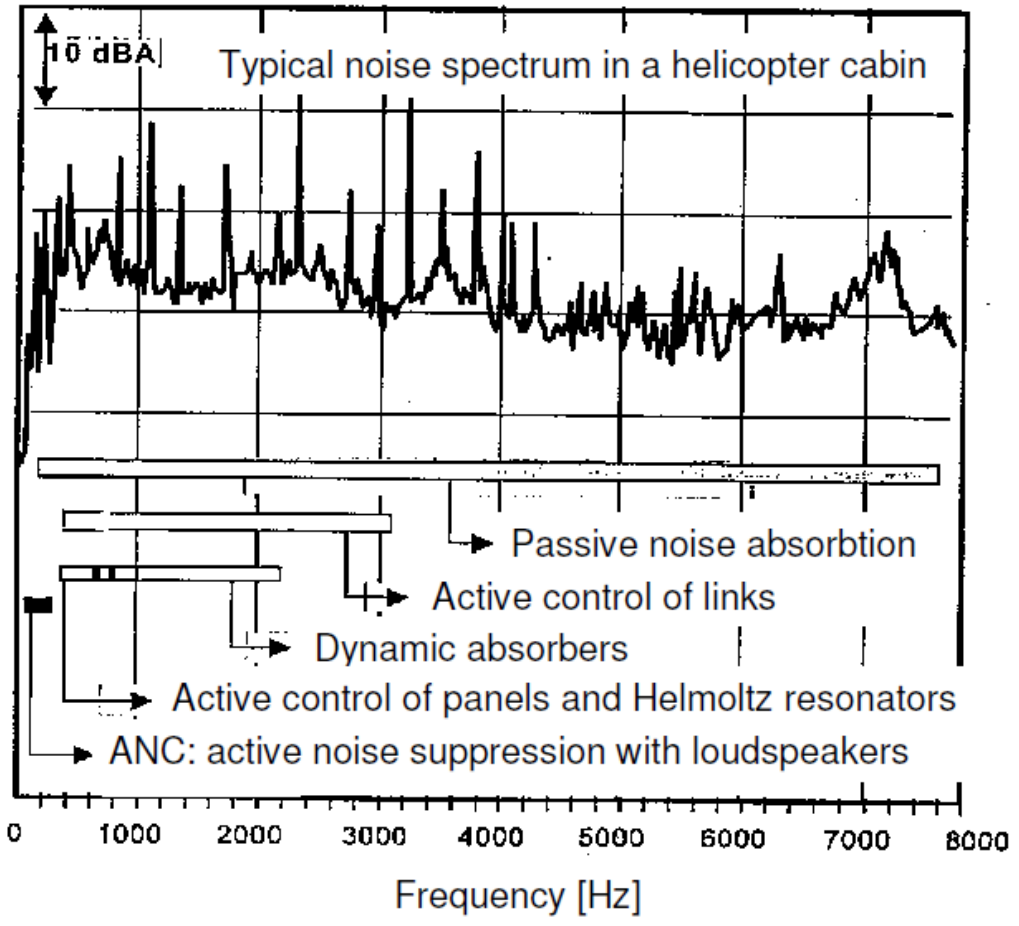

Figure 1.9: Noise control techniques for helicopter cabin noise reduction, from [7]

1.3 Broadband and narrowband feedforward ANC systems

Active noise cancelling systems for low-frequency applications are better explained with a simple single-channel control configuration for narrow duct noise reduction. In figure 1.10 the physical system and main variables are shown at the discrete time instant n under the hypothesis of broadband noise attenuation, while an equivalent block diagram representation is given in fig. 1.11. A main source is generating the primary noise $x(n)$, which induces a disturbance acoustical pressure $d(n)$ at the station of interest. At this position, it is desired to minimize the acoustical pressure, so a control action $y(n)$ is adaptively generated by a control loudspeaker (secondary source) on the basis of an algorithm driven by measures obtained at the previous time instant $n-1$. Since the previously discussed wave superposition principle holds, a residual noise $e(n) = d(n) - y(n)$ can be measured at the station in which is desired to minimize the error. The residual noise, or error acoustical pressure, is measured by an error microphone. The primary noise is instead measured by a reference microphone.

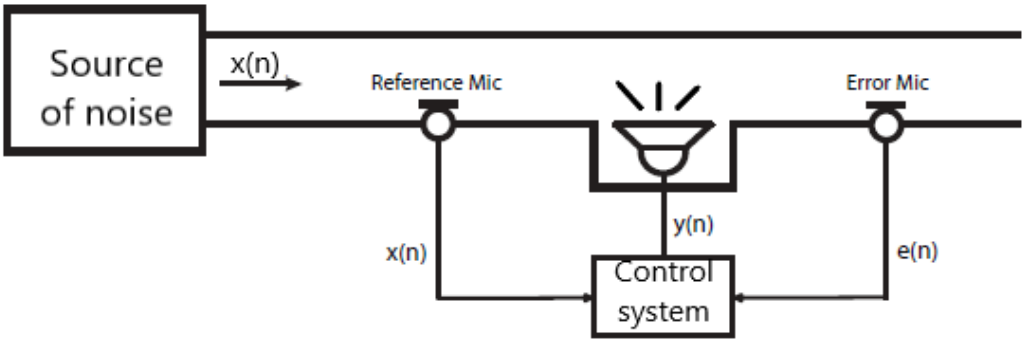

Figure 1.10: Broadband ANC system

$P(z)$ is the (discrete) unknown transfer function between $x(n)$ and $d(n)$. The aim of the controller is to provide a suitable $y(n)$ in order to minimize $e(n)$. The core of the algorithm is the transfer function $W(z)$, which is a finite impulse response filter (FIR filter) whose coefficients are adapted to generate a control signal $y(n)$ giving $x(n)$ and $e(n)$ as inputs. $S(z)$ is called secondary acoustical path, and it indicates the discrete transfer function between the control loudspeaker and the error sensor.

It may contain different contributions: the digital-to-analog (D/A) converter, the reconstruction filter, the power amplifier, the loudspeaker, the acoustic path from the loudspeaker to the error microphone, the error microphone itself, the preamplifier, the anti-aliasing filter, and the analog-to-digital (A/D) converter. As discussed in section 1.4, its estimation is required in order to build a more robust control algorithm.

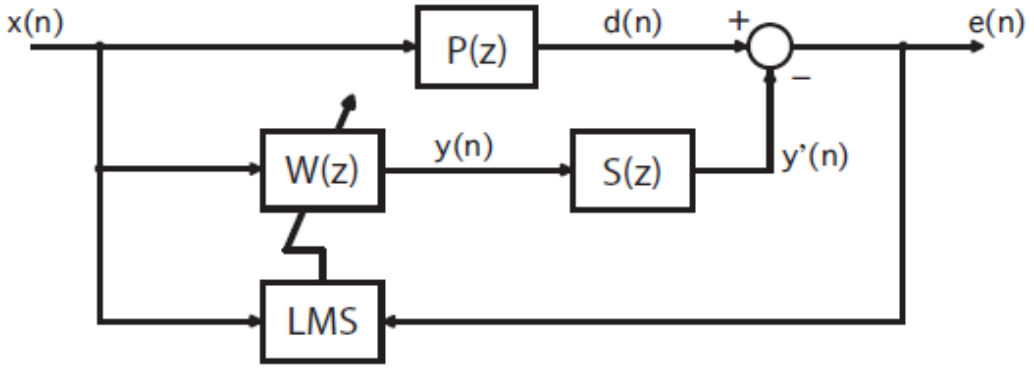

Figure 1.11: Broadband ANC system - Block diagram of LMS system

Inside the controller, an adaptation law of the coefficients of $W(z)$ is implemented. The most commonly used algorithm the LMS (least mean squares) one, which is essentially a gradient-based minimization of the residual error. $W(z)$ coefficients are in fact changed at each n in the steepest descent direction, which is analytically given by the negative gradient direction:

$$\boldsymbol{w}(n+1) = \boldsymbol{w}(n) - \frac{\mu}{2}\boldsymbol{\nabla}\xi(n) \tag{1.36}$$

$\boldsymbol{w}$ is a vector containing the coefficients of FIR filter $W(z)$, $\xi = E[e^2(n)]$ is the expected value of the squared error and μ is called step size, convergence factor or learning rate and expresses the magnitude of the adaptation in the direction of the negative gradient. Assuming that no secondary path is present and $E[e^2(n)] = e(n)$, (Widrow approximation), with some additional computation [8] the following updating equation can be obtained for LMS-based algorithms:

$$\boldsymbol{w}(n+1) = \boldsymbol{w}(n) + \mu e(n)\boldsymbol{x}(n) \tag{1.37}$$

$\boldsymbol{x}(n)$ is a vector containing the L most recent measures of the reference microphone, namely $\boldsymbol{x} = [x(n)\ x(n-1)\ ...\ x(n-L)]^T$. L is the length of filter $\boldsymbol{w}(n)$.

Broadband systems then completely rely on a reference microphone measure to provide a signal which must be sufficiently correlated to the disturbance to achieve effective attenuation, as discussed in section 1.6. Another strategy commonly used for highly periodic noise such as engine noise or propeller noise is to use non-acoustical sensors (i.e. tachometers) which provide an estimate of the frequency content of the noise source. A narrowband attenuation control system scheme is shown in fig. 1.12.

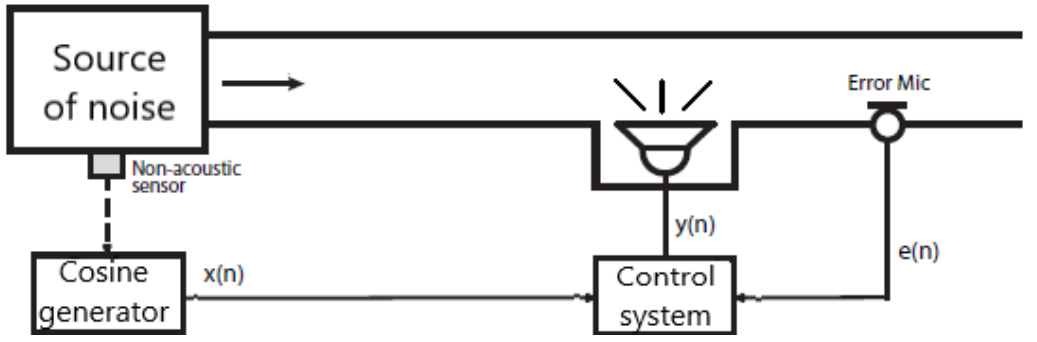

Figure 1.12: Narrowband ANC system

These kind of approaches guarantee some advantages over broadband ones:

- They can be freely tuned and each periodic component of the signal can be independently controlled in order to achieve greater attenuation for specific tones;
- They do not suffer from acoustical feedback (see subsect. 1.4.1);
- $S(z)$ might be modelled only in the vicinity of the tone(s) of interest, enhancing the computational efficiency;
- Non-acoustical sensors do not suffer from nonlinearities and aging;

Two approaches for narrowband noise attenuation are the waveform synthesis and the adaptive notch filtering (ANF). The former requires as reference signal a train of impulses whose period is equal to the inverse of the fundamental frequency of the harmonic to be cancelled. The latter was first proposed by Widrow [19] and uses instead two synthesised sinusoidal signals with a frequency content as close as possible to the harmonic tones to be cancelled.

For this activity only ANF will be considered, since waveform synthesis-based filters have smaller bandwidth [20] and are more difficult to realize in practice.
Figure 1.13 shows the block scheme of an adaptive notch filter. a and b are the constants that are adaptively tuned by the algorithm. $x_A(n)$ is a cosine signal with an harmonic content estimated by a non-acoustic sensor or a frequency estimation algorithm. The 90° block means that another reference signal in quadrature is fed into the controller.

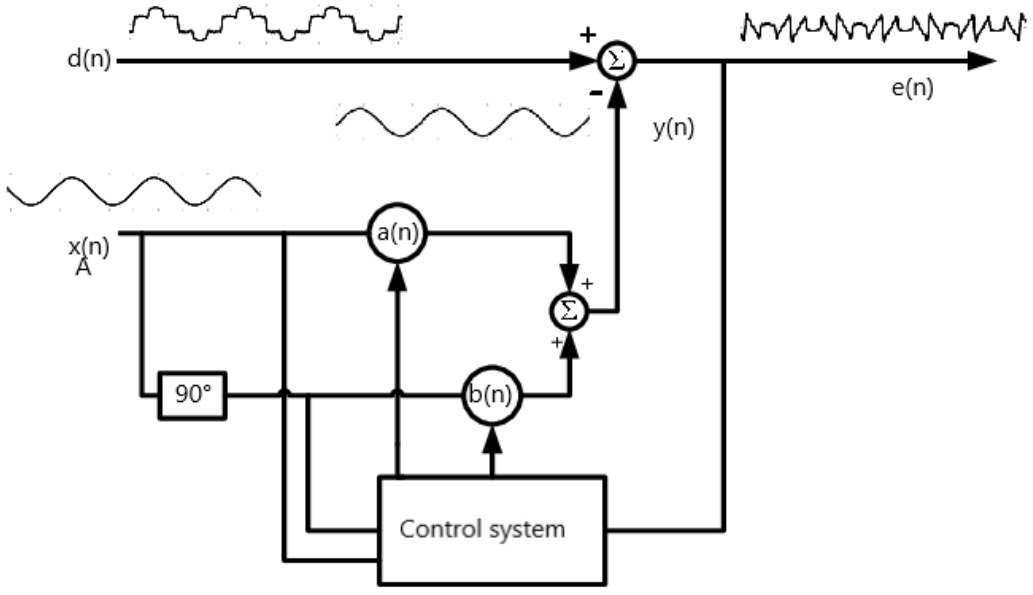

Figure 1.13: Narrowband ANC system - Block diagram of LMS system

The working principle is exactly the same of a broadband system, and the updating equations are:

$$\begin{aligned} a(n+1) &= a(n) + \mu e(n) x_A(n) \\ b(n+1) &= b(n) + \mu e(n) x_B(n) \end{aligned} \tag{1.38}$$

$x_B(n)$ indicates the signal in quadrature with respect to $x_A(n)$, at time n. The narrowband algorithm used for this activity is slightly different from the Widrow one shown in figure 1.13: following the work described by Glover [21], for multicomponent periodic noise a sum of sinusoids can be considered as a reference signal to an adaptive filter with length L much higher than two.

This technique aims in automatically creating a notch for each sinusoid, tracking changes in frequency if a correct spectrum content estimate is output of the tachometer.
A typical adaptive notch filter frequency response is shown in fig. 1.14:

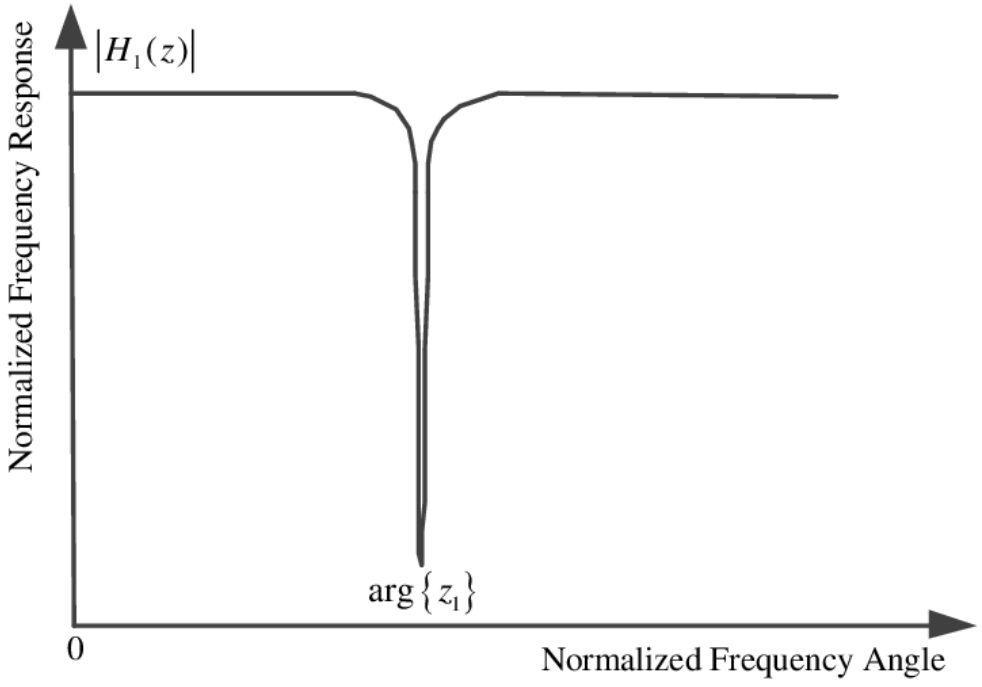

Figure 1.14: Typical adaptive notch filter frequency response

The most important parameters describing an ANF-based system are the input frequency and the filter $3 - dB$ bandwidth B. This can be evaluated for a Glover adaptive notch filter, under the assumption of $x_A(t) = Acos(\omega t)$, as:

$$B = \frac{\mu L A^2}{4\pi T} \tag{1.39}$$

Where T is the control sampling period. The bandwidth is then proportional to the sampling frequency, the learning rate and the control filter length, and it grows quadratically with the reference signal amplitude A. Frequency mismatches between the estimated and the real one may fall outside the range expressed in eq. 1.39 leading to a severe degradation of the attenuation.

1.4 Secondary path effects - The FxLMS algorithm

The secondary path $S(z)$ plays an important role in the system stability, and it cannot be neglected as in section 1.3. The residual error transform can be written as :

$$E(z) = [P(z) - S(z)W(z)]X(z) \tag{1.40}$$

Where $X(z)$ is the frequency transform of the reference signal $x(n)$. It follows that the optimal filter expression is :

$$W_0(z) = \frac{P(z)}{S(z)} \tag{1.41}$$

From equation 1.41 some important conclusions for practical applications can be obtained. First of all, typically high-order adaptive FIR filter are required for a satisfying approximation of the rational function $\frac{1}{S(z)}$, which translates into an increase in the overall computational effort. Moreover, if the delay in the secondary path is greater than the one of the primary path, the adaptive filter is non-causal: causality problem is of great importance in broadband noise attenuation systems and will be discussed in sect. 1.6. Finally, an adaptive filter $W(z)$ must then be able to model both $P(z)$ and $S(z)$. The latter in particular can cause instabilities in the system if it goes to zero at certain frequencies. The secondary path has then to be compensated somehow with a modification of the control algorithm, switching from the LMS to the FxLMS one. In presence of a secondary path, the same computation considered in section 1.3 yields to the following residual noise expression:

$$e(n) = d(n) - y'(n) = d(n) - s(n) \star y(n) = d(n) - s(n) \star [\boldsymbol{w}^T(n)\boldsymbol{x}(n)] \tag{1.42}$$

Where $y'(n)$ is the control action which arrives to the cancelling station, while $s(n)$ indicates the impulse response of the secondary path $S(z)$. The "$\star$" indicates the convolution product. Since the secondary path will be assumed to be a FIR filter as well (see subsect. 1.4.1), its expression in time is a (time-invariant) vector $\boldsymbol{s}$. The convolution with $y(n)$ will be then performed as a dot product between $\boldsymbol{s}$ and the L_{iden} most recent outputs of the control, where L_{iden} is the length of the considered estimation filter.

The updating equation of $W(z)$ coefficients follows:

$$\boldsymbol{w}(n+1) = \boldsymbol{w}(n) + \mu e(n)\boldsymbol{x}'(n) \tag{1.43}$$

$\boldsymbol{x}'(n)$ is a vector containing the L most recent values of the convolution between the secondary path and the reference signal, namely:

$$\boldsymbol{x}'(n) = [\boldsymbol{s} \cdot \boldsymbol{x}(n),\ \boldsymbol{s} \cdot \boldsymbol{x}(n-1)\ ...\ \boldsymbol{s} \cdot \boldsymbol{x}(n-L)] \tag{1.44}$$

Equation 1.43 is the core of FxLMS-based algorithms. Its block diagram representation is given in fig. 1.15.

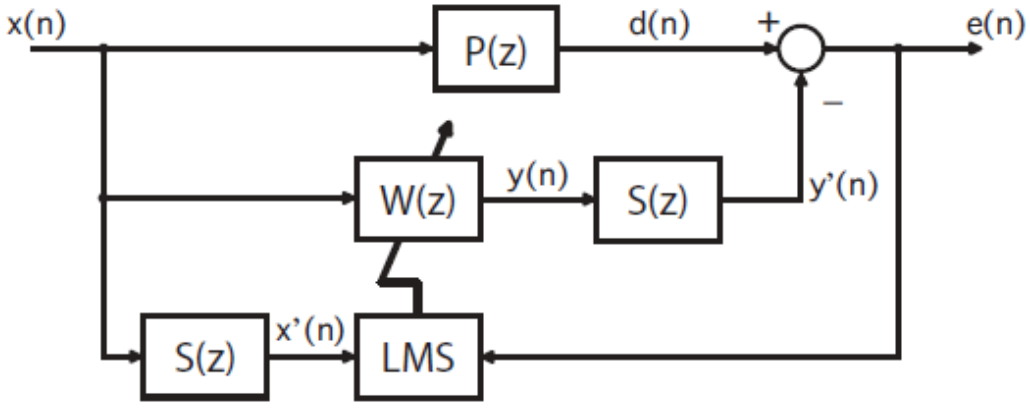

Figure 1.15: Broadband ANC system - Block diagram of FxLMS system

A similar compensation applies to narrowband systems as well [22].
Stability, convergence rate and excess steady error are the performances indicator for an FxLMS-based algorithm.
Stability is theoretically ensured by a maximum limit on the convergence rate:

$$\mu_{max} = \frac{1}{\sigma^2_{x'}(L + \Delta s)} \tag{1.45}$$

Where $\sigma^2_{x'}$ is the variance of the filtered reference signal and Δs is the overall delay in the secondary path expressed in number of samples. The secondary path delay negatively affects the stability and it may be reduced by decreasing the distance between the control loudspeaker and the error microphone, in addition with a reduction in the delay of the control system components.
A convergence rate indicator for broadband LMS-based algorithm can be analytically obtained as well.

The weight misalignment vector can in fact be written in terms of its modal representation: defining $\boldsymbol{Q}$ as the modal matrix formed by the eigenvectors of matrix $\boldsymbol{R}$ (which is the reference signal $\boldsymbol{x}(n)$ autocorrelation matrix), $\boldsymbol{v}(n) = \boldsymbol{w}(n) - \boldsymbol{w_0}$ and $\boldsymbol{v'}(n) = \boldsymbol{Q}^T\boldsymbol{v}(n)$, equation 1.46 holds:

$$v_i'(n) = (1 - \mu\lambda_i)^n v_i'(0) \tag{1.46}$$

Where λ_i is the $i-th$ eigenvalue of matrix $\boldsymbol{R}$ and $\boldsymbol{w_0}$ the optimal filter expression. Under the assumption of small μ, equation 1.46 becomes

$$v_i'(n) = e^{-\mu\lambda_i n} v_i'(0) \tag{1.47}$$

From eq. 1.47, the time τ_i in which each modal deviation v_i' is reduced by a factor equal to e (Nepero's number) can be estimated as:

$$\tau_i = \frac{T}{\mu\lambda_i} \tag{1.48}$$

Where T is the control sampling time. The convergence time is reduced by increasing μ as it may be expected, as well as increasing the control sampling frequency. In terms of subjective noise measures, a reduction by a factor e is equivalent to around $9dB$ of attenuation. Each mode will then converge differently, meaning that the slowest significant mode will determine the overall system stability. Eq. 1.48 can then be rewritten into:

$$\tau_{mse} \leq \frac{T}{\mu\lambda_{min}} \tag{1.49}$$

Where τ_{mse} is the maximum convergence rate dominated by the slowest mode, so by the minimum eigenvalue of $\boldsymbol{R}$, λ_{min}. The fastest convergence of the dominant mode is associated to $\mu = \frac{1}{\lambda_{max}}$, where λ_{max} is the maximum eigenvalue of matrix $\boldsymbol{R}$. Then;

$$\tau_{mse} \leq T\frac{\lambda_{max}}{\lambda_{min}} \tag{1.50}$$

Since the ratio between the maximum and minimum eigenvalue of $\boldsymbol{R}$ may not be precisely known, an estimate for the eigenvalue spread can be obtained by expression 1.51:

$$\frac{\lambda_{max}}{\lambda_{min}} \leq \frac{\max\limits_{\omega} |X(e^{j\omega})|^2}{\min\limits_{\omega} |X(e^{j\omega}|^2} \tag{1.51}$$

X is the reference signal Fourier transform and the spanned frequency range is from $\omega = 0$ to $\omega = 2\pi$. Eq. 1.51 shows that reference signals with flat spectra will be associated to the fastest convergence of the modes and thus of the control. Particular attention must then be payed since reference input signals in practice are typically filtered by anti-aliasing low-pass filters. Finally, the residual error after convergence can be estimated as:

$$\xi_{excess} = \frac{\mu}{2} L P_x \xi_{min} \tag{1.52}$$

ξ_{excess} is the difference between the estimated squared-error and ξ_{min}, which is the minimum theoretical value of ξ associated to the optimal condition $W(z) = W_0(z)$. P_x is the power of the reference signal. From eq. 1.52, an increase in the convergence rate results in larger excess error. Since increasing μ is equivalent to increase the convergence rate of the system, a trade-off in the tuning of the control parameters is required.
For an adaptive notch filter with $x_A(t) = Acos(\omega t)$, the convergence rate can be calculated as:

$$\tau_{mse} \leq \frac{2T}{\mu A^2} \tag{1.53}$$

While the stability constraint is:

$$\mu_{max} \leq \frac{4}{LA^2} \tag{1.54}$$

Even though these expressions are obtained for single-channel configurations under simplified assumptions, they can still be used as a guideline for the tuning of L and μ in more general cases.

1.4.1 Acoustical feedback and secondary paths estimation

A problem of major concern in broadband noise attenuation systems is in guaranteeing the reference microphone measure is as coherent as possible (see section 1.6). The coherence between the reference measure and the disturbance may drop due to the presence of the control action itself that may perturb the measure of $x(n)$. This effect is called acoustical feedback, and its consequences are particularly evident in small environments. Figure 1.16 shows how the acoustical feedback effect can be inserted into the previously discussed block scheme.

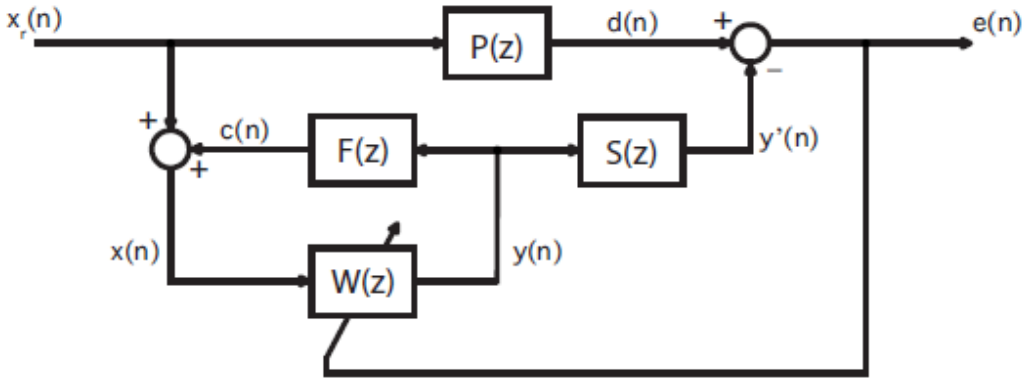

Figure 1.16: Block scheme with acoustical feedback loop

The transfer function $F(z)$ express the effect of the control action $y(n)$ at the reference microphone station. Due to the superposition principle, a perturbation signal $c(n)$ is added to the reference signal $x_r(n)$ yielding the reference microphone measure $x(n)$. Bode criteria states that instabilities can occur if the open-loop phase lag reaches 180° and the open-loop gain is greater than 1. The presence of a closed loop in the system then brings the control system from a feedforward configuration to a feedback one, so a way to compensate for the acoustical feedback introduction is then required to ensure stability. In figure 1.17 a compensation method (known as feedback neutralization) is presented.

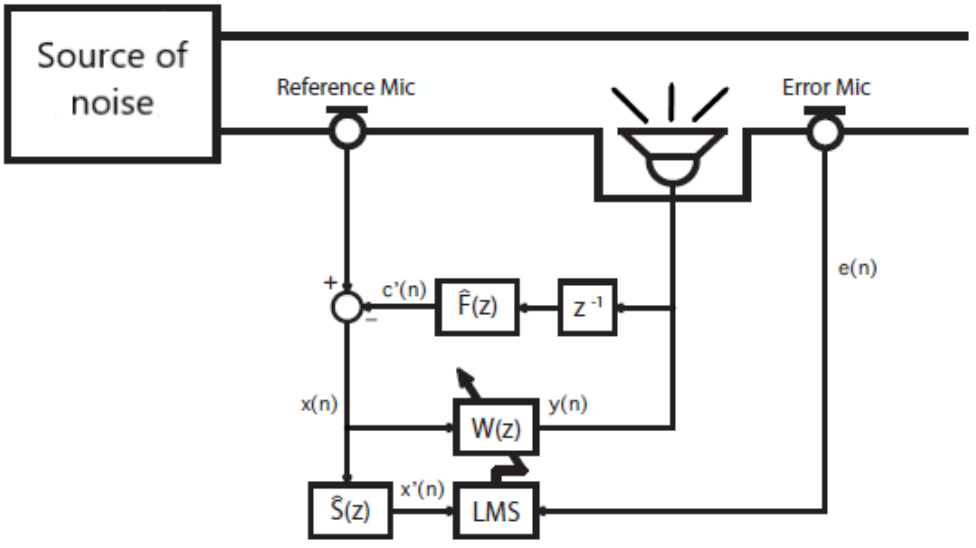

Figure 1.17: Control scheme with acoustical feedback compensation

Essentially, a signal $c'(n)$ is introduced to clean the corrupted measure of the reference microphone by the effect of the loop. Since the control action at time n is still not known from the control algorithm when this compensation is taking place, a discrete-time delay (the operation z^{-1}) is formally introduced to obtain $y(n-1)$.
Both $F(z)$ and $S(z)$ computation is then required in order to implement a broadband FxLMS control algorithm. Their estimates $\hat{F(z)}$ and $\hat{S(z)}$ can be obtained offline (prior to the control activation) by means of a process of identification on the basis of the very same LMS-based algorithm described in sect. 1.3. An offline identification process can be experimentally set by driving the control loudspeaker with broadband white noise. $\hat{F(z)}$ and $\hat{S(z)}$ can be estimated as adaptive FIR filters whose coefficients are automatically tuned by an LMS-based minimization algorithm in order to minimize two identification error measures (e_s and e_f), as shown in fig. 1.18.

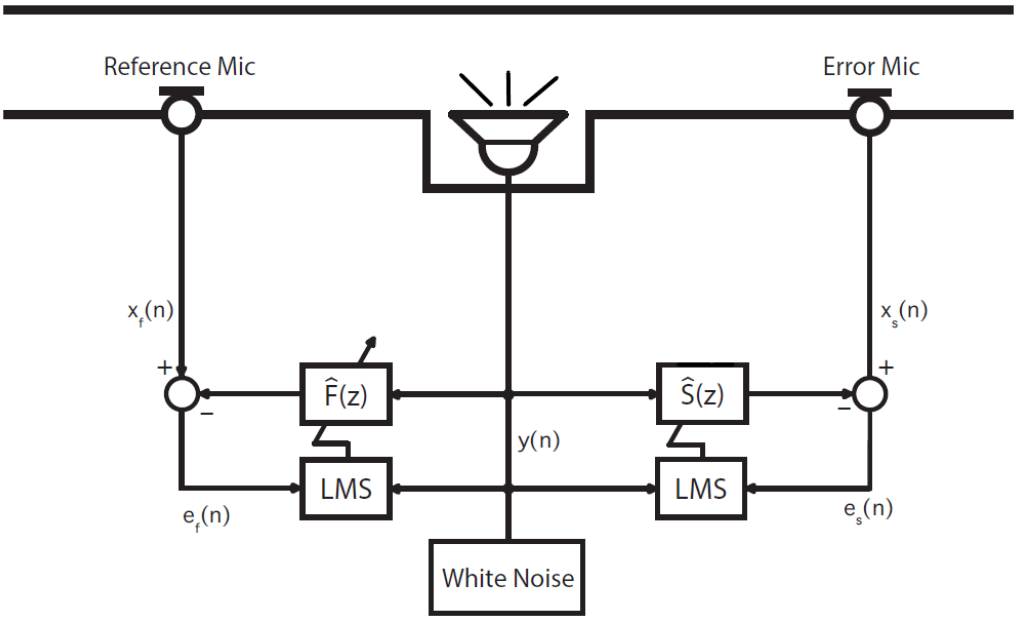

Figure 1.18: $S(z)$ and $F(z)$ identification process

An online identification may be performed in parallel with the control action in case of highly time-variant environments, at the cost of an increase in the computational burden.

1.4.2 Leaky-FxLMS algorithm

High noise levels associated with low frequency resonances can cause non-linear distortion by overloading the secondary sources. For this reason a common approach is to limit the control effort $y(n)$ by considering to weight it with a coefficient γ inside the cost function expression:

$$\xi(n) = e(n)^2 + \gamma y(n)^2 \tag{1.55}$$

γ has to be less to unity but close to it. This modifies the updating equation of the control filter coefficients into:

$$\boldsymbol{w}(n+1) = \nu \boldsymbol{w}(n) + \mu e(n) \boldsymbol{x'}(n) \tag{1.56}$$

Moreover, this formulation (leaky-FxLMS algorithm) also reduces numeric error in a finite-precision implementation. However, the introduction of leakage leads to an increased complexity of the weight update equation and the introduction of a bias into the solution. Moreover, a performance degradation is expected in terms of convergence rate.

1.5 Multi-channel ANC systems

When the unwanted noise is transmitted into multidimensional spaces in a complicated manner (typically large ducts or enclosures) multichannel ANC systems are typically required. They aim in exploiting multiple loudspeakers actions and reference microphones measures to reduce the overall noise in a set of error stations rather then at a single cancelling station, thus extending the region of attenuation of interest. While multichannel broadband noise attenuation is rather difficult due to the causality constraint (mainly due to relevant acoustical feedback paths presence and reverberant field perturbations of the reference microphones), narrowband noise cancelling in enclosures shows more promising results, particularly at frequencies near to the lowest resonances of the enclosure. If a sinusoidal primary source is placed in a 3D environment with volume V, the number of secondary sources needed to achieve perfect noise cancellation is equal to the number of the excited acoustic modes, which may be very large. It can be obtained as:

$$N_{modes} = \frac{4\pi V}{3c^2} f^2 \tag{1.57}$$

Eq. 1.57 states that the number of modes below a given frequency f shows a quadratic growth with respect to the frequency itself. This strengthens the fact that ANC systems are particularly effective at low frequencies only. Moreover, correct placement of the components is required by carefully placing control loudspeakers and reference microphones far from the modal nodes and near to the enclosure corners where the modal contribution factor is at its maximum. If possible, they should couple directly with the primary sources: in this case, the best performances can be obtained reducing the distance between noise source and control loudspeakers to less then a quarter - wavelength at the highest frequency. Finally, the coupling between sources radiation may severely affect the control performances. It depends on various factors, such as the relative distance, the wavelength and the relative source strength. Another important aspect to consider is that in closed environments local noise attenuation shows better performances with respect to global one, in particular at low frequencies. All these aspects must be taken into account to formulate an effective design.
Both the control schemes and updating equations for a multichannel control system are presented in section 2.1, with reference to the particular solution adopted for this Thesis. The results are anyway generalizable to any control configuration, thus only some principles will be remarked here. A way to define the cost function over an acoustical space of volume V is:

$$E_p = \frac{1}{4\rho_0 c^2} \int_V |p|^2 dV \tag{1.58}$$

Approximating the pressure field with M error microphones:

$$E_p = \xi = \frac{V}{4\rho_0 c^2 M} \sum_{m=1}^{M} |p_m|^2 dV = \frac{V}{4\rho_0 c^2 M} \boldsymbol{e}^T \boldsymbol{e} \tag{1.59}$$

Where $\boldsymbol{e}$ is a vector containing the error pressures. M (the number of error sensors) should be sufficiently high to correctly represent the sound field in volume V, but in practice this value is limited by the processing power at disposal. Considering K secondary sources, and defining $\boldsymbol{Z}$ as the $K \times M$ acoustic transfer impedance matrix, $\boldsymbol{p_p}$ as the unknown vector of pressures at the M discrete error positions due to the primary sources and $\boldsymbol{q_s}$ the vector of K secondary sources control volume velocities, exploiting the superposition principle:

$$\boldsymbol{e} = \boldsymbol{p_p} - \boldsymbol{Z}\boldsymbol{q_s} \tag{1.60}$$

The consequence of equations 1.59 and 1.60 is that ξ results to be a quadratic function of the individual source strengths. This allows the implementation of a gradient descent method-based optimization. In fact, minimizing ξ is equivalent to minimize the following cost function:

$$\hat{\xi}(n) = \boldsymbol{e}(n)^T \boldsymbol{e}(n) \tag{1.61}$$

In analogy with what presented in sect. 1.3, the expression in equation 1.61 can be seen as the algebraic sum of the Widrow approximation of M expected values of squared error pressures, thus leading to a completely analogous formulation with respect to the single-channel ANC system case study. In presence of J reference signals (both non-acoustic sensors or microphones for broadband noise attenuation), $K \times J$ adaptive FIR filters are required to be updated for real time noise control and $M \times K$ secondary paths require to be estimated. In addition, each acoustical reference sensor requires the estimation of K acoustical feedback paths. A view of a generic multichannel ANC system is given in fig. 1.19.

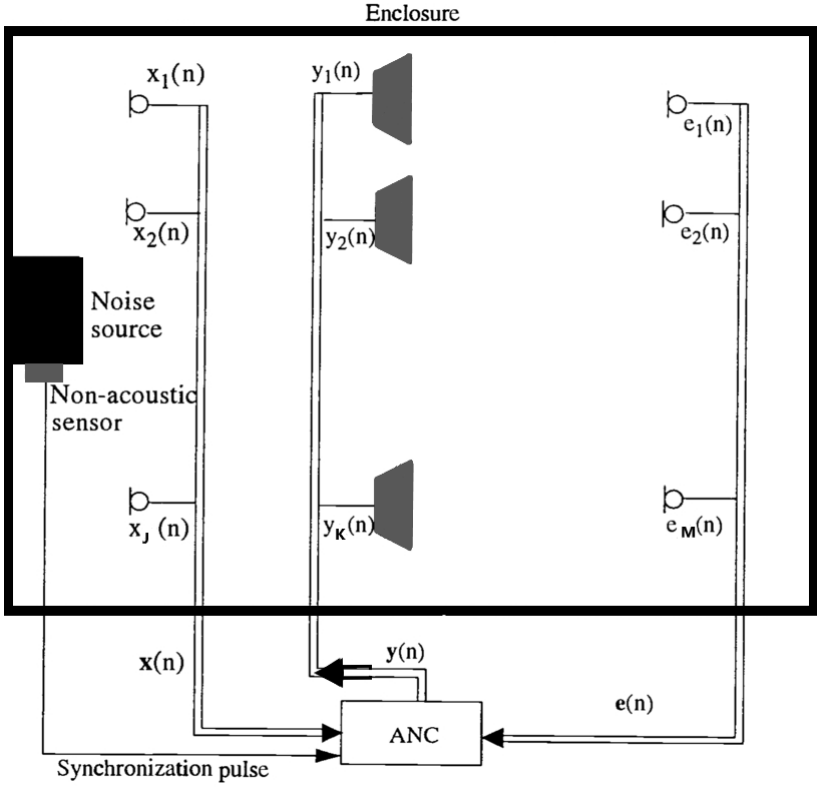

Figure 1.19: Multichannel ANC system

In terms of modal representation, minimizing E_p is equivalent to minimizing the sum of the squares of the (complex) acoustic mode amplitudes. Thus pressure cancelling at M positions is equivalent to eliminating M acoustic modes. From expression 1.60, it follows that multiple-channel control problem is consistent when $K \geq M$, otherwise it is not possible to control the error pressure at all the M stations. Choosing $K = M$ leads to the optimal solution

$$\boldsymbol{q_s} = \boldsymbol{Z^{-1}} \boldsymbol{p_p} \tag{1.62}$$

Eq. 1.62 shows it is possible to control the most significant M modes under this condition. However, the secondary sources may significantly excite other additional modes. This effect is termed "control spillover". For this purpose, $K > M$ is typically required to control both the first M acoustic modes and the next $K - M$ ones altogether.

1.6 Practical considerations

Some aspects have to be taken into account for practical implementation of an active noise control based on the previously presented algorithms. For a broadband noise control system the coherence between the reference signal and the disturbance $d(n)$ directly affects the performance. The autopower spectra of the error signal can be calculated as:

$$S_{ee}(\omega) = [1 - C_{dx}(\omega)] S_{dd}(\omega) \tag{1.63}$$

Where C_{dx} is magnitude squared coherence between reference signal and disturbance, and S_{dd} the autopower spectra of the disturbance. Eq. 1.63 shows that enhancing the coherence between $x(n)$ and $d(n)$ will be beneficial in the minimization of the residual error. As a consequence, turbulent noise, flow noise or any other source of uncorrelation can limit the attenuation. Coherence can be enhanced reducing the flow velocity (for duct noise application), using multiple and distributed error microphones and by proper design of the duct/enclosure and placement of the sensors themselves. However, measurement errors at the error microphones do not directly contribute to the degradation in the stability.
In addition to measurement errors, modeling errors can significantly degrade the control performances.

They essentially consist in estimation errors in $\hat{S(z)}$. For a narrowband reference signal, a broadband disturbance and small convergence rate, it can be shown that stability can be achieved when the phase difference between $S(z)$ and $\hat{S(z)}$ is between -90° and 90°. Modelling errors can be reduced using high-order estimation filters.
Causality is another important aspect to take into account. The controller has to be able to perform all of its operations and transmit the control action in a smaller time with respect to the one requested by the acoustical wave to propagate from the reference microphone to the error one. In other words, the acoustical delay must be greater then the electrical one (which can be estimated to be proportional to the sampling time), otherwise the wrong control signal will be continuously provided as secondary source action. This is the reason why greater performances can be achieved in long ducts rather then small enclosures, when the source emits random noise. However, when non acoustical sensors are considered (as for narrowband periodic noise cancellation) causality is not a problem and greater performances can be obtained even in small environments.

Chapter 2

The proposed noise control algorithm

In this chapter an active control system is presented as a solution for the creation of an optimized silentseat for propeller-induced noise. It consists in a multi-channel configuration with four control loudspeakers and four error microphones. It is driven by two multi-component narrowband reference signals in quadrature to realize an adaptive notch filter, and a broadband measure from a reference microphone, leading to a $3 \times 4 \times 4$ active noise control configuration. The resulting algorithm is shown, discussed and tested by performing numerical simulations in various conditions, in order to assess its capabilities in terms of stability and achievable performances.

2.1 Algorithm description

The algorithms written for this activity incorporate all the active noise control theory that has been summarized up to this point. Since the aim is to provide narrowband noise attenuation, two sinusoids in quadrature, namely $x_A(n)$ and $x_B(n)$, are given as multi-component reference signals. A third reference signal, $x_{rif}(n)$, is the output of a reference microphone and it has been added to enhance the robustness of the solution. Its effects are investigated in section 2.2. They drive a configuration consisting in four control loudspeakers and four error microphones.

The updating is based on the conventional leaky-FxLMS algorithm, taking into account the acoustical feedback effect on the reference microphone. For this configuration, 12 FIR filters W_{ij} then need to be updated in real time for the loudspeakers to adaptively provide four outputs ($y_1(n)$, $y_2(n)$ $y_3(n)$ and $y_4(n)$) capable of minimizing the acoustical pressure at four error microphones, indicated as $e_1(n)$, $e_2(n)$, $e_3(n)$ and $e_4(n)$. As discussed in section 1.4, the loudspeakers outputs are physically filtered by secondary acoustical paths which results in a change of the control actions into $y'_1(n)$, $y'_2(n)$ $y'_3(n)$ and $y'_4(n)$ at the cancelling stations. From what stated instead in sect. 1.5, the number of loudspeakers (K) must be equal or greater then the number of error microphones (M). In this case, $K = M = 4$, which implies the control spillover effect won't be removed, if present.
An identification scheme is then performed offline prior to the control. This is typical of cases in which the plant physics can be considered time - invariant. The identification of 16 secondary paths S_{ij} is required. They correspond to any of the transfer functions between each control loudspeaker and each error microphone. In addition, 4 FIR filters F_i are required to identify the acoustical feedback paths. Estimates are provided by means of the LMS algorithm: 20 filters are adaptively updated by driving the loudspeakers with broadband white noise. In figure 2.1 the identification scheme is represented by means of a Simulink block diagram scheme. As it can be seen, four gaussian white noise signals are numerically or experimentally generated to drive each loudspeaker. An associated disturbance can then be measured at the error microphones stations. The very same input is given to the estimated secondary paths as well : their outputs are then summed at each error microphone to provide the final action of any loudspeaker at each cancelling station. The difference between the real disturbance and the estimated filter output at each error station provide four identification errors that are used by the algorithm for the updating of the identification filters. The estimation block is represented in fig. 2.2.

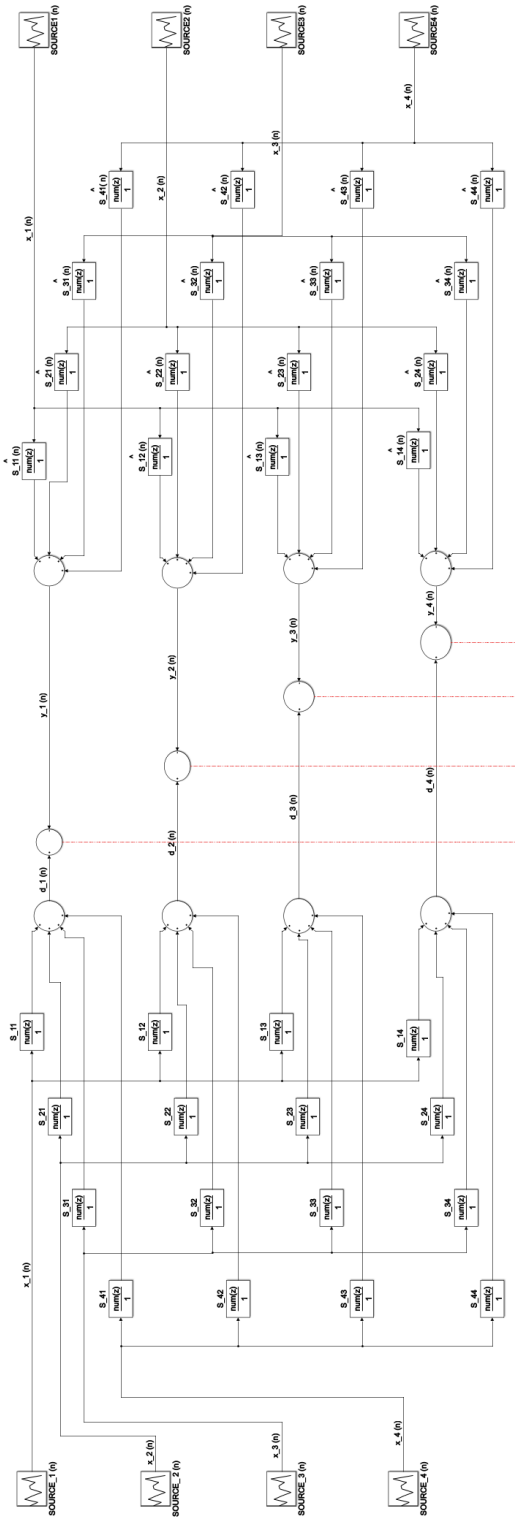

Figure 2.1: Secondary paths identification - Scheme

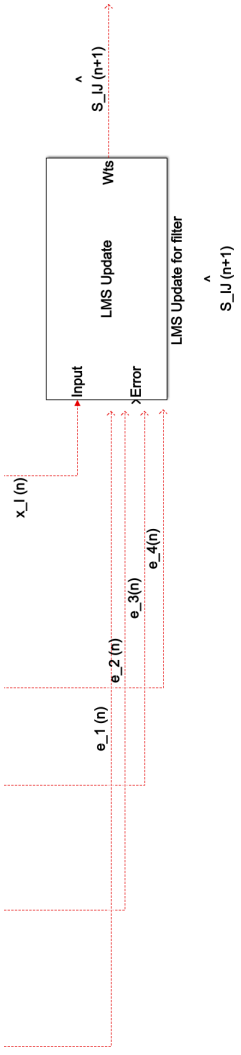

Figure 2.2: Secondary paths identification - Leaky LMS block

The updating equation for the $ij-th$ acoustical secondary path is thus

$$\hat{S_{ij}}(n+1) = \hat{S_{ij}}(n) + \sum_{k=1}^{M=4} \nu_{iden}\ \mu_{iden}\ \boldsymbol{x_i}(n)\ e_k(n) \tag{2.1}$$

where $\boldsymbol{x_i}(n)$ is the vector containing the most recent L_{iden} values of the white noise reference signal of source i. L_{iden} is the length of the identification filters.

The estimation scheme of the acoustical feedback path from the four control loudspeakers to the reference microphone is represented in figure 2.3.

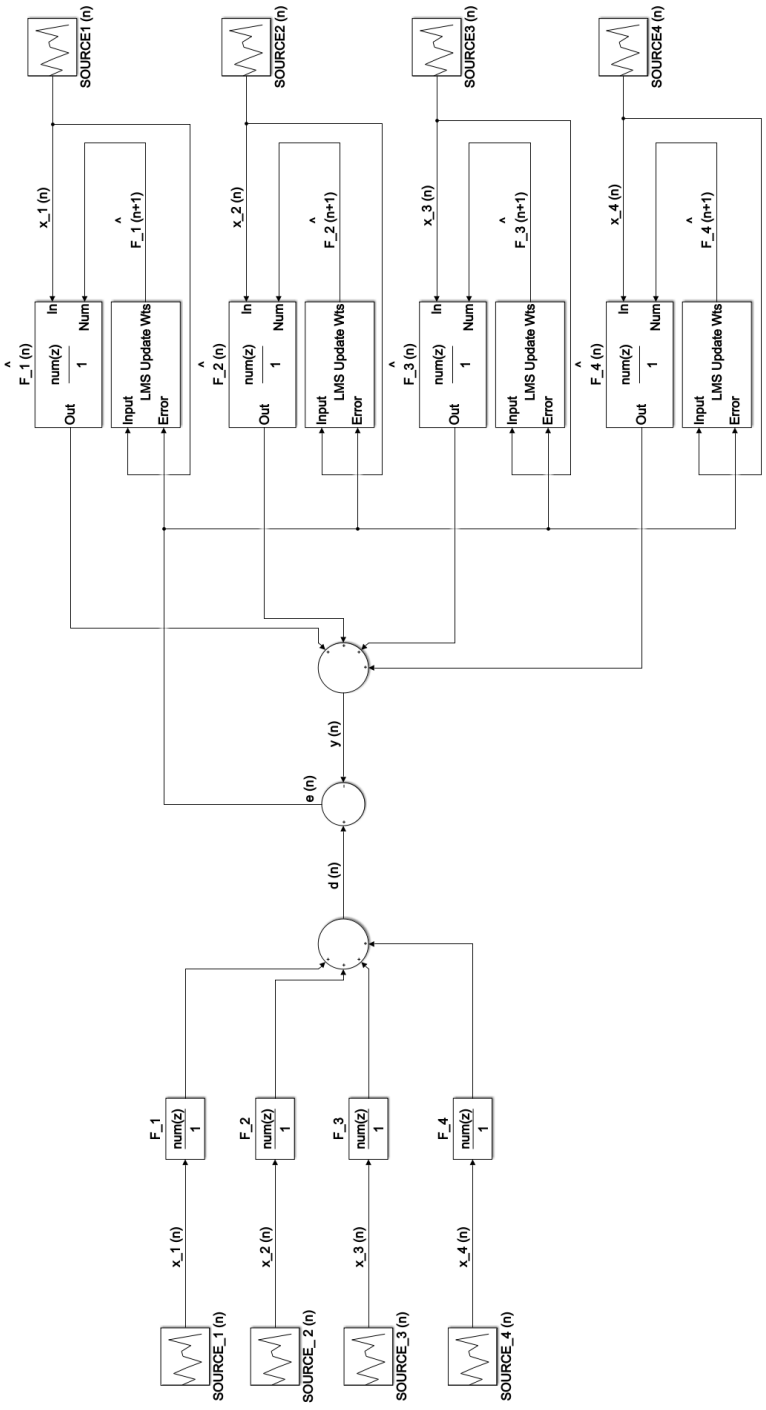

Figure 2.3: Acoustical feedback identification

In analogy with the secondary paths identification, white noise is experimentally or numerically generated by the control loudspeakers and recorded at the reference microphone station. The same white noise input is filtered by four identification FIR filters. Their outputs are then summed to give an overall output at the reference microphone station. The difference between the recorded disturbance and the estimation filters output is the identification error that is sent to the updating algorithm of the acoustical feedback filters $\hat{F}_i$. The updating equation is then

$$\hat{F}_i(n+1) = \hat{F}_i(n) + \nu_{iden}\ \mu_{iden}\ \boldsymbol{x_i}(n)\ e(n) \tag{2.2}$$

The identification process is performed over a time T_{iden}. The final performances can be evaluated by plotting the identification error in time, checking the effective attenuation of the pressure at the corresponding microphone station.
The control algorithm is shown in figure 2.4. The aforementioned reference signals are given to the control filters W_{ij} to provide 12 control outputs. These are then summed in order to generate a resulting action associated to any secondary source. Each of these actions can affect the acoustical pressure at any error microphone, which is described by the $\hat{S_{ij}}$ transfer function estimated during the previous identification session. The summation of all the filtered outputs coming from each loudspeaker and arriving to a certain error station is the control output arriving at the given cancelling microphone. The difference between the disturbance pressure and the control output at this station is the control error to be minimized. The detail on the acoustical feedback is given in fig. 2.5. The reference signal used for control purposes is then cleaned from the perturbation induced by the secondary sources. The control filters updating is based on a leaky-FxLMS algorithm and it is performed over a time T_{contr}. The updating block is shown in fig. 2.6.
The updating equation for filter W_{ij} is:

$$W_{ij}(n+1) = W_{ij}(n) + \sum_{k=1}^{M=4} \nu_{contr}\ \mu_{contr}\ \boldsymbol{x'_{ijk}}(n)\ e_k(n) \tag{2.3}$$

Where $\boldsymbol{x'_{ijk}}(n) = \hat{S_{jk}} \cdot \boldsymbol{x_i}(n)$, with $\boldsymbol{x_i}(n)$ defined as the vector containing the L_{contr} most recent values of the reference signal $x_i(n)$.

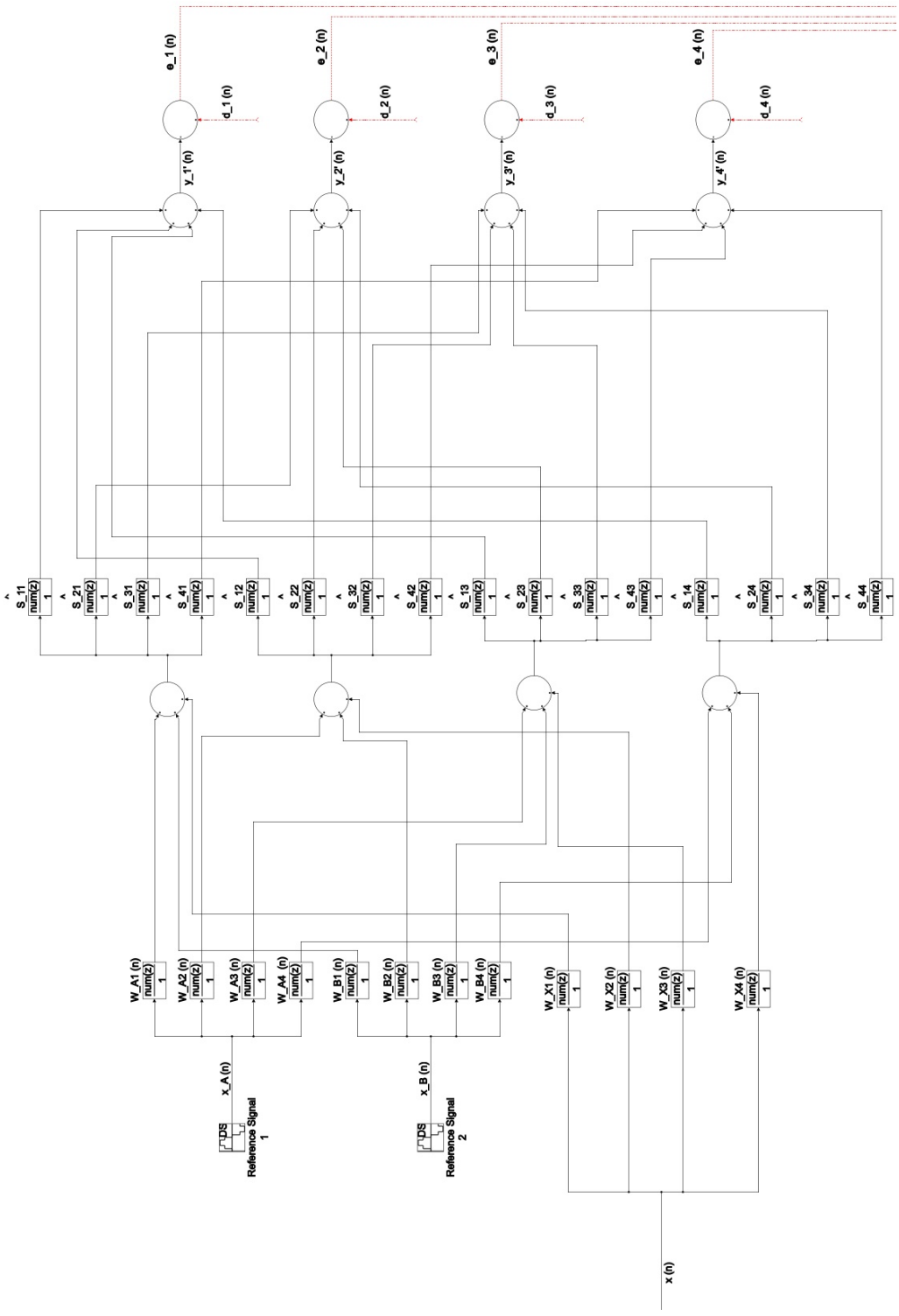

Figure 2.4: Proposed control algorithm - Scheme

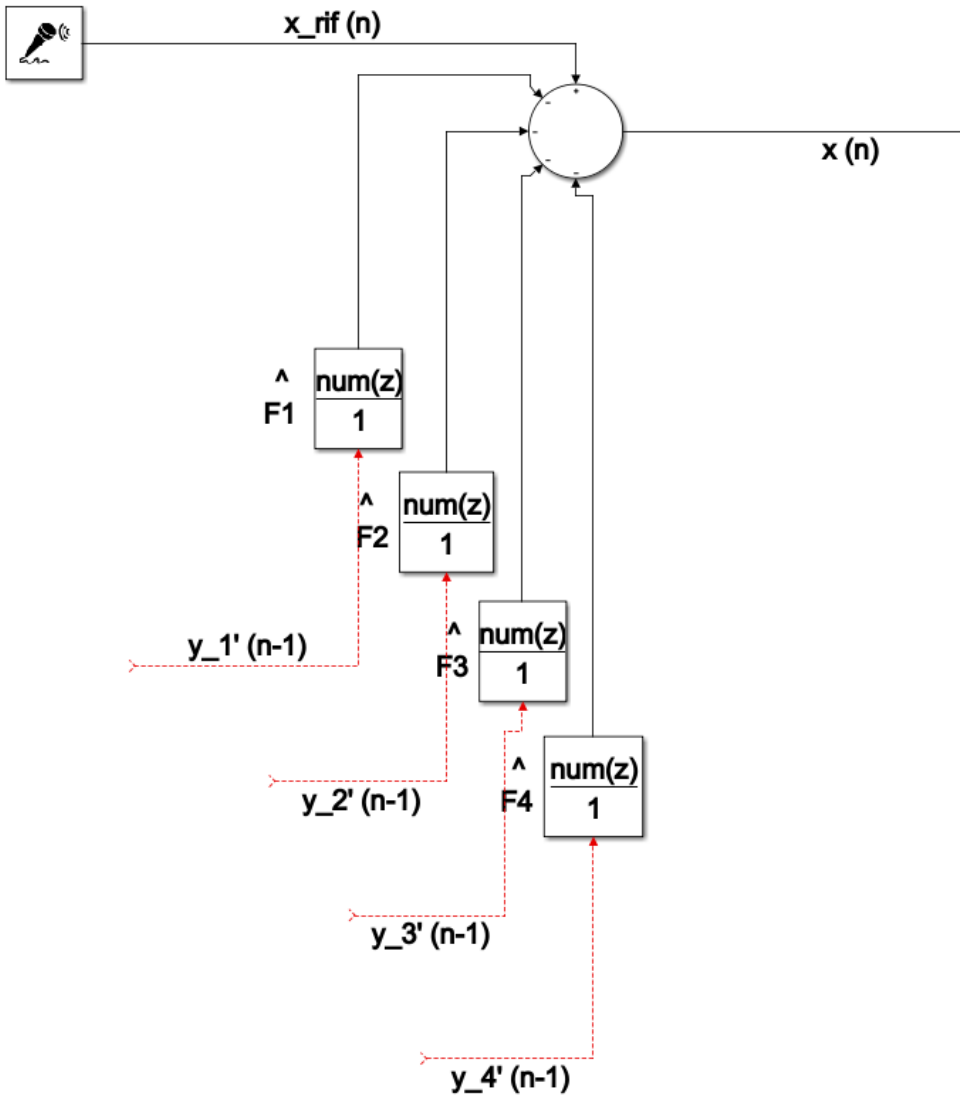

Figure 2.5: Acoustical feedback path compensation

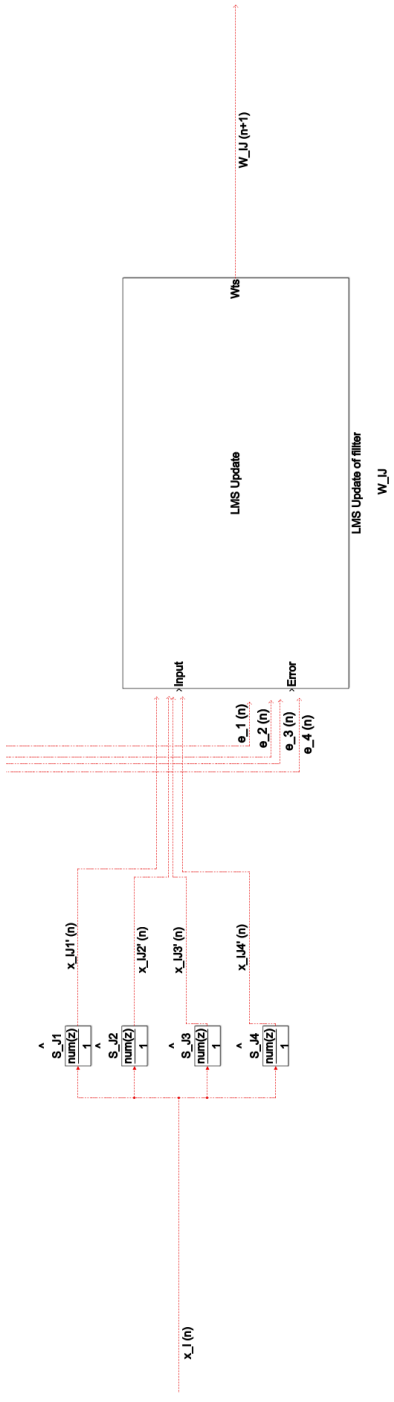

Figure 2.6: Control filters updating - Leaky FxLMS block

In order to give an insight on the algorithm computational cost, roughly $68L_{iden} + 24L_{contr}$ sums and $68L_{iden} + 60L_{contr}$ multiplications are needed per control sample, as well as 5 acoustical pressure acquisitions and a tachometer measure.

2.2 Numerical simulations

Numerical tests with simple input signals are performed in order to check for the correct implementation of the identification and control algorithms and provide a general view on the obtainable performances in different working conditions.

2.2.1 Analysis parameters

A set of primary paths is required to numerically generate the disturbance at the error stations to be minimized. For the following analysis, the primary paths to be considered are four 7-tap FIR filters with the following expressions:

$$P_1 = [\ 0.01\ 0.25\ 0.5\ 1\ 0.5\ 0.25\ 0.01\ ]$$

$$P_2 = 0.9\ P_1$$

$$P_3 = 1.1\ P_1$$

$$P_4 = 1.2\ P_1$$

The sampling frequency is set to $3kHz$.

2.2.2 Secondary and feedback acoustical path identification

The identification phase aims to find a total of 20 FIR filters estimating the secondary and acoustical feedback paths, which have been indicated as $\hat{S_{ij}}$ and $\hat{F_i}$, with $i, j = 1 : 4$.
In order to check the algorithm tracking capabilities, a set of exact secondary paths has been :

$$S_{ij} = 0.25\ P_1\ when\ i = j$$

$$S_{ij} = 0.1\ P_1\ when\ i \neq j$$

While for the feedback paths:

$$F_i = 0.1\ P_1$$

The loudspeakers input is zero-mean gaussian white noise. The total time for the identification is set to $5s$. The parameters for the filter coefficients updating are: $L_{iden} = 28$, $\mu_{iden} = 0.001$ and $\nu_{iden} = 0.999999$. It is also assumed that a random value ranging from -5% to $+5\%$ on the pressures at the error and reference microphones is added as measurement error. Figure 2.7 - 2.11 show the residual noise at the cancelling and reference microphones during time, while figure 2.12 - 2.16 show the deviation of the estimated coefficients with respect to the exact ones.
As it can be seen from the obtained results, the estimation of the secondary paths coefficients can lead to errors up to 44 % on some filter coefficients. This is due to the minimization scheme itself, which in presence of different secondary paths tries to converge to a single mean set of coefficients in a least square approach. The system is in fact overdetermined, since 16 coefficients are to be found but only 4 error measures are used. It can be verified that in the case of 16 identical secondary paths the estimation precision drastically increases: small deviations of a secondary path with respect to another can be obtained by reducing the differences in the audio chain (for instance using four identical loudspeakers) and focusing on small regions in space, which is the case of local active noise control. For this very same reason, the acoustical feedback estimation shows noticeably lower estimation errors : the system is in this case perfectly determined, since 4 filters are to be found relying on 4 error measures. More on the identification of acoustical paths in multi-channel control systems can be found in [8].

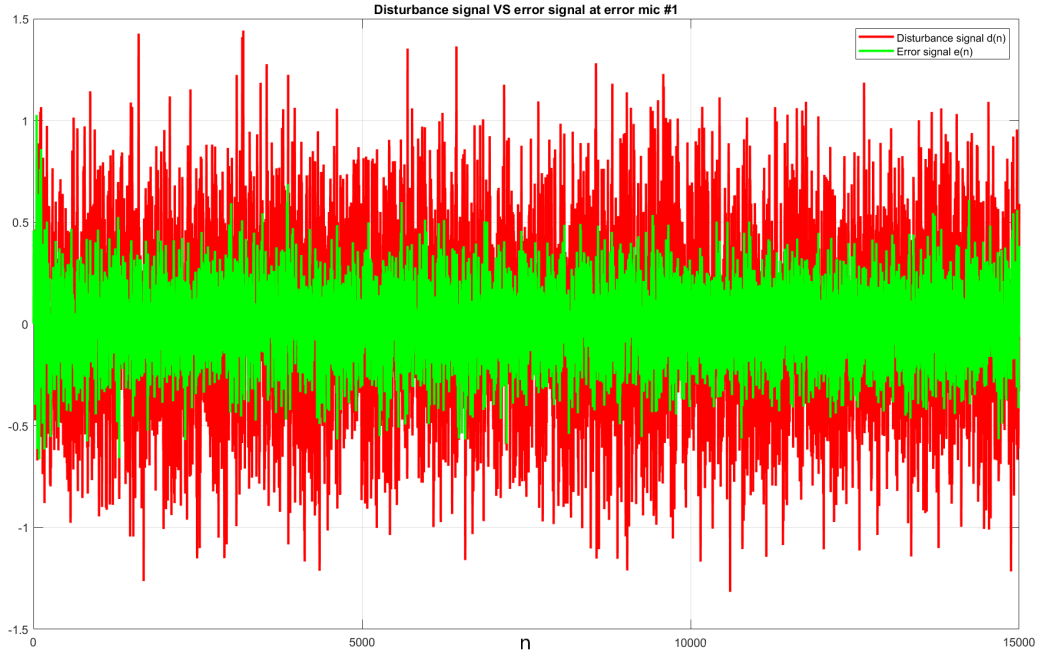

Figure 2.7: Identification disturbance and error - Error microphone # 1

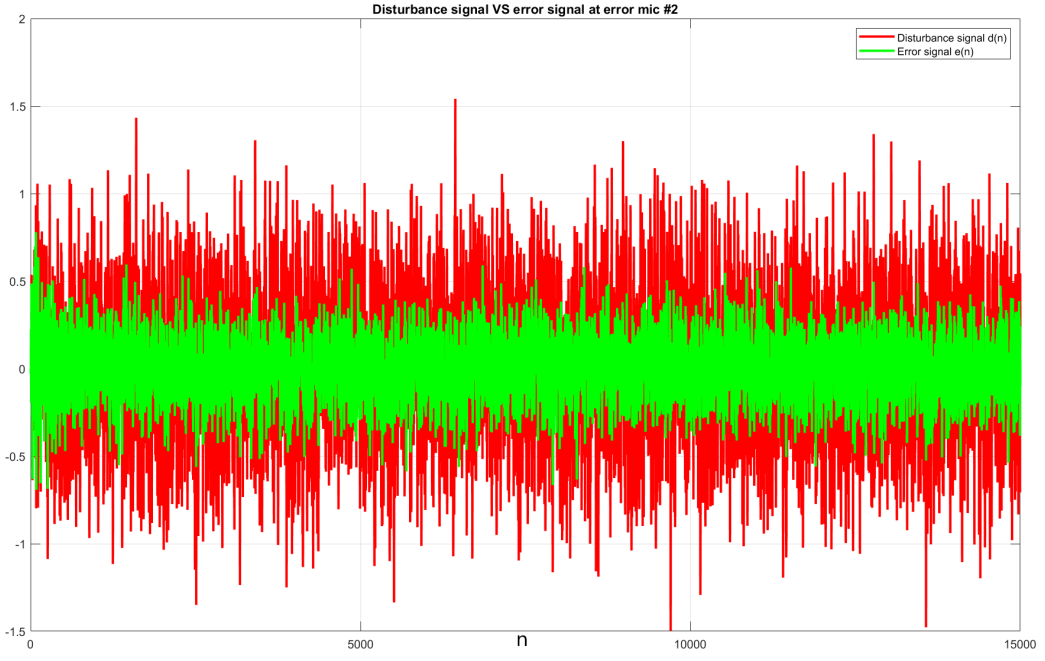

Figure 2.8: Identification disturbance and error - Error microphone # 2

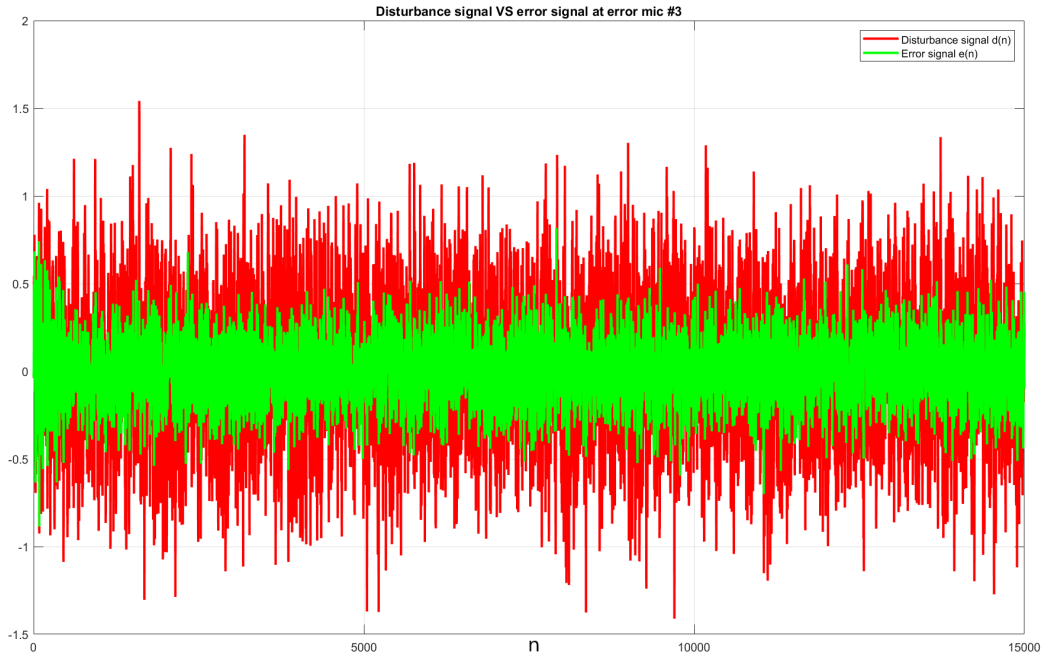

Figure 2.9: Identification disturbance and error - Error microphone # 3

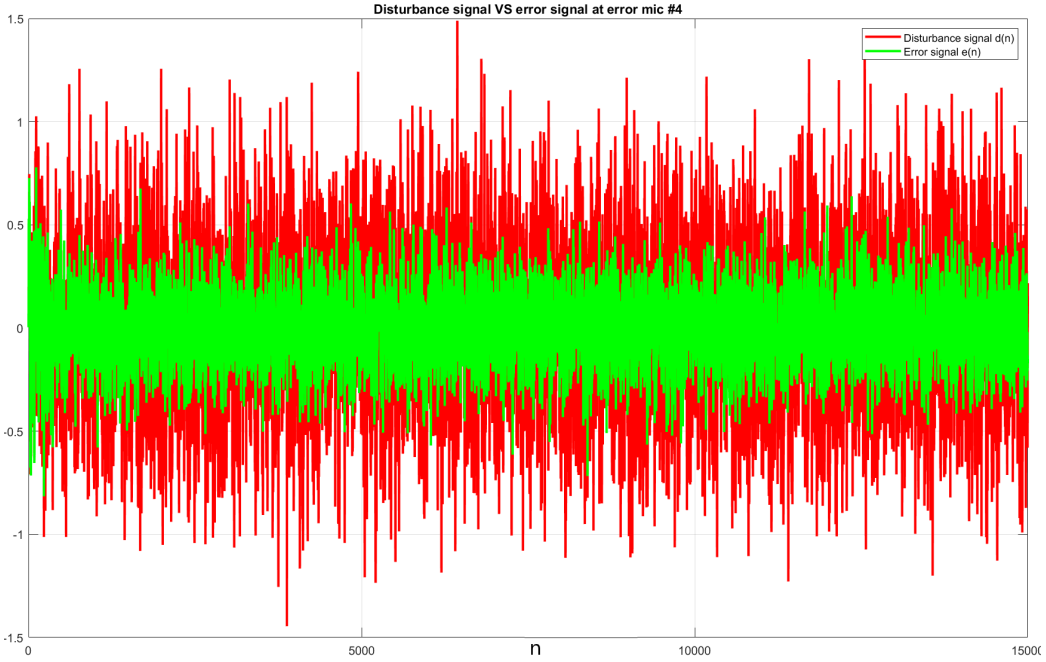

Figure 2.10: Identification disturbance and error - Error microphone # 4

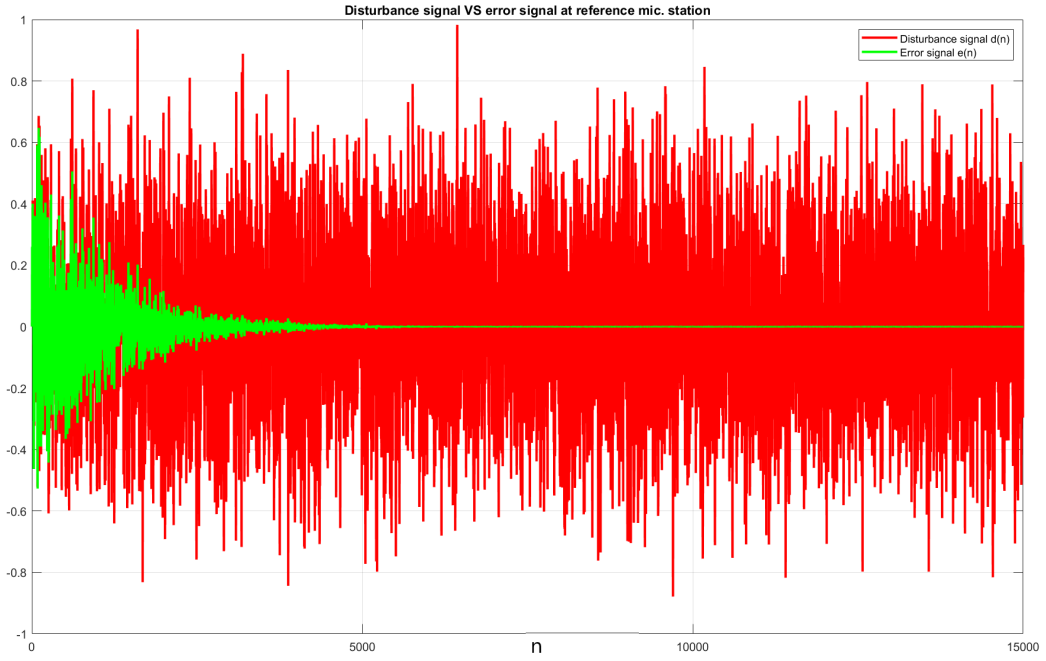

Figure 2.11: Identification disturbance and error - Reference microphone

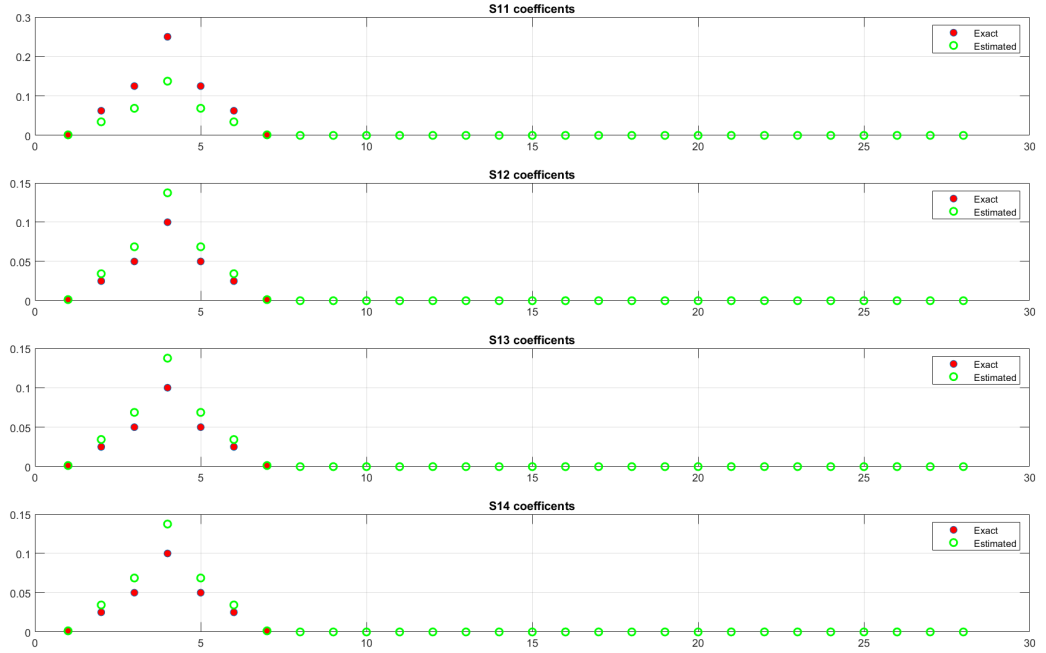

Figure 2.12: S11-S14 coefficients

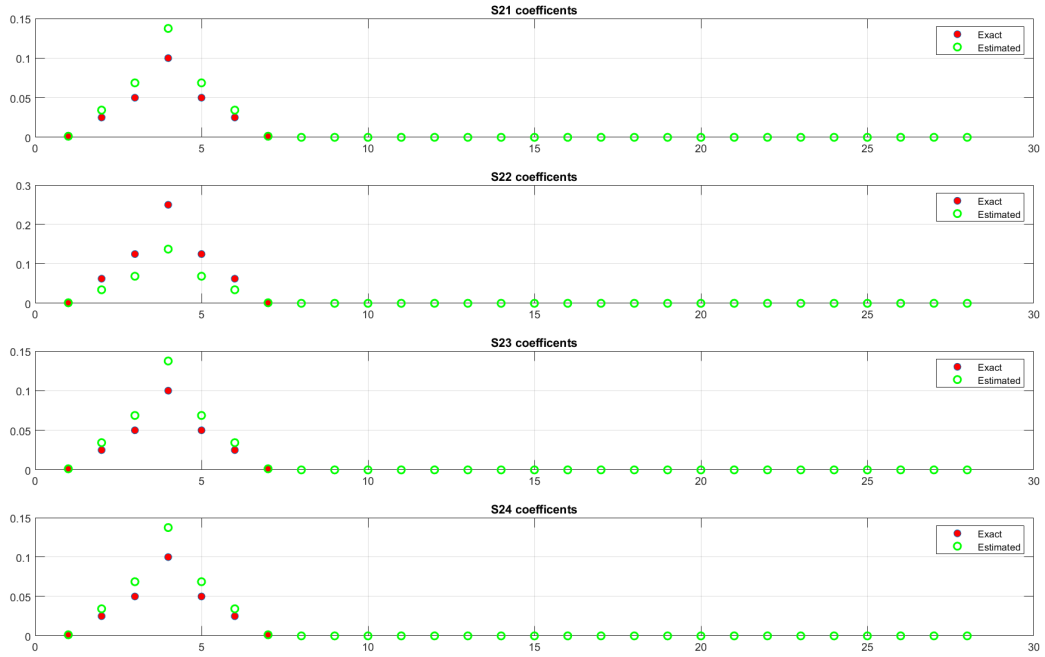

Figure 2.13: S21-S24 coefficients

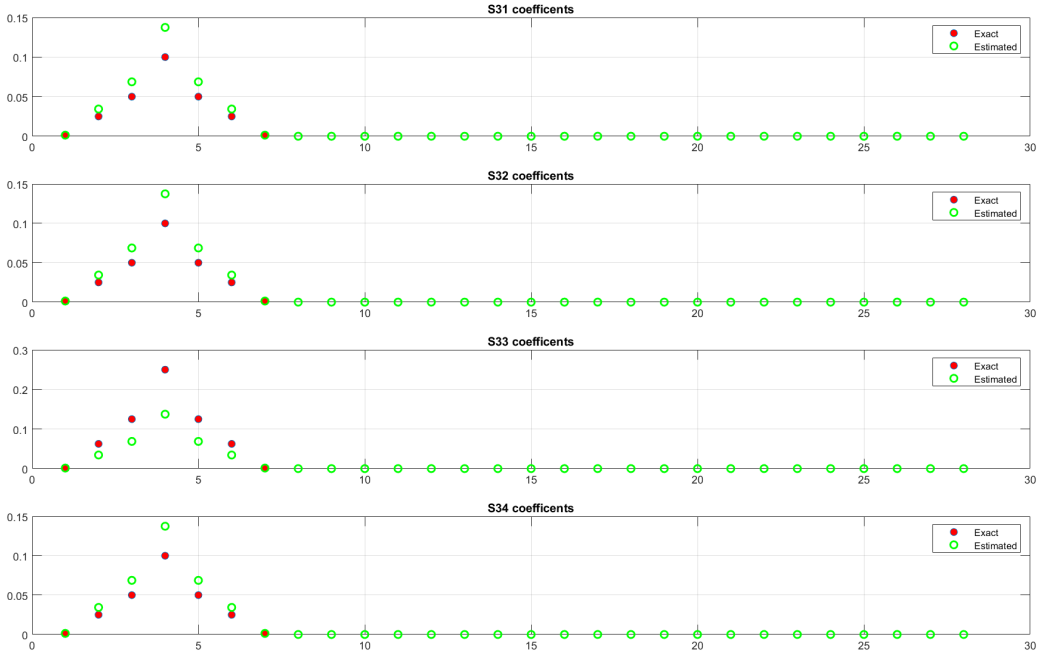

Figure 2.14: S31-S34 coefficients

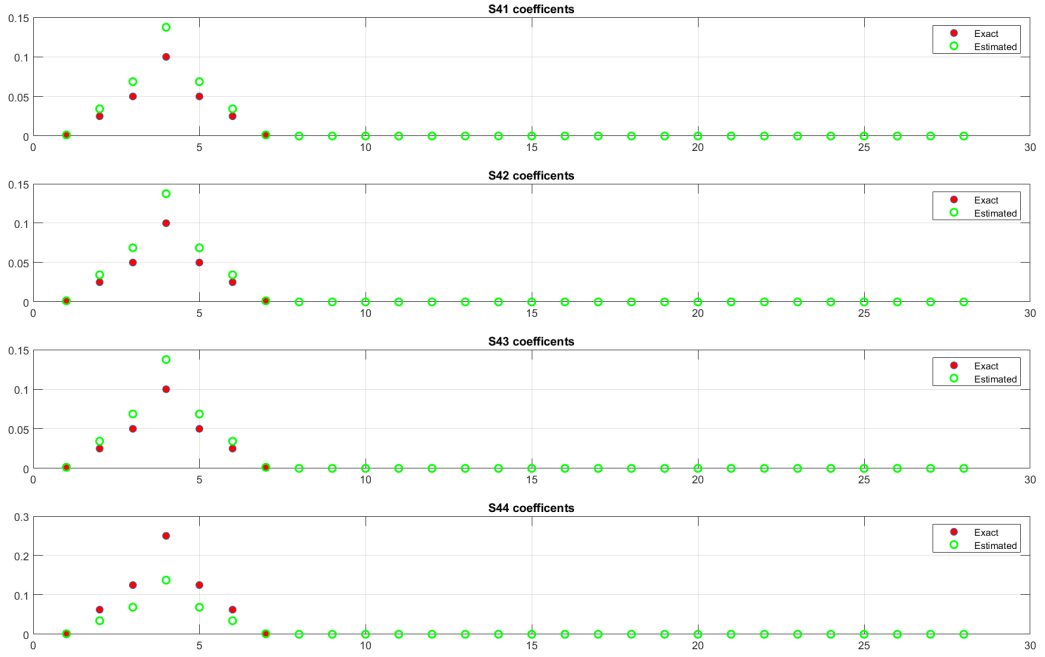

Figure 2.15: S41-S44 coefficients

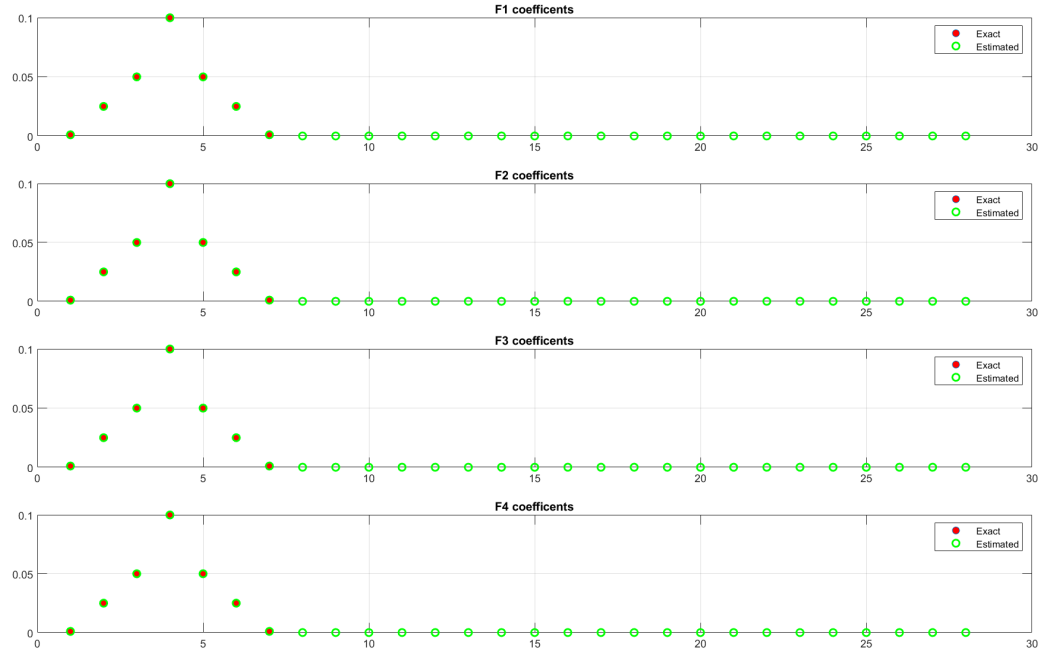

Figure 2.16: F1-F4 coefficients

2.2.3 Numerical tests with stationary reference signal

A narrowband multicomponent reference signal is defined as a noise source with four tones at 50, 75, 100 and $150Hz$, corresponding to a fundamental frequency $f_0 = 50Hz$ and three additional harmonics, namely $1.5f_0$, $2f_0$ and $3f_0$. These peaks are considered to be fixed in time, which may be the case for an engine regime condition. Broadband noise up to $400Hz$ is also added. Its frequency content is shown in fig. 2.17.

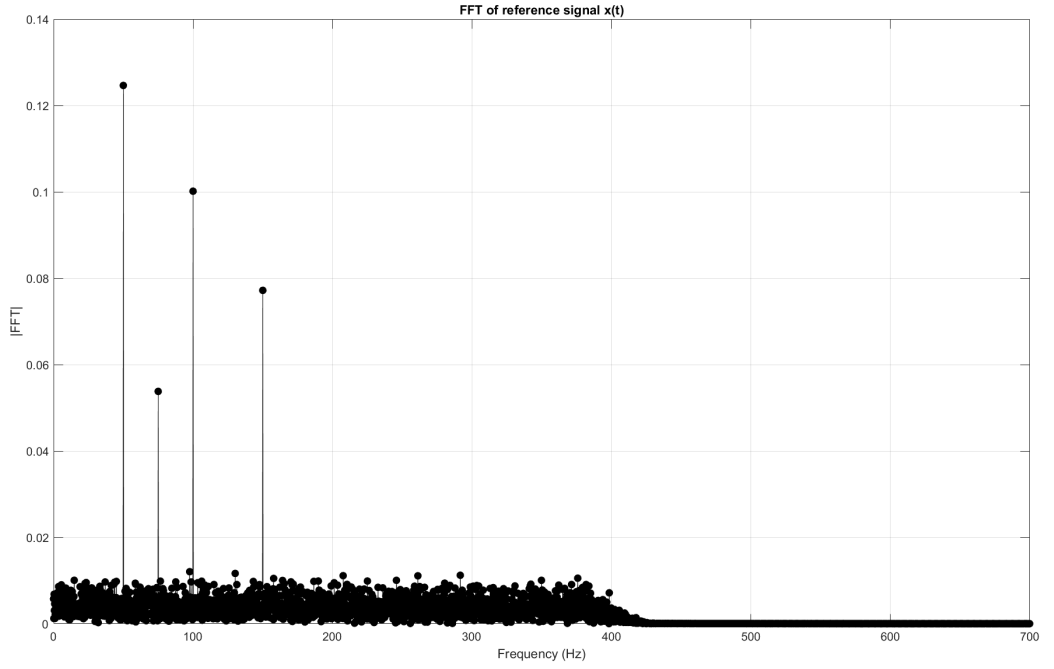

Figure 2.17: Reference noise signal frequency content

The narrowband reference signals are

$$x_A(n) = \sum_{m=1}^{4} A_m \; cos(\omega_m \; n) \tag{2.4}$$

and

$$x_B(n) = \sum_{m=1}^{4} B_m \; sin(\omega_m \; n) \tag{2.5}$$

with $A_1 = B_1 = 0.6$, $A_2 = B_2 = 0.1$, $A_3 = B_3 = 0.05$ and $A_4 = B_4 = 0.05$. $x_A(n)$ and $x_B(n)$ are in quadrature, as for an adaptive notch filter for single frequency attenuation.

For real time applications, cosine signals can be generated by different approaches, such as lookup tables implementation or digital resonators. A 90° phase difference signal can be obtained by means of a digital Hilbert transform filter [8]. The third reference signal, $x_{rif}(n)$, is set equal to the noise directly generated by the noise source, thus $x_{rif}(n) = x(n)$. This assumes the reference microphone provides a perfectly correlated measure of the noise source, which is hardly the case in real practical applications.
The control parameters are $L_{contr} = 220$, $\mu_{contr} = 0.0004$ and $\nu_{contr} = 0.999999$. The total control time is $5s$. A random measurement error ranging from -5% to $+5\%$ is added to the pressures at the error and reference microphones.
The disturbance and residual signals at the cancelling microphones are plotted in fig. 2.18 - 2.25, both in time and frequency domain to fully appreciate the stability and attenuation performances. Frequency spectra in decibels (SPL) is evaluated with formula 1.29.

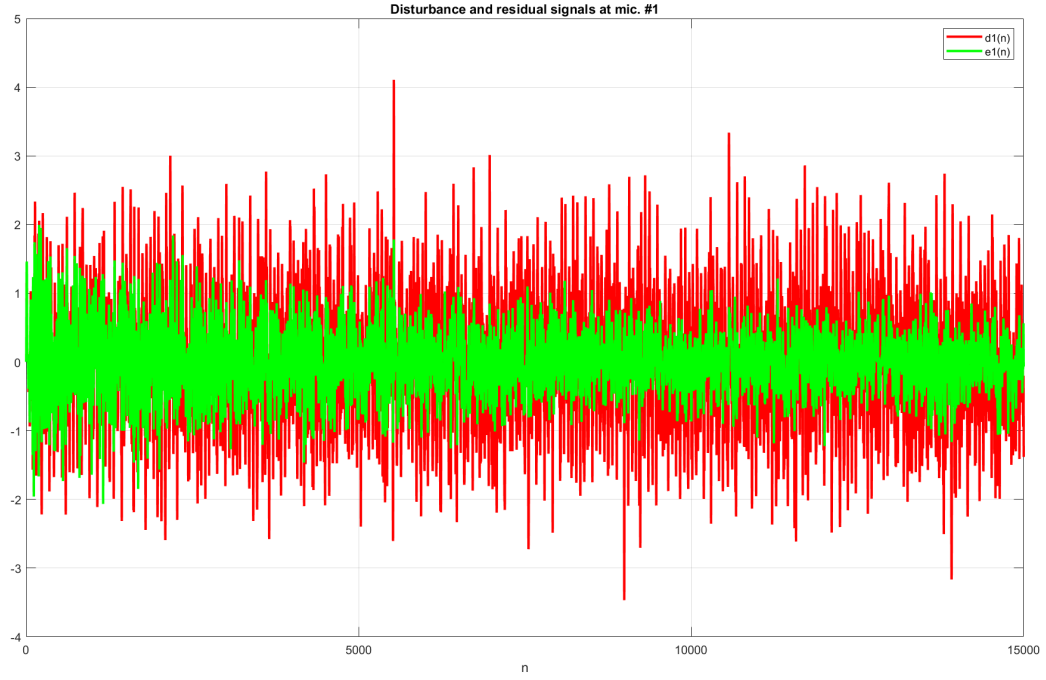

Figure 2.18: Disturbance and error signal at error microphone # 1, time domain

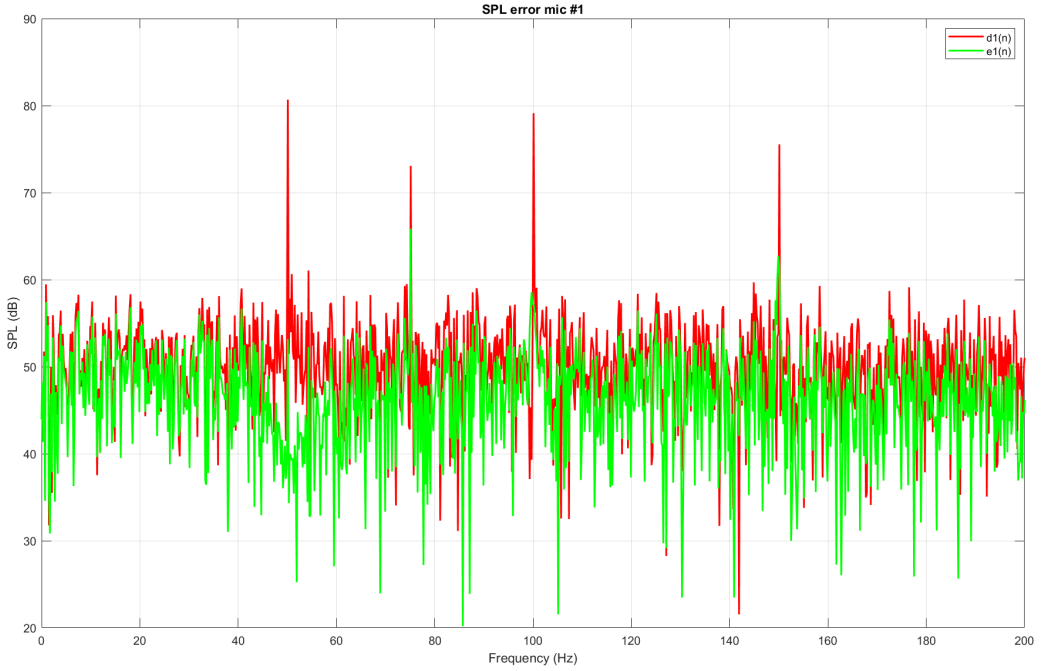

Figure 2.19: Disturbance and error signal at error microphone # 1, frequency domain

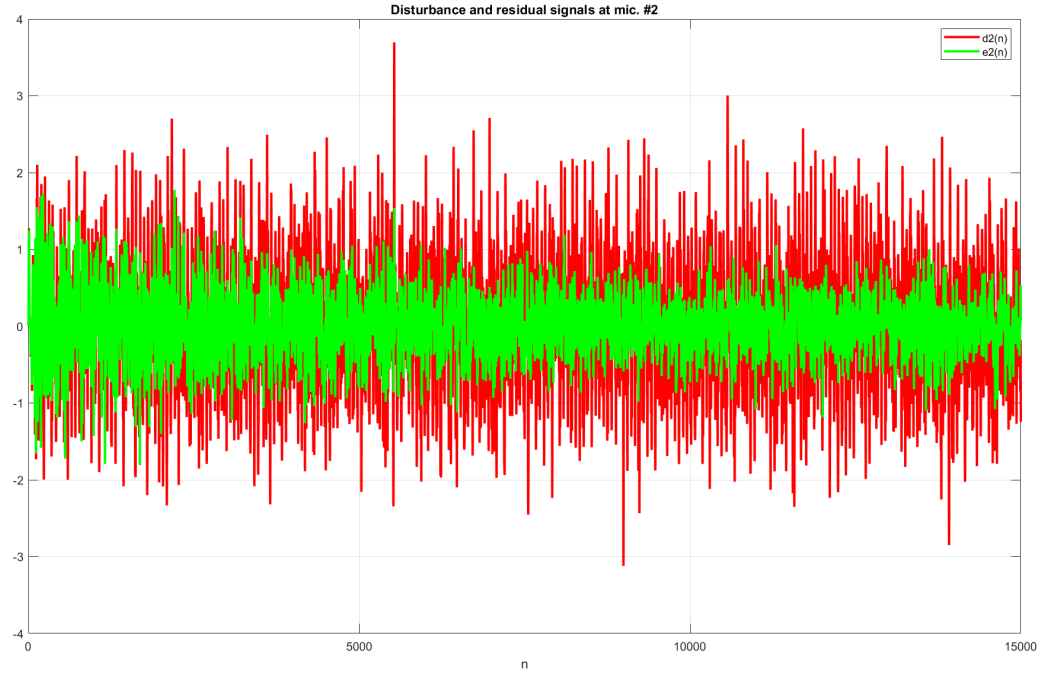

Figure 2.20: Disturbance and error signal at error microphone # 2, time domain

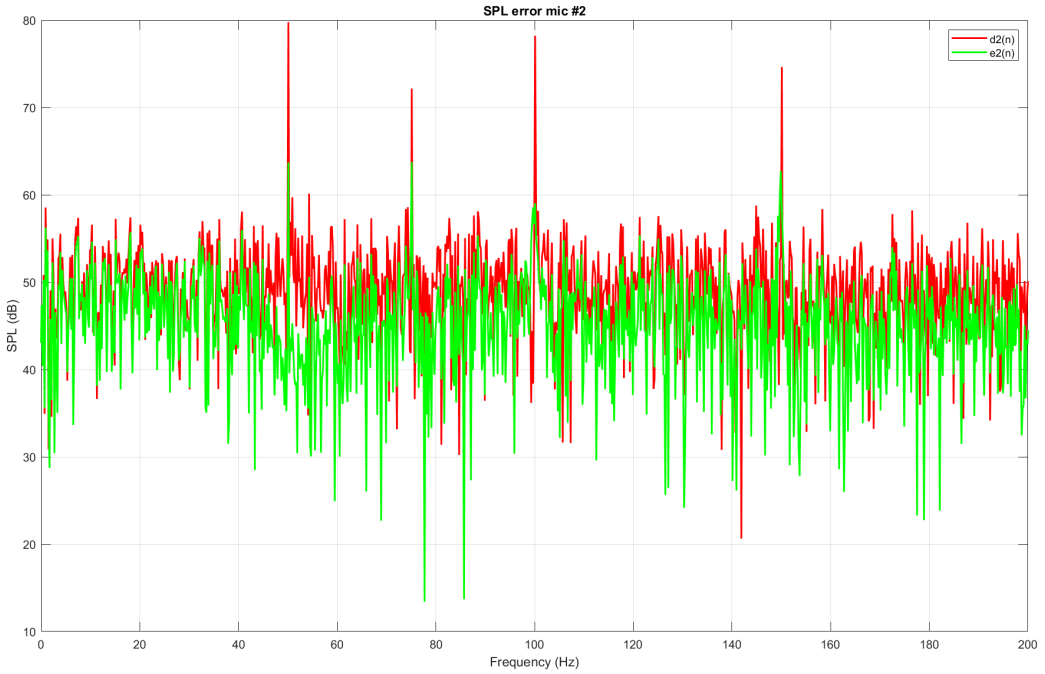

Figure 2.21: Disturbance and error signal at error microphone # 2, frequency domain

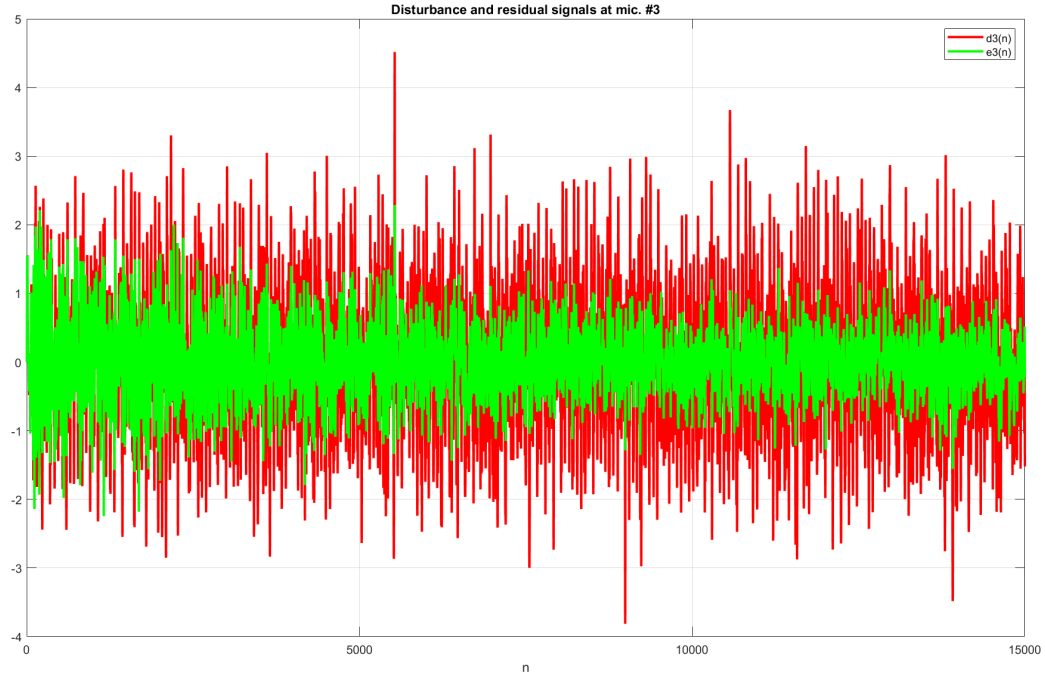

Figure 2.22: Disturbance and error signal at error microphone # 3, time domain

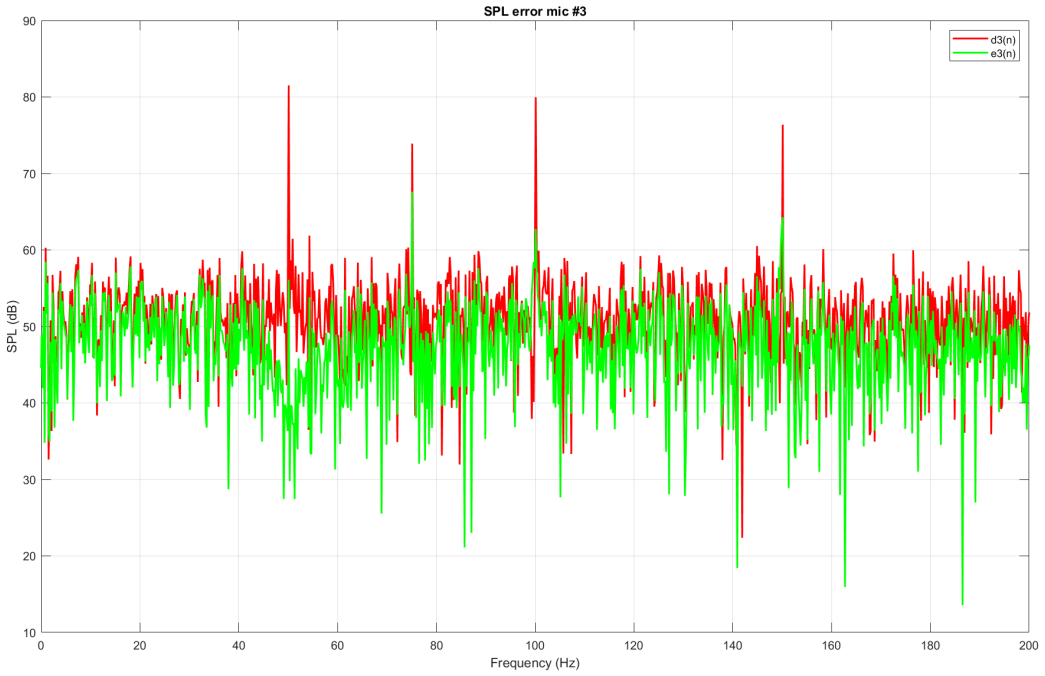

Figure 2.23: Disturbance and error signal at error microphone # 3, frequency domain

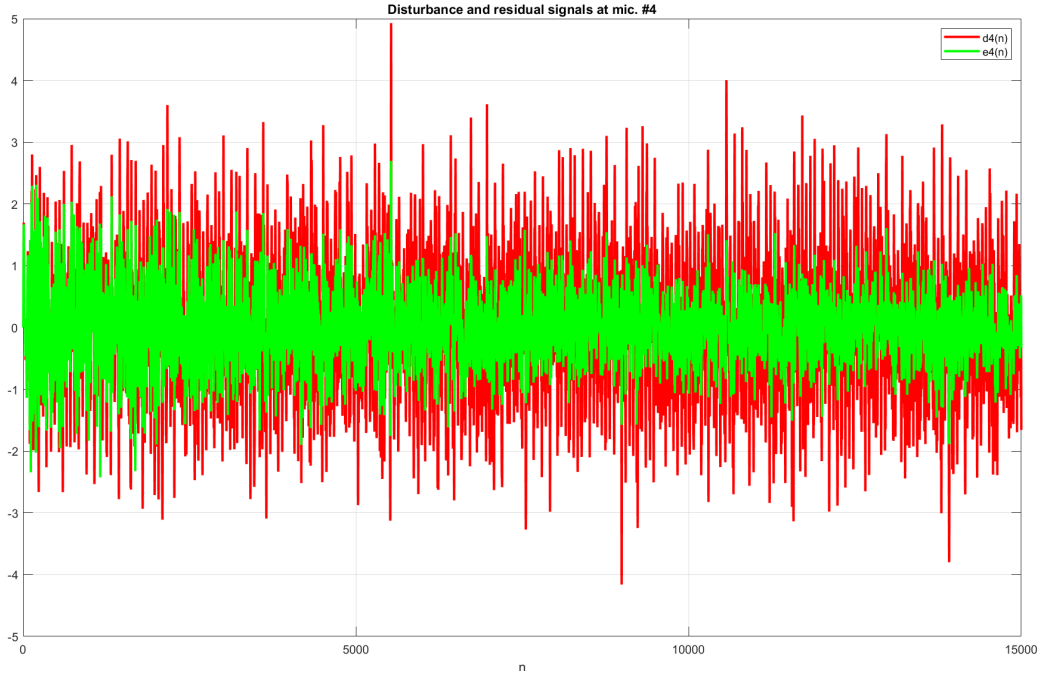

Figure 2.24: Disturbance and error signal at error microphone # 4, time domain

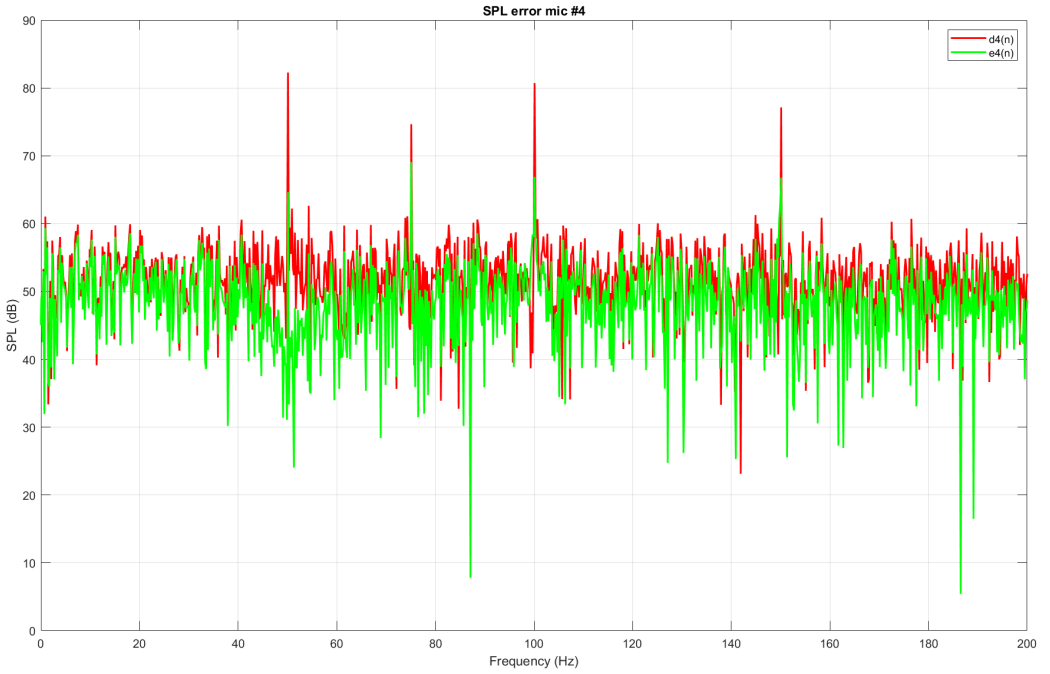

Figure 2.25: Disturbance and error signal at error microphone # 4, frequency domain

These plots show a good attenuation can be achieved both in terms of broadband noise and peak tones. Fig. 2.26 shows the SPL at error microphone # 1 when the narrowband signals are removed, while in 2.27 the same result is presented but with the reference microphone disabled instead.
Comparing plots 2.26 and 2.27 with figure 2.19, the proposed control solution can then provide both broadband noise attenuation and tones cancelling. However, the analysis was performed assuming a perfect knowledge of the frequency, which is an ideal case indeed. In realistic applications, frequency mismatches can arise when non-acoustical sensors (i.e. tachometers) provide a wrong estimate of the reference noise frequency content. This drastically reduces the performances of narrowband noise cancelling techniques. Introducing an error on the fundamental frequency estimate f_0 equal to 10% of the original value, the SPL evaluated at cancelling microphone 1 without the broadband reference signal is represented in figure 2.28. The same result without the narrowband noise attenuation system is plotted in figure 2.29. Finally, in figure 2.30 both the narrowband and the broadband system are enabled.

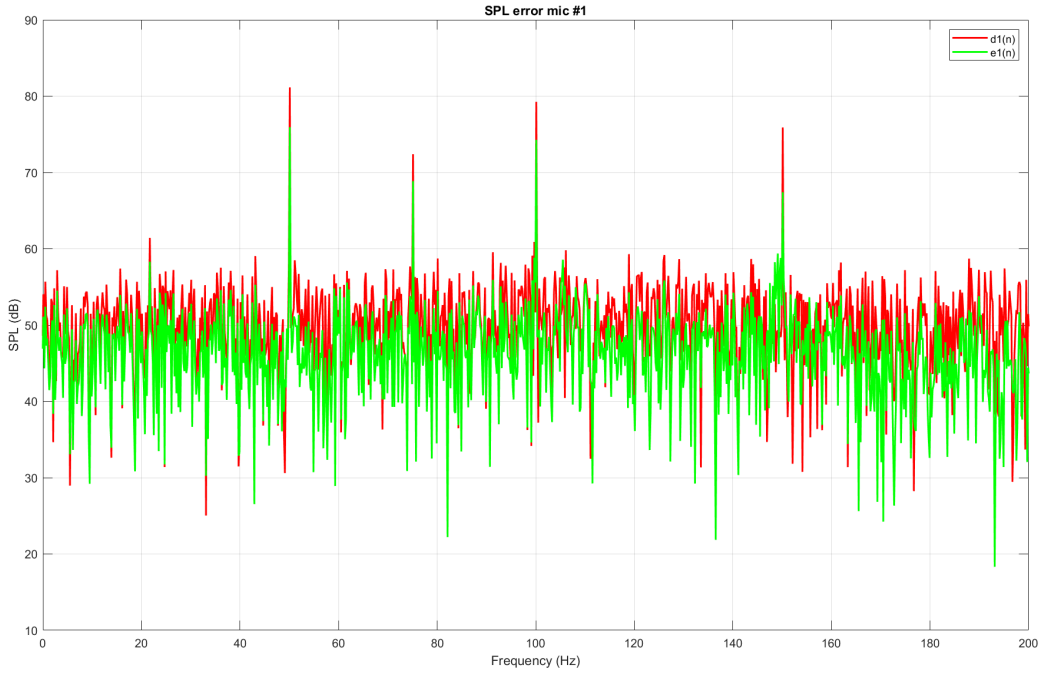

Figure 2.26: SPL err. mic. #1 , no narrowband system

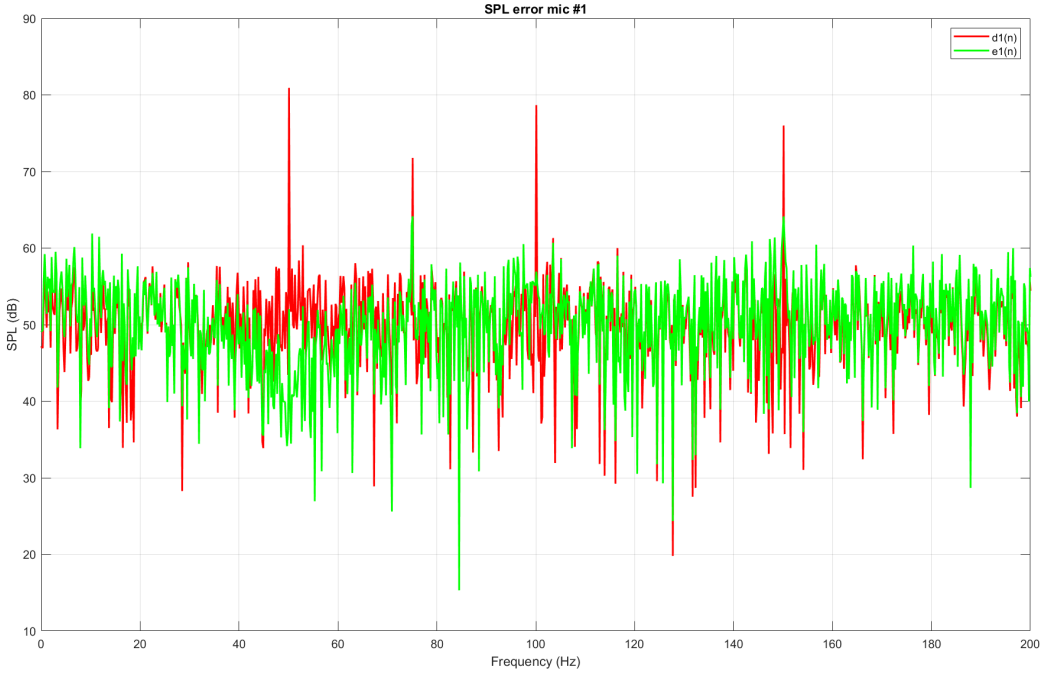

Figure 2.27: SPL err. mic. #1 , no broadband system

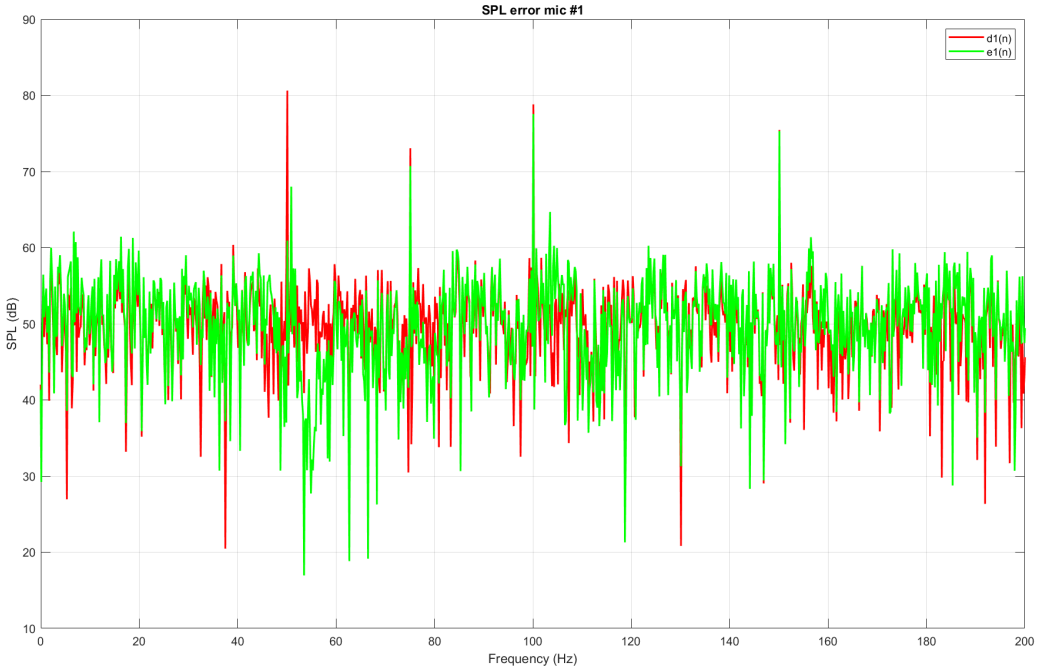

Figure 2.28: SPL err. mic. #1 , no broadband system, error in frequency estimation

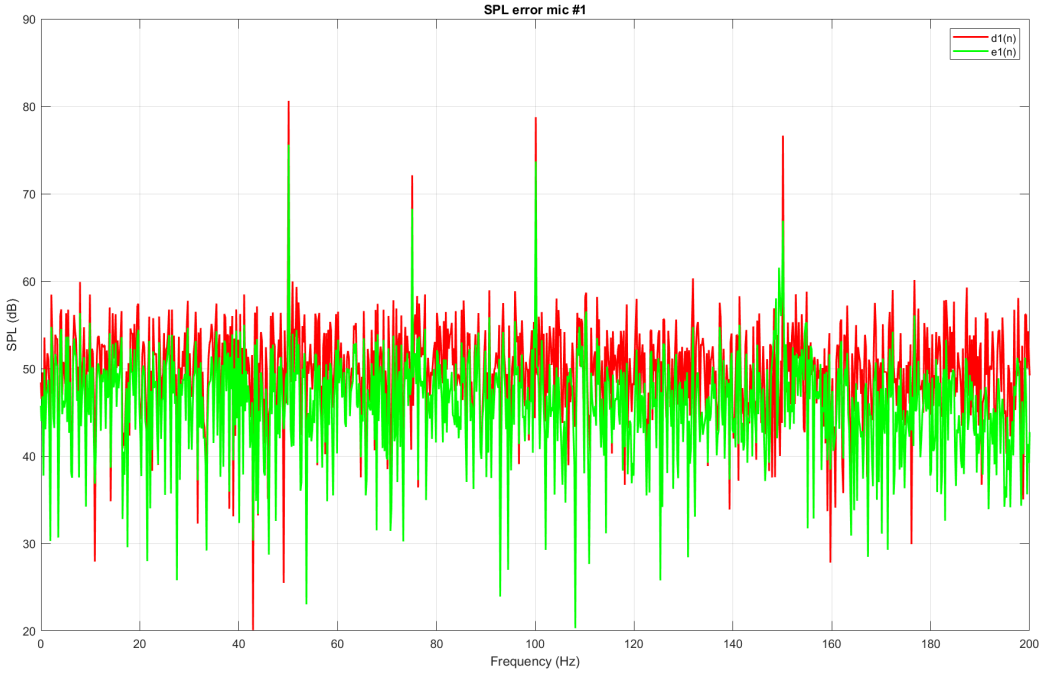

Figure 2.29: SPL err. mic. #1 , no narrowband system, error in frequency estimation

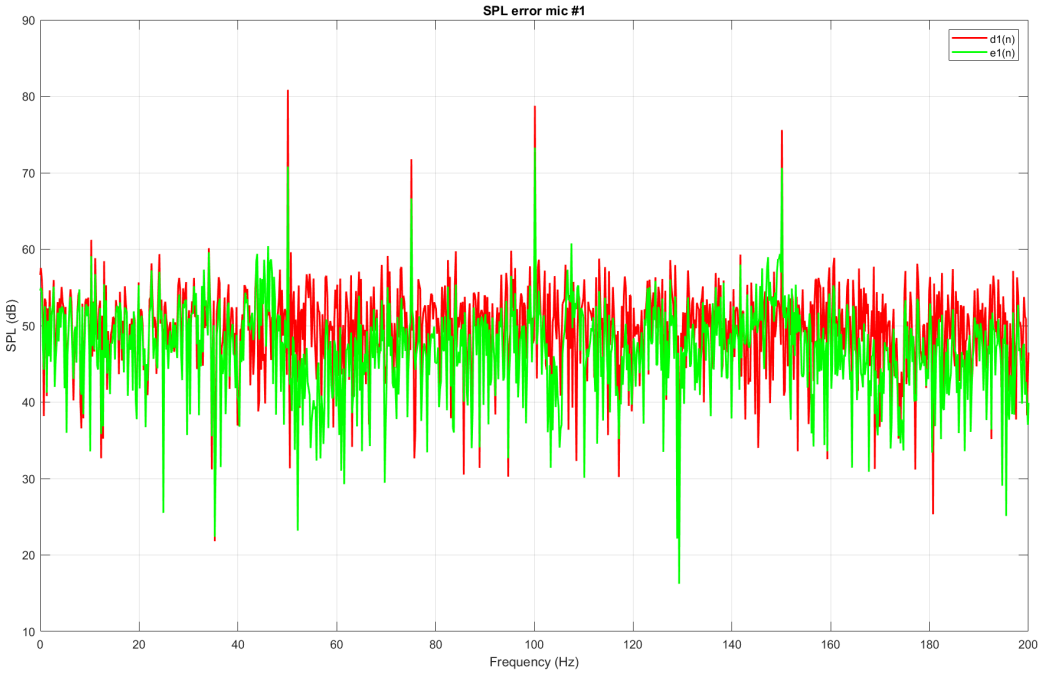

Figure 2.30: SPL err. mic. #1, error in frequency estimation

As it can be seen from figure 2.28, in presence of an error on the estimated frequency not all the peaks are attenuated. For this example the only peak still in the notch filter bandwidth even in presence of an error on the estimated frequency is the one at f_0. Figure 2.29 shows that both some broadband and narrowband attenuation can be obtained with a single reference microphone. Finally, as can be seen in fig. 2.30, in presence of a frequency mismatch the proposed control solution can provide more or less the same performances as the system without the narrowband attenuation system, as can be expected. However it is still possible to target specific frequencies if they still fall sufficiently near to the filter notches. A more effective way to reduce frequency mismatches is the introduction of a frequency estimator algorithm. This becomes of particular interest in the case of a time-varying frequency content, which is the topic discussed in subsection 2.2.4.

2.2.4 Numerical test with time-varying frequency content

Another interesting case of study is the attenuation of noise with time-varying frequency content, which in practice represents the case on an engine during

acceleration. These signals are characterized by a time-varying instantaneous frequency (IF). IF can be defined as the average frequency at each time in the signal [67]. It is expected that a narrowband attenuation system will show the best attenuation performances when the reference signals frequency content correctly follows the variation in time of the noise source one. This requires reliable tachometer measures or an instantaneous frequency estimation algorithm. A lot of effort in the signal and speech processing literature is dedicated to this topic, but IF estimation algorithms are typically complex and thus quite costly to be efficiently implemented on cheap hardware architectures for real time applications. Appendix A collects some possible solutions for this task. For this analysis, a shifting-DTF algorithm has been used due to its robustness even in presence of broadband noise. The reference signal is a linear chirp with a single tone going from $f_{in} = 20Hz$ to $f_{fin} = 100Hz$ in $5s$. Linear chirps are characterized by a linear behavior of their instantaneous frequency, as can be seen in fig. 2.31 (in green). In fig. 2.31 it is also shown the frequency obtained from the estimation algorithm. Fig. 2.32 is the plot of its spectrum: as expected, on the total time it behaves as a broadband noise with frequency content from 20 to $100Hz$.

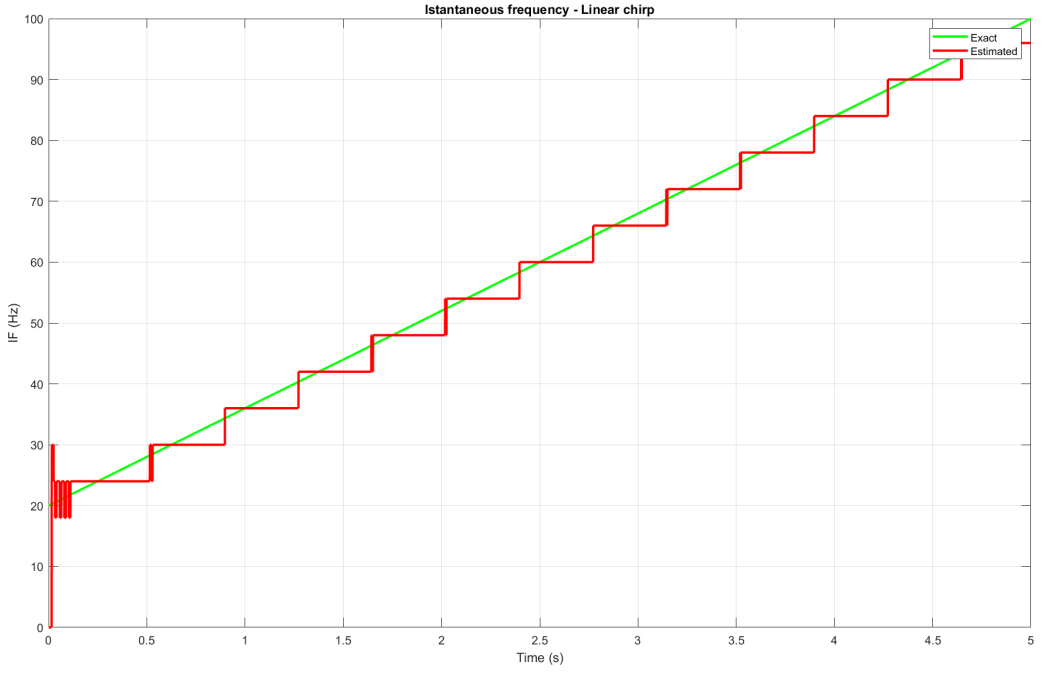

Figure 2.31: Exact and estimated linear chirp IF

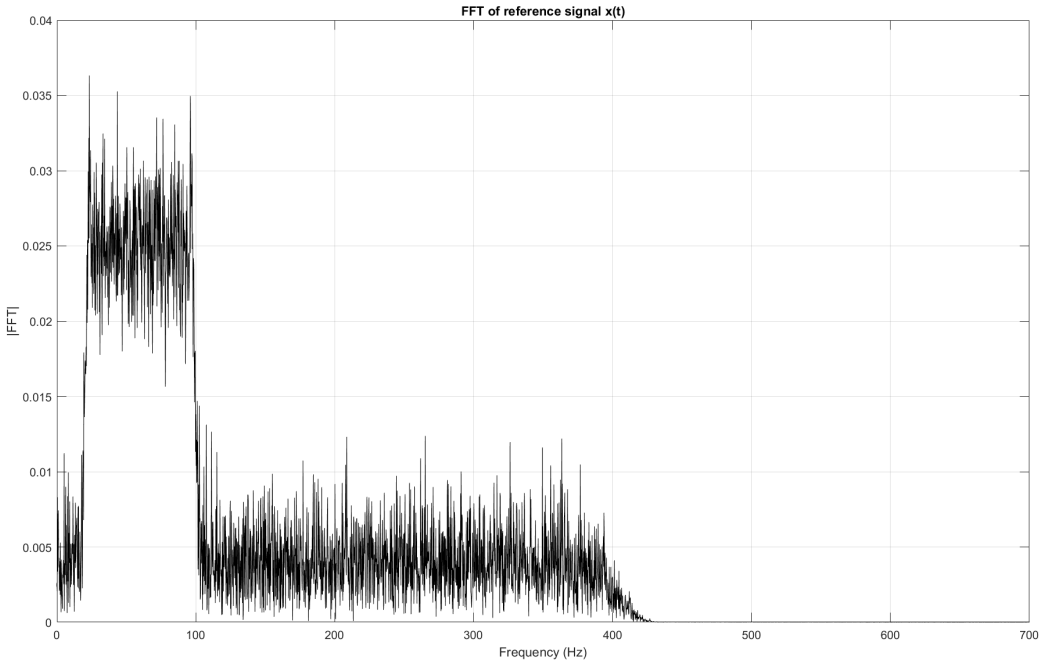

Figure 2.32: Linear chirp frequency spectrum

The analysis parameters are set as follows: $L_{contr} = 120$, $\mu_{contr} = 0.00005$, $\nu_{contr} = 0.9999$, $x_A(t) = 3\ cos(\omega_{estim}\ t)$ and $x_B(t) = 3\ sin(\omega_{estim}\ t)$. The frequency is estimated extracting the maximum FFT value evaluated on time samples vectors of length $N = 1500$. The remaining are set as in subsect. 2.2.3. The SPL at error mic. # 1 is shown in fig. 2.33. The same results is shown without the broadband reference microphone in figure 2.34. The narrowband system is disabled in fig. 2.35. Finally, both the broadband and the narrowband are enabled in fig. 2.36, but the reference frequency content is set to $\omega_{estim} = 2\pi f_{in}$ on the whole time interval.
The time-varying tone is effectively removed by the proposed control solution, under the condition that the narrowband system is fed with the correct frequency estimate and reference amplitude. The presence of a broadband microphone can provide some attenuation but the best results can be obtained only with the introduction of a narrowband attenuation system coupled with an efficient but reliable frequency estimator. As discussed in section 1.3, a practical solution to avoid the additional computational burden of an IF estimation is to adopt a non-acoustical sensor. Its correct positioning and proper functioning are then of fundamental importance to fully exploit the narrowband attenuation capabilities of the proposed solution.

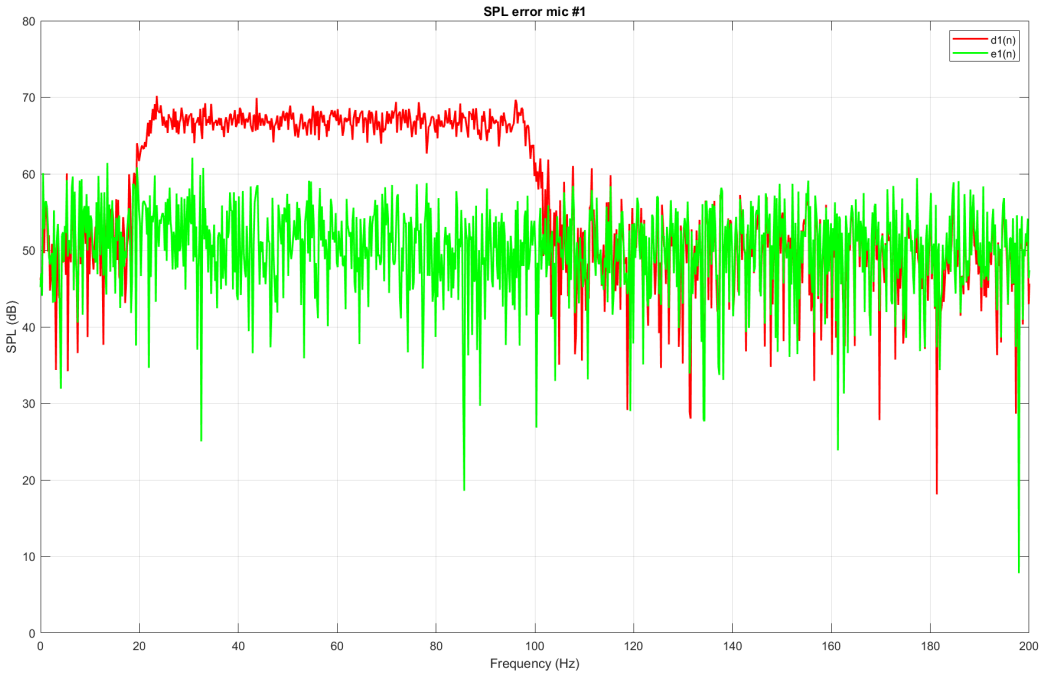

Figure 2.33: SPL at error mic. #1

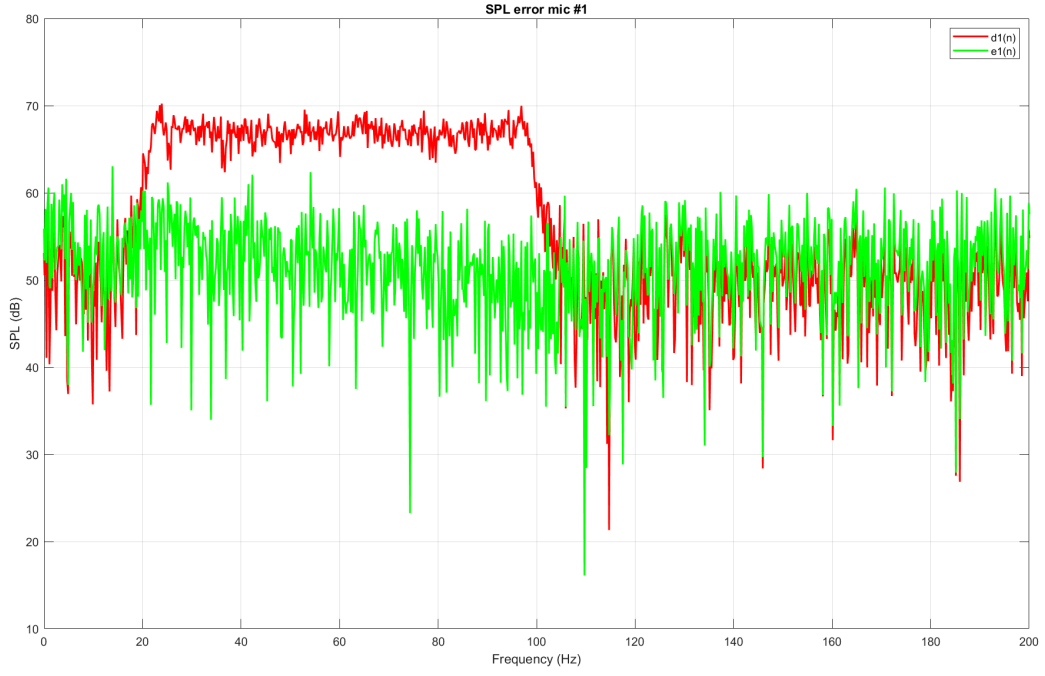

Figure 2.34: SPL at error mic. #1 - No broadband system

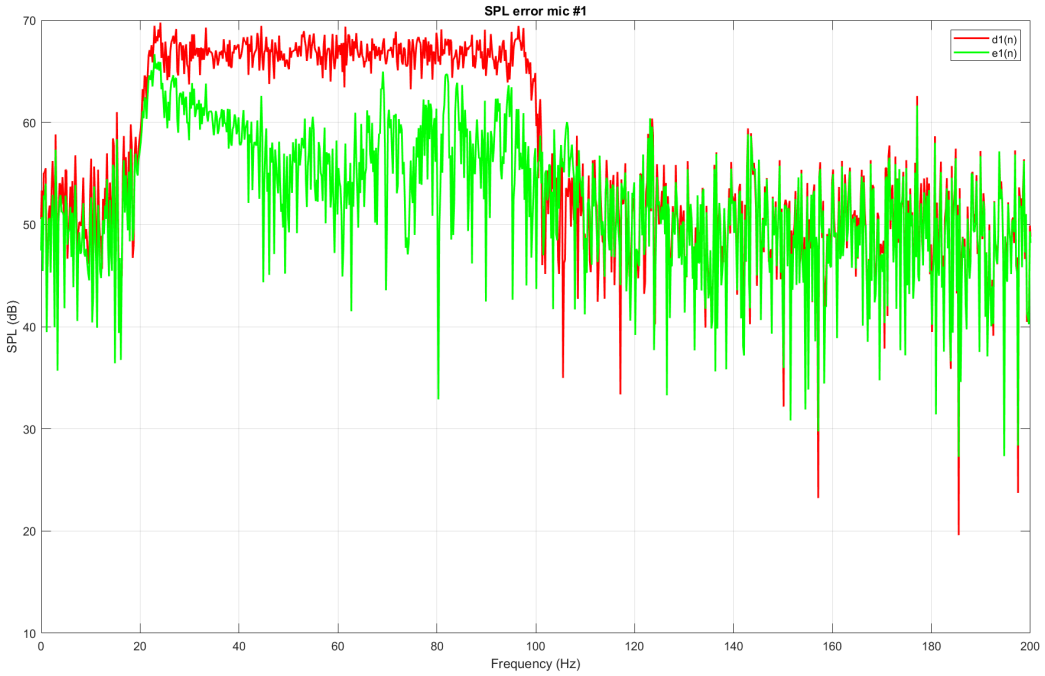

Figure 2.35: SPL at error mic. #1 - No narrowband system

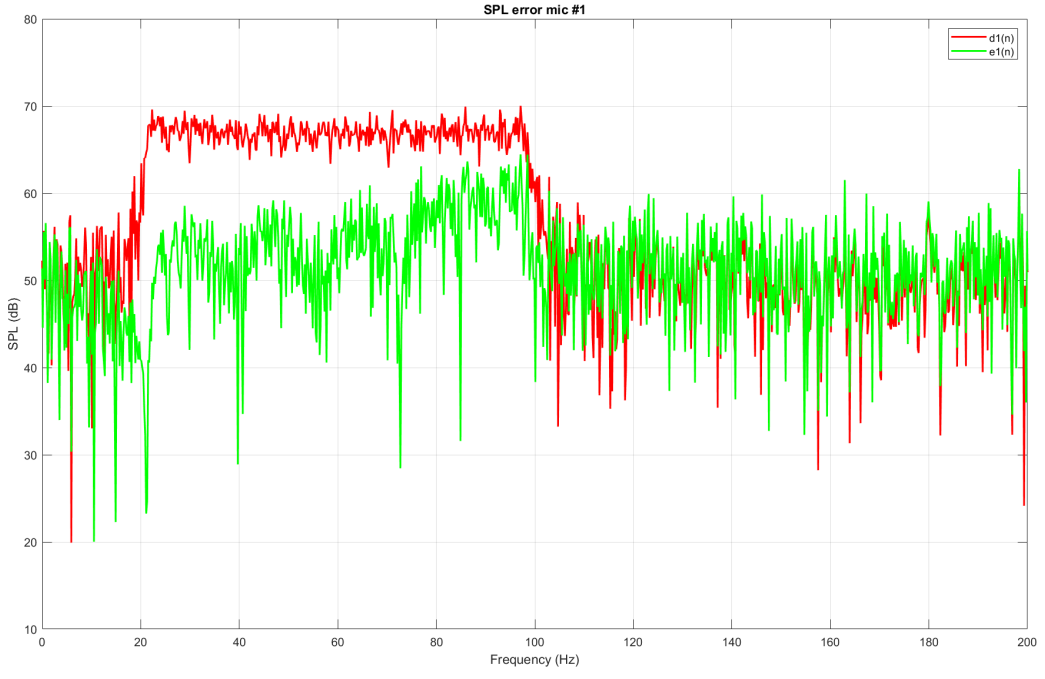

Figure 2.36: SPL at error mic. #1 - Wrong frequency estimate

In conclusion, this control solution is able to guarantee good performances in terms of tonal attenuation as long as an accurate estimate of the frequency is used to compute the narrowband reference signals. Tachometers measurement errors or time-varying frequencies associated to non-stationary operational conditions are then to be carefully treated. Real time frequency estimation techniques might be exploited to solve this problem, but it must be remembered their introduction comes with an increase in the computational cost of the algorithm, which is desired to be fast enough for real time implementation on cheap technology.
The introduction of a reference microphone guarantees some robustness with respect to frequency mismatches and broadband noise attenuation with the cost of a slight increment in the required computation by control sample as well. Moreover, in presence of an additional acoustical sensor the aforementioned problem of the acoustical feedback must be addressed, as well as the causality constraint has to be met for practical implementation, as discussed in section 1.6.

Chapter 3

ANC system simulation in small enclosures

An acoustical control simulation tool has been developed in MATLAB environment, on the base of the work described in both [23] and [24]. This simple software allows the study of the performances of ANC systems integrated in an acoustically-excited enclosure, and will be used to perform realistic preliminary studies on a noise control system in terms of convergence speed, attenuation, and quiet zone extension with respect to components positioning. The multi-channel control algorithm described in Chapter 2 has been interfaced with this acoustical simulation, as well as the secondary paths identification algorithm.

3.1 Numerical methods for virtual acoustics simulation

There are many different approaches in literature for virtual acoustical simulation of small enclosures, which are formally defined as small rooms with volumes in the range from a few cubic meters to a few hundred cubic meters [25]. From Siltanen et al. [26] and Savoja [27], the acoustical modelling of closed environments can rely on two different approaches: the geometrical approach and the wave-based approach.
Geometrical approaches (also known as ray-based approaches) are based on the geometrical acoustic assumption of a wavelength much smaller than the room dimensions.

Thus they are efficient methods but their accuracy decreases at lower frequencies. Moreover they do not consider the wave nature of sound, but they substitute sound waves with the concept of acoustic rays: each source is modeled as an emitter of particles moving along straight lines at the speed of sound between two consecutive reflections at the boundary walls. Reflections follow the reflection rule from the geometric optics (Snell's law) or can be statistically described. Particle absorption is analogously determined by the wall absorbance or an absorbance probability. The most known geometrical methods are Ray-Tracing (RT) and Image Source (IS). IS method is based on the substitution of the boundary walls reflecting the sound with emitting sources. More precisely, reflected paths associated to an emitting source are replaced by direct paths from reflected mirror images of the considered source. The image-source method is able to find all the reflected paths, but the computational requirements are such that in practice only a set of early reflections can actually be computed. As a consequence, the maximum achievable order of reflections depends on the room geometry and available calculation capacity. In addition, the geometry must be formed of planar surfaces. The RT is based on a Monte Carlo simulation technique to sample the reflection paths thus giving a statistical result. This allows a reduction of the computational cost, but it won't guarantee to find all the reflected paths.
A wave-based approach aims to solve the actual wave equation numerically. It is a "brute force" approach, so it is very accurate but typically computationally intensive, since the load grows rapidly with the frequency of interest. Thus, wave-based approaches find their application for auralization purposes only in small enclosures at low frequency ranges [27], which are of interest for active control of propeller noise in an aeronautical environment. They generally consist in the division of the space and/or its bounding surfaces into small elements. The most known methods are element methods (EM) and finite difference time domain method (FDTD). Well-known element-based methods are FEM and BEM. A FEM approach is based on the discretization of the whole acoustic space, while a BEM approach involves the discretization of the boundaries only, as discussed in subsection 1.1.4. FEM methods can thus deal with internal acoustical problems while BEM methods are used to solve acoustic radiation problems (examples of its application are the radiated pressure evaluation from a baffled piston or from a finite vibrating plate).

These methods compute a numerical approximation of the Helmoltz equation over the domain of interest. The outputs are then time-independent solutions, thus implying a separate computation for the acoustic pressure time evolution required for control applications. FDTD is instead an approach based on the direct solution of a set of algebraic equations, which are derived from differential equations (in this case the wave equation) by substituting the derivatives in time and space with their corresponding finite differences. This is the method that will be used in this activity due to its simple implementation, its accuracy even at lower frequencies and as a result of the fact that both time and space behaviors are solved simultaneously, allowing to impose arbitrary unknown control behavior in time without exploiting the Fourier transform. A third method is seldom used for virtual acoustics, which is called statistical modelling. It consists in the study of the noise level transmitted between two systems by means of a statistical energy analysis. This method does not provide the temporal behavior of the acoustical pressure and for this reason it is not adequate for noise control applications. An overview of the previously described methods is presented in figure 3.1.

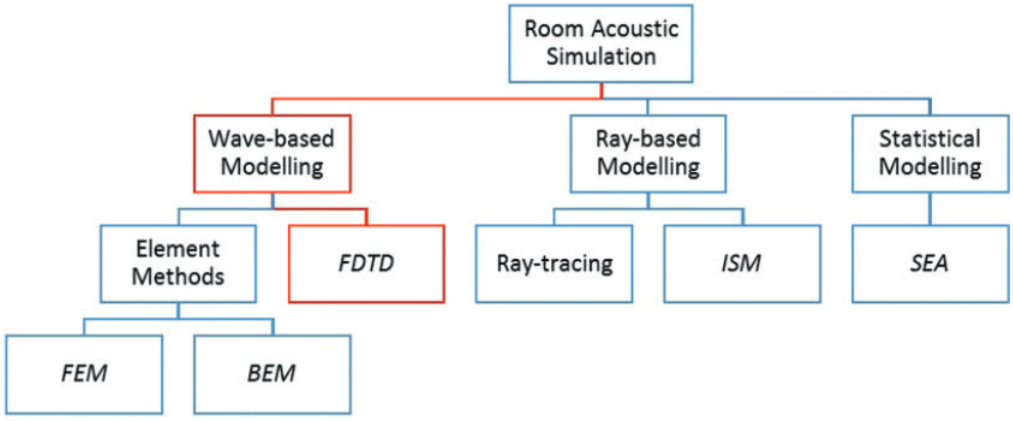

Figure 3.1: Numerical methods for virtual acoustics (from [24])

3.2 The proposed method

A MATLAB code for acoustical pressure integration during time in 3D rectangular enclosures has been developed. The simulation is based on a Finite Difference Time Domain method (FDTD). One or more forcing pressure or

volume velocity source(s) in time can be imposed in desired station(s). The boundary conditions are six walls described in terms of their apparent absorption coefficient (it accounts the amount of incident sound intensity that is not reflected). The aim is to provide a simple yet flexible and accurate tool for performance evaluation of ANC systems in small environments where the acoustics is largely affected by the waves reflections and subsequent enclosure modes contribution, which leads to the creation of standing waves that may affect the acoustic field and thus the control performances. A brief description of the method is presented. Then, a series of validation analysis are performed in order to check for the acoustical simulation reliability.

3.2.1 The FDTD method in acoustics

The FDTD method is widely used in the field of computational electromagnetism (see for instance [28]). Nevertheless, the very same numerical scheme can be applied to the acoustical framework, in which the velocity vector field and the acoustical pressure scalar field are the problem unknowns. The governing equations to be discretized are eqs. 1.1 and 1.2. In a classical leap-frog FDTD scheme, the media is divided into points separated by a spatial step h, and the derivatives evaluated for each point in time and space are replaced by their corresponding finite differences evaluated exploiting only the adjacent mesh nodes. A representation of the mesh basic cell (also known as Yee's cell, from the mathematician who formulated the FDTD method) is given in figure 3.2.

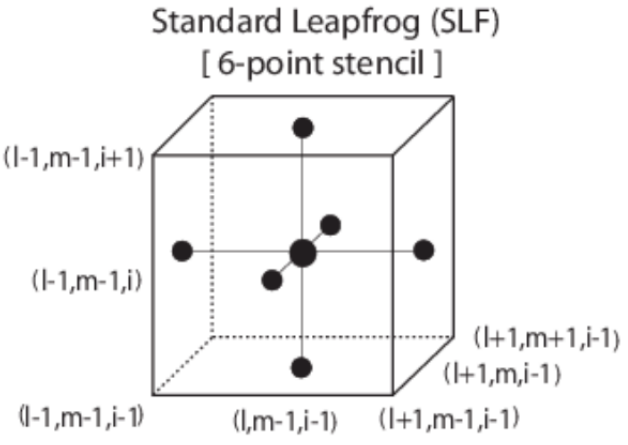

Figure 3.2: Yee's cell, from [29]

In order to enhance the computational efficiency, the numerical scheme for this activity has been made as simple and quick as possible by implementing forward finite differences only. From the momentum equation 1.1 it is then possible to obtain three updating equations for the velocity vector components:

$$u_x(x,y,z,t+\delta t) = u_x(x,y,z,t) - \frac{\delta t}{\rho_0 h}\Big[p(x+h,y,z,t) - p(x,y,z,t)\Big] \quad (3.1)$$

$$u_y(x,y,z,t+\delta t) = u_y(x,y,z,t) - \frac{\delta t}{\rho_0 h}\Big[p(x,y+h,z,t) - p(x,y,z,t)\Big] \quad (3.2)$$

$$u_z(x,y,z,t+\delta t) = u_z(x,y,z,t) - \frac{\delta t}{\rho_0 h}\Big[p(x,y,z+h,t) - p(x,y,z,t)\Big] \quad (3.3)$$

Where δt represents the time step of the analysis. From the continuity equation 1.2 the acoustical pressure at a new time step can be found as:

$$p(x,y,z,t+\delta t) = p(x,y,z,t) - \frac{c^2\rho_0\ \delta t}{h}\Big[u_x(x+h,y,z,t+\delta t) - u_x(x,y,z,t+\delta t)$$

$$+u_y(x,y+h,z,t+\delta t) - u_y(x,y,z,t+\delta t) + u_z(x,y,z+h,t+\delta t) - u_z(x,y,z,t+\delta t)\Big] \quad (3.4)$$

The spatial step size h has to be chosen carefully to avoid aliasing: the mesh discretization must be small enough to guarantee representation of the highest frequency of interest f_{max}. Kunz [30] stated that the optimum number of cells per wavelength required to provide reasonable results is from 5 to 10.

Since this is an explicit time scheme, numerical stability will be guaranteed by setting a time step consistent with the Courant-Friedrichs-Lewy condition (CFL). This implies that in a 3D problem [30] :

$$c\delta t \leq \frac{1}{\sqrt{\frac{1}{dx^2} + \frac{1}{dy^2} + \frac{1}{dz^2}}} \quad (3.5)$$

Where dx, dy and dz are the spatial steps in x,y and z direction respectively. For the considered simulation, $dx = dy = dz = h$, so the relation between the time step and the spatial step is reduced to $\frac{\sqrt{3}c\delta t}{h} \leq 1$. δt will always be set as the larger between all the admissible ones in order to reduce the computational time.

3.2.2 The sources

The acoustical forcing sources are defined as points belonging to the FDTD mesh in which the pressure time history is imposed (hard sources) or in which the current pressure value is superimposed to an externally-imposed pressure (soft source). Hard sources are completely reflective with respect to the pressure waves impacting over them. Their formulation in the numerical scheme is simply:

$$p(x_s, y_s, z_s, t) = p_s(t) \tag{3.6}$$

Where (x_s, y_s, z_s) is the source position and p_s is the hard source pressure time behaviour. Soft sources formulation directly comes from the inhomogeneous version of the continuity equation 1.2:

$$\frac{\partial \rho(\boldsymbol{x}, t)}{\partial t} + \rho_0 \nabla \cdot \boldsymbol{u}(\boldsymbol{x}, t) = q(\boldsymbol{x}, t) \tag{3.7}$$

Following [31] it is possible to derive the numerical formulation of a soft source in a FDTD scheme:

$$p(x_s, y_s, z_s, t+\delta t) = p(x_s, y_s, z_s, t) - \frac{c^2 \rho_0 \delta t}{h} \Big[u_x(x_s + h, y_s, z_s, t+\delta t)$$

$$- u_x(x_s, y_s, z_s, t+\delta t) + u_y(x_s, y_s + h, z_s, t+\delta t) - u_y(x_s, y_s, z_s, t+\delta t)$$

$$+ u_z(x_s, y_s, z_s + h, t+\delta t) - u_z(x_s, y_s, z_s, t+\delta t) \Big] + \frac{\delta t c^2 \rho_0}{h^3} q(t+\delta t) \tag{3.8}$$

where $q(t)$ is the volume velocity of the source in $\frac{m^3}{s}$. It is then clear from the previous equation that a soft source is a pressure that is added to the one evaluated in a point of the mesh. More details on the sources implementation in a FDTD scheme has been provided by Murphy [32].

The validation phase (see section 3.3) has shown reasonable results by implementing hard sources rather than soft sources, which is the reason why they will be used for the rest of the activity. Moreover, for control purposes it is desired to have a specific control pressure at the loudspeakers stations, which is exactly what can be modeled by an hard source. This approach has also been implemented in an FDTD scheme by Orlis et al. [33].
The considered acoustical sources implementation is analogous to consider them as boxed loudspeakers with dimensions $h \times h \times h$. Moreover, real loudspeakers behave approximately as acoustic monopoles at frequencies whose wavelength is much longer then the component dimension itself, emitting omni-directional spherical waves in the surrounding space (Borwick, [34]). This model is then built on the hypothesis of small loudspeakers emitting low frequency pressure waves.

3.2.3 Boundary conditions

In a wave-based method, the most difficult part is the definition of the boundary conditions [27]. The current literature deals with different approaches in order to provide consistent and realistic formulations. Boundaries consist in six walls with a given surface impedance Z. Provided that the enclosure dimensions are $L_x \times L_y \times L_z$, the acoustical pressures at the boundaries $x = 0$ and $x = L_x$ can be written exploiting the surface impedance definition:

$$p(0, y, z, t) = Z_0 \; u_x(0, y, z, t) \tag{3.9}$$

$$p(L_x, y, z, t) = Z_{Lx} \; u_x(L_x, y, z, t) \tag{3.10}$$

These expressions can be substituted in the update equation for the velocity components leading to [23]:

$$u_x(0, y, z, t + \delta t) = C_{Z1,0} \; u_x(0, y, z, t) - C_{Z2,0} \; p(h, y, z, t) \tag{3.11}$$

$$u_x(L_x, y, z, t + \delta t) = C_{Z1,L} u_x(L_x, y, z, t) + C_{Z2,L} \; p(L_x - h, y, z, t) \tag{3.12}$$

with $C_{Z1} = \frac{\frac{\rho_0 h}{\delta t} - Z}{\frac{\rho_0 h}{\delta t} + Z}$ and $C_{Z2} = \frac{2}{\frac{\rho_0 h}{\delta t} + Z}$.
Analogous expressions can be found for u_y and u_z. The surface impedance has different values for each wall and is assumed to only have a real part.

Typically complex impedances are required, but it is hard to find that data from existing literature. Moreover, a key factor to take into account in the formulation is the fact that the surface impedance is strongly dependent by the impacting sound frequency, namely $Z = Z(f)$. Jeong [35] presented two simple approaches (2-DOF approximation and minimum phase approximation) in order to directly estimate the impedance or estimate the random reflection coefficient to derive it. Under the hypothesis of normal plane waves impacting a flat surface, the surface impedance is related to the surface reflection coefficient R by the following expression [37]:

$$Z = \rho_0 c \frac{1+R}{1-R} \tag{3.13}$$

The reflection coefficient can be related to the wall absorbance coefficient α, since $\alpha = 1 - |R|^2$. Thus the wall acoustics can be described by the absorbance coefficient only. In order to formulate a simple method for its estimation the mass law has been exploited. Under the assumption of boundary limp walls (walls with only mass vibrating in the direction normal to their plane) from eq. 1.34 it is possible to obtain the transmission coefficient $\boldsymbol{\tau}$, which is defined as the ratio between the acoustical pressure transmitted through the boundary over the incident one. Its squared value is the ratio between the transmitted acoustical power and the incident one, which can be set equal to α if neither acoustical absorption nor damping are considered. From Kim [36] :

$$|\boldsymbol{\tau}|^2 = \alpha = \frac{(2\boldsymbol{Z_0})^2}{(\omega m)^2 + (2\boldsymbol{Z_0})^2} \tag{3.14}$$

where $\boldsymbol{Z_0} = \rho_0 c$, $\omega = 2\pi f$ with f the incident acoustic wave frequency, $m = \rho_w t$ with ρ_w the wall density and t the wall thickness. A correction to the previous formula has been given by Yairi et al. [38] to take into account spherical acoustic waves absorption instead of plane ones, which is a more precise model for acoustic pressure propagating in a small environment in which the reflection is likely to occur in the near-field acoustical region:

$$\alpha = \frac{arctg(\frac{m\omega}{2\boldsymbol{Z_0}})}{\frac{m\omega}{2\boldsymbol{Z_0}}} \tag{3.15}$$

3.2.4 Initial conditions

The particle velocity components at time $t = 0$ has been set to zero (rest condition) in the whole domain.

This is consistent with the hypothesis under which wave equation 1.3 is obtained. The initial acoustical pressure is set to zero as well, so the fluid pressure in the enclosure is initially equal to the atmospheric one.

3.3 Simulation validation

In Section 3.2 a numerical scheme for internal acoustic simulations based on the FDTD method has been briefly discussed. The code has been written in MATLAB environment. A series of tests is now presented in order to provide its validation prior to the control algorithm implementation by comparing the numerical results with known analytical results from closed spaces acoustics summarized in Chapter 1. Two enclosures are defined:

- A room $7.8 \times 4.12 \times 2.77m$, the same considered in [23]
- A duct $24 \times 2 \times 2m$

3.3.1 Analysis of the room

A sinusoidal hard pressure source is set in the centre of the room, at $x_s = \frac{L_x}{2}$, $y_s = \frac{L_y}{2}$, $z_s = \frac{L_z}{2}$. The excitation frequency is $54Hz$. The propagation media is air, so $\rho_0 = 1.225\ \frac{kg}{m^3}$ and $c = 343\ \frac{m}{s}$. Figure 3.6 is the top view of the plot showing the propagation of an acoustic wave in the x-y plane from the centre of the room to the wall parallel to the x axis. The observation plane is set at $\frac{L_z}{2}$. The absorbance coefficient is set to 0.99, which is representative of an highly absorbing room (anechoic room), in order to avoid boundary walls reflection during the run. The solution is symmetric as expected. Moreover the propagating wave has a circular wavefront, which results from the cut of a spherical wave by a plane parallel to the x-y plane. These results are consistent with the acoustic monopole analytical solution described in subsection 1.1.2. In addition, it can be seen the propagation time between the first shot and the third one is equal to $24.60\ ms - 18.59\ ms = 6.01\ ms$, while the wave travelled distance is equal to $\frac{L_y}{2} = 2.06\ m$. This leads to a propagation speed equal to $342.76\ \frac{m}{s}$, corresponding to an error of 0.07 % with respect to the expected one.

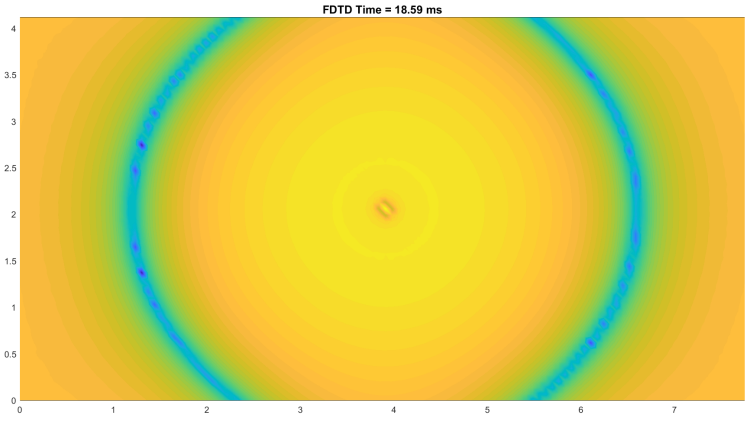

Figure 3.3: Time: 18.59 ms

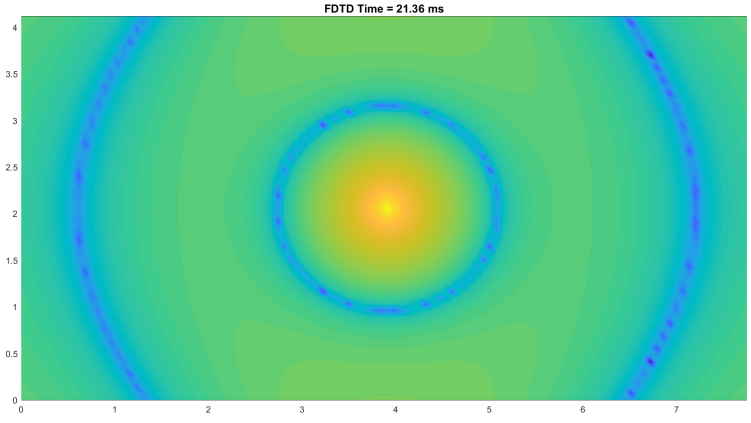

Figure 3.4: Time: 21.36 ms

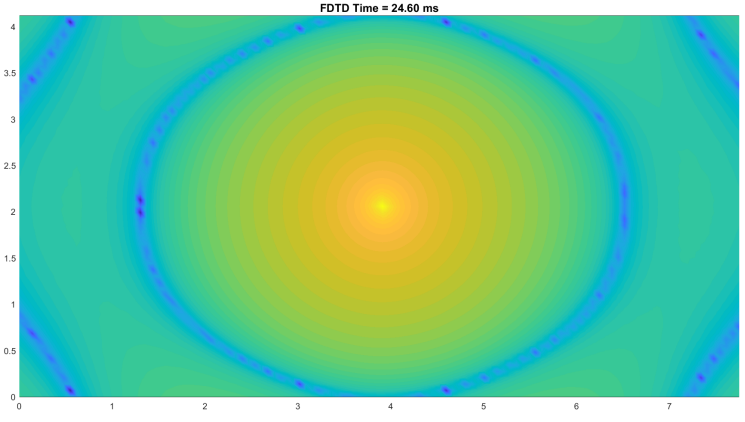

Figure 3.5: Time: 24.60 ms

Figure 3.6: Propagating waves at different time instants

From subsect. 1.1.2, in a monopole near field the attenuation of the acoustic energy (or analogously the SPL attenuation) is equal to $-6dB$ when doubling the distance from the source. In fig. 3.7 and 3.8 the obtained numerical attenuation in the central monopole near field has been recorded for a timespan of $0.3s$. The spatial step is $h = 0.0686m$ and the timestep is $\delta t = 1.155e{-}04s$, which correspond to a maximum frequency of interest $f_{max} = 500Hz$ with 10 mesh elements in its wavelength. The attenuation are evaluated as differences between the SPL recorded at two virtual microphones in the vicinity of the loudspeaker, at distances h and $2h$ in figure 3.7, whereas the distances are $3h$ and $6h$ in figure 3.8. After a quick transient, the attenuation stabilizes to a value of $-6.128dB$ in the first case and $-6.561dB$ for the second simulation, leading to a 2.13% and 9.35% error respectively.

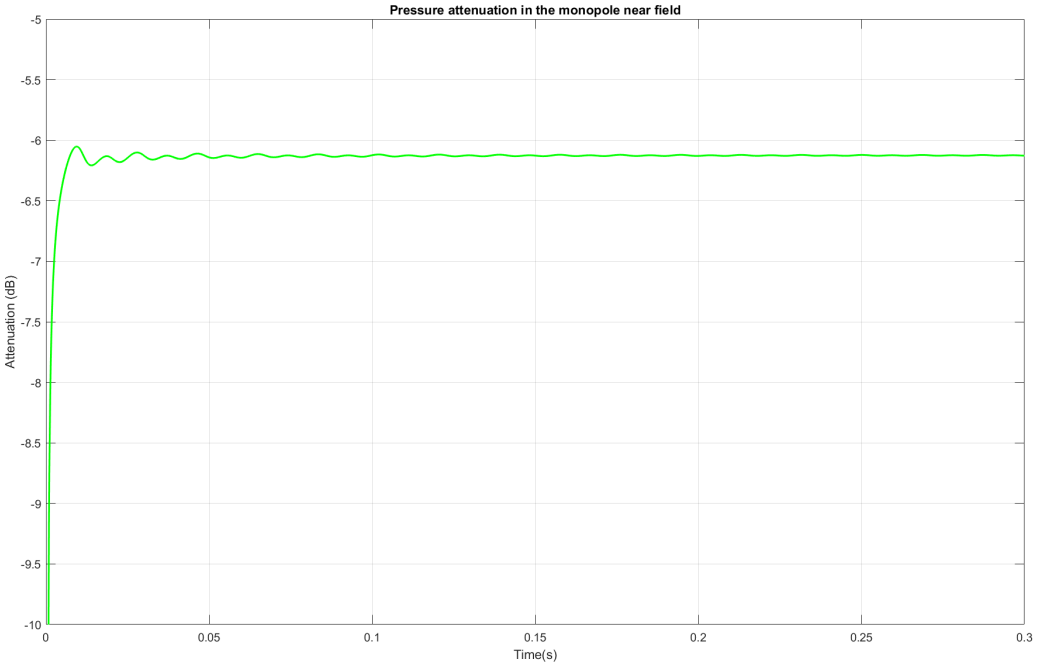

Figure 3.7: Attenuation (dB) in monopole near field

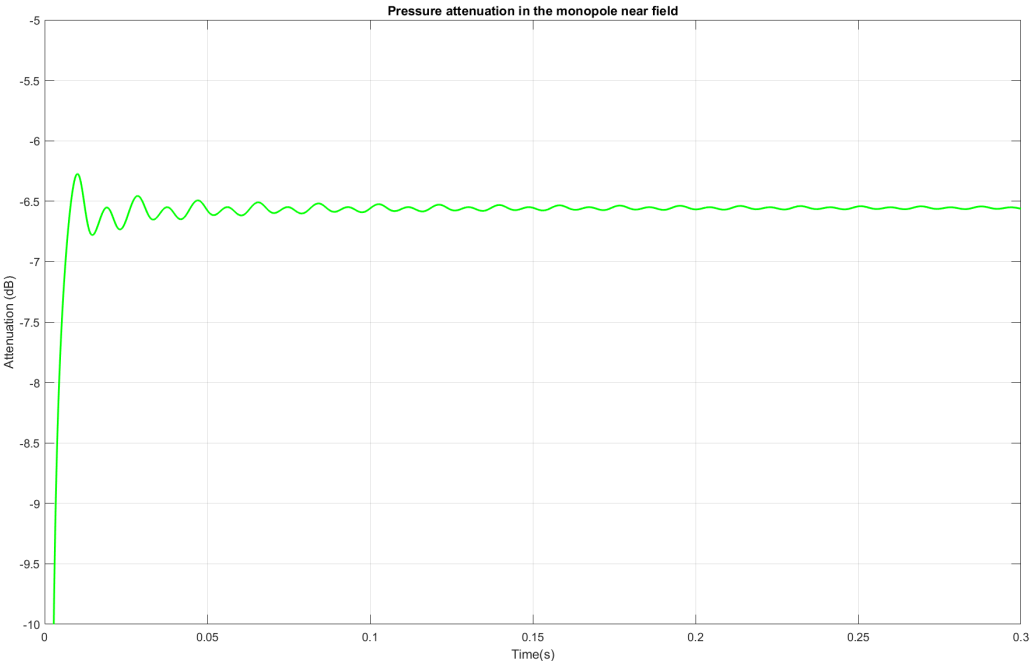

Figure 3.8: Attenuation (dB) in monopole near field

Next, the absorption coefficient is lowered. A value for α equal to 0.1 has been chosen, and reverberation effects are expected to be seen. Since the room volume is $V = 89.4m^3$ and the maximum wavelength of interest is $\lambda = \frac{c}{f_{max}} = 0.69m$ the room has a ratio $\frac{\lambda}{V^{\frac{1}{3}}}$ equal to 0.15, which is a value sufficiently small with respect to 1 to consider the room as acoustically large. For acoustically large enclosures, Sabine theory for reverberation time evaluation can be considered valid if the boundary walls have small absorption coefficients and the sound field is diffuse, as discussed in subsection 1.2.1. For what concerning the latter hypothesis, it is known that in regularly-shaped enclosures such as rectangular rooms it is more difficult to realize a reverberant diffuse sound field. For this reason a first check for the spatial variability of the acoustical pressure is performed. Figure 3.9 shows the direct and reverberant sound field along x direction after $1s$ of simulation with a central sinusoidal source at frequency $f = 54Hz$.

The plot clearly shows the presence of a direct field (the $-6dB$ attenuation region for the acoustic monopole) and a reverberant field region. The vertical line corresponds to the reverberation radius, which can be synthetically defined as the distance at which direct and reverberant fields contribute in the same manner to the acoustical pressure. A central impulsive hard pressure source is also defined: to avoid aliasing, it is set as a band- limited Gaussian pulse: fig. 3.10 shows its behavior in time while 3.11 shows its frequency content. In order to formulate significant analysis in an FDTD framework, an initial delay in the excitation is suggested [71]. The direct and reverberant field plot for an impulsively excited enclosure is also provided in fig. 3.12.

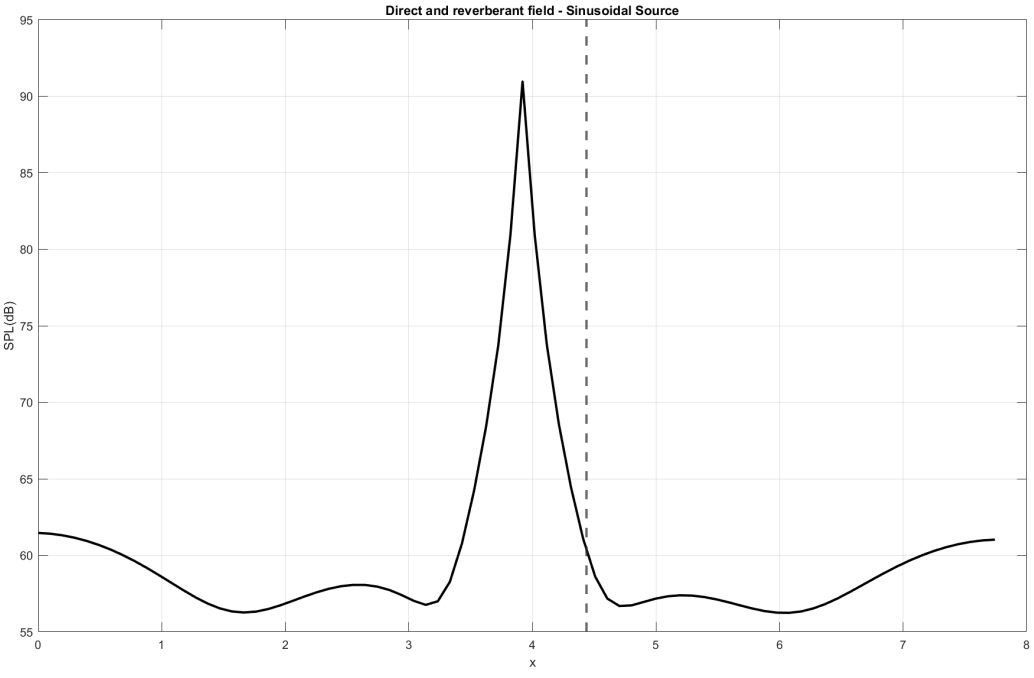

Figure 3.9: Direct and reverberant field for central sinusoidal source

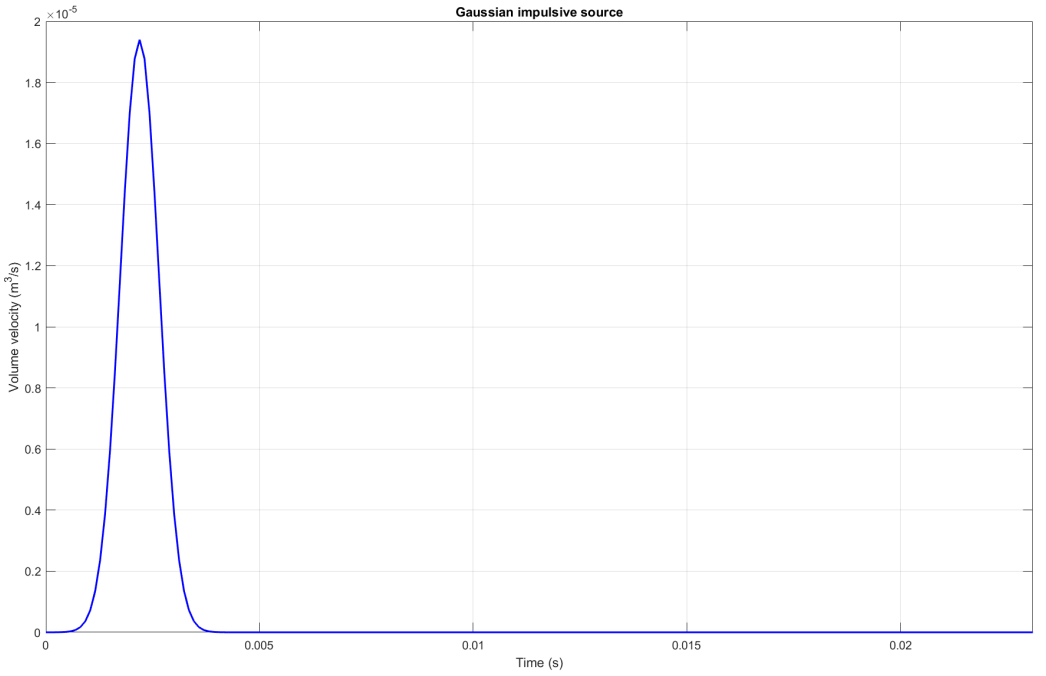

Figure 3.10: Applied Gaussian pulse in time

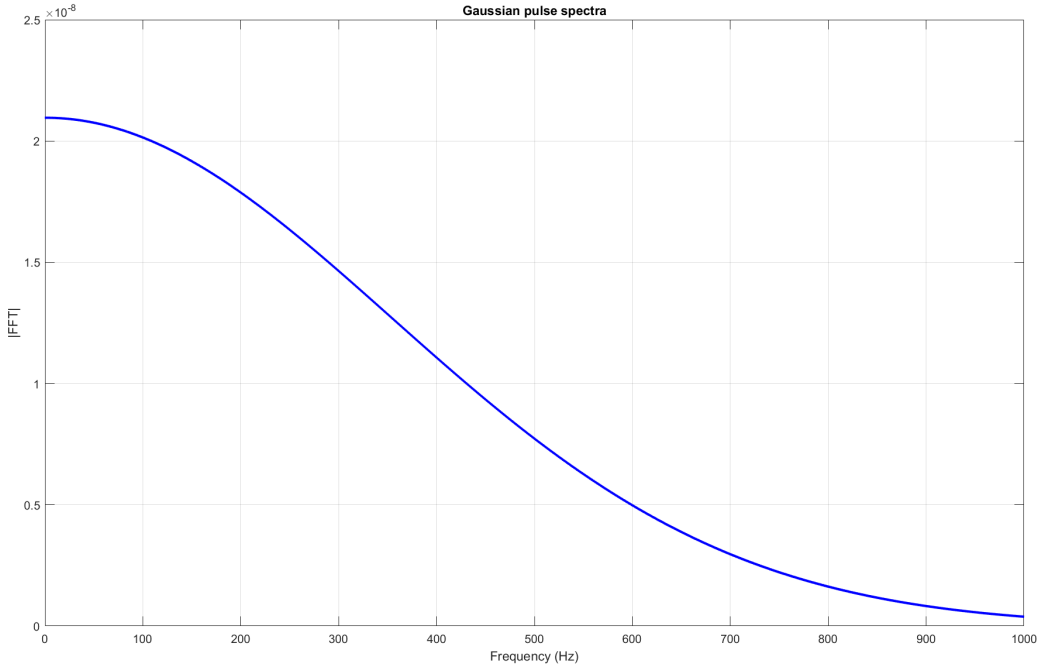

Figure 3.11: Gaussian pulse frequency content

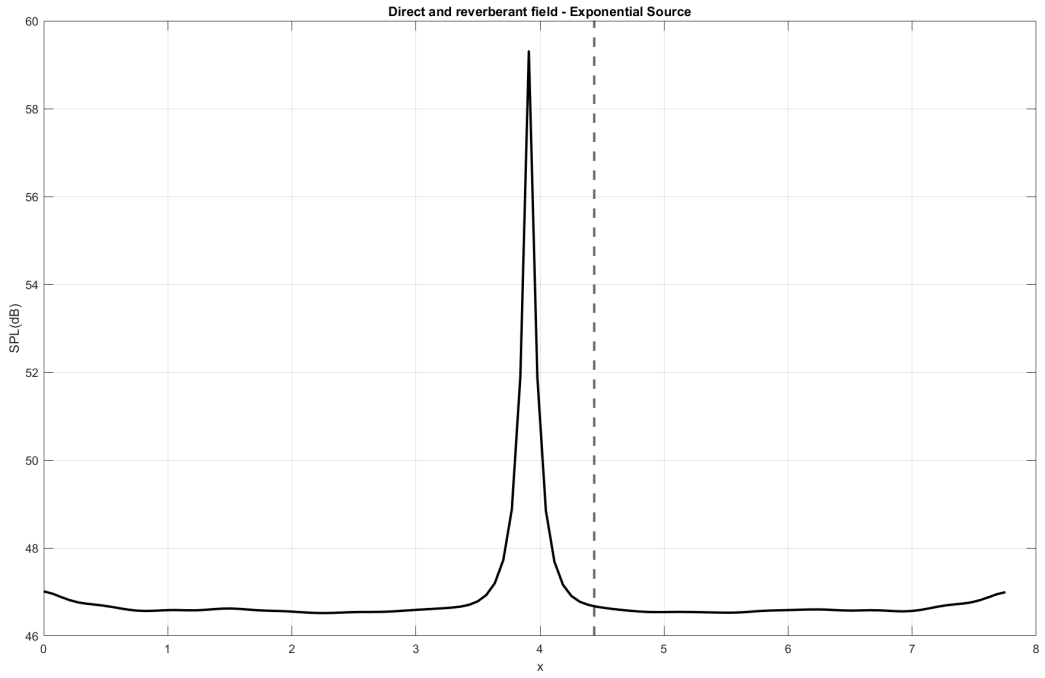

Figure 3.12: Direct and reverberant field for central impulsive source

Apart from the central zone in which the pressure averaged in time is obviously higher, the behavior in the reverberant field region is quite diffuse. For what concerning the small absorption coefficients hypothesis, even if $\alpha = 0.1$ can be considered sufficiently small in order to apply Sabine formula for the reverberation time, Norris-Eyring formula is instead used since this correction leads to more realistic results:

$$T_{rev} = 0.1611 \frac{V}{-A\ ln(1-\alpha)} \tag{3.16}$$

where A is the total internal surface of the enclosure. For the given room and α, the theoretical reverberation time is $1.0445s$. The total simulation time is set equal to this value. Fig. 3.13 shows the evolution of the acoustic energy averaged on the plane at $z = \frac{L_z}{2}$ during the run. The black line is the theoretical decay behavior from Sabine theory. According to it, the acoustic energy decay follows a negative exponential $\epsilon(t) = \epsilon_0 exp(-\frac{t}{\tau})$, where $\tau = \frac{4V}{cA_s}$ and $A_s = \sum_{n=1}^{6} S_i \alpha_i$ (Kim, [36]).

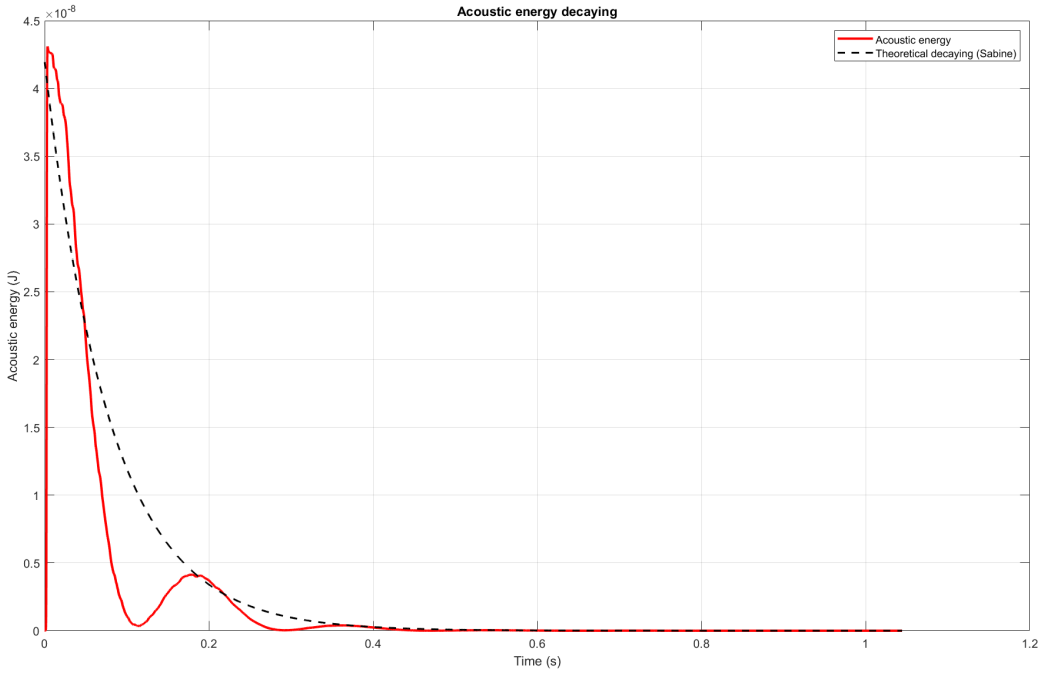

Figure 3.13: Acoustic energy decay and theoretical expected behavior in time

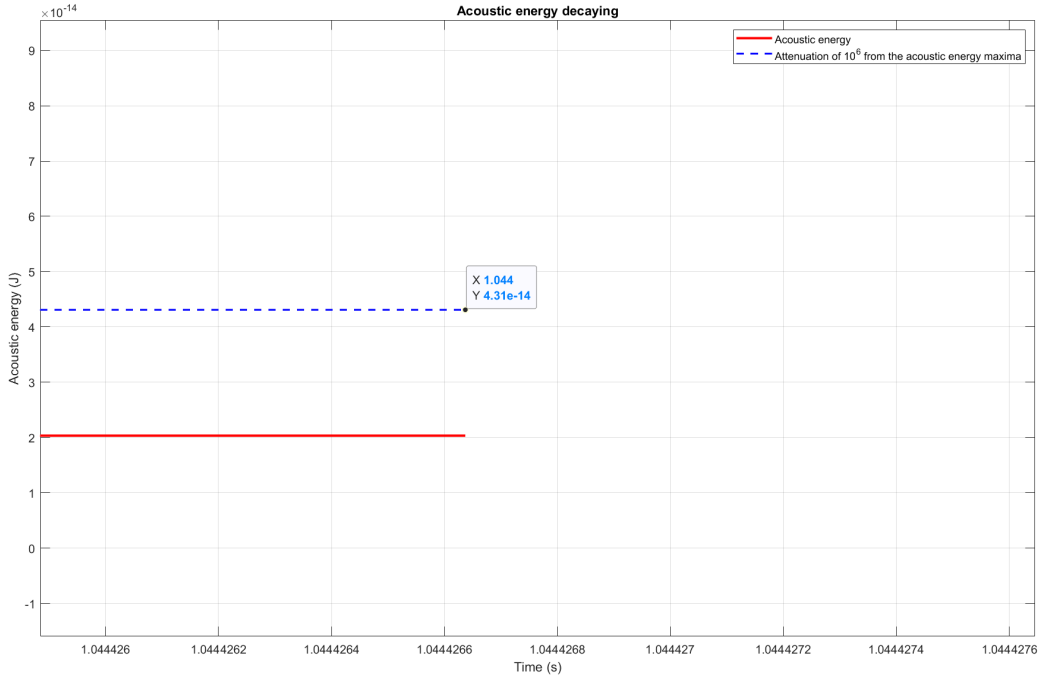

Figure 3.14: Numerical acoustic energy vs expected value at $t_{final} = T_{rev}$

Fig. 3.14 shows the acoustic energy and a blue line representing the attenuation of a factor 10^6 from its maximum value, zoomed at the final time instant which has been set equal to the reverberation time. These values should be as close as possible, since the reverberation time is defined as the time at which the acoustic energy is attenuated by a factor 10^6 from its maximum. The plot shows a relative error of 53.60 %, but on an order of magnitude equal to 10^{-14}. For this reason the error can be instead evaluated in terms of the difference between the numerical reverberation time and the expected one, which corresponds to the intersection of the blue horizontal line with the red plot. This intersection is found at $t = 0.9765s$, corresponding to a relative error on the reverberation time equal to 6.51%.

3.3.2 Modal analysis of a duct

A duct can be defined as a space whose length along one direction (x) is significantly greater than the cross sectional dimensions. This constraints the low frequency waves propagation in a single direction [36]. For an infinite rectangular duct with rigid (highly reflective) walls, an exact expression for the acoustic pressure distribution can be found starting from the Helmoltz equation. In analogy with the solution for 3D rectangular rigid walls room acoustics, it will consist in a sum of modes, as stated in subsect. 1.1.3. From [39]:

$$P(x,y,z) = \sum_{l,m,n=0}^{\infty} \boldsymbol{a_{l,m,n}} cos(k_x x) cos(k_y y) cos(k_z z) \tag{3.17}$$

Each enclosure mode is defined by a triad of integers (l, m, n) and has a natural frequency which can be evaluated as

$$f_n = \frac{c}{2}\sqrt{\left(\frac{l}{L_x}\right)^2 + \left(\frac{m}{L_y}\right)^2 + \left(\frac{n}{L_z}\right)^2} \tag{3.18}$$

An expression for the modal nodes can be derived from the previous formula by setting $P(x, y, z) = 0$. For an axial mode $(l, 0, 0)$:

$$x_{nodal,l} = (2p+1)\frac{L_x}{2l} \tag{3.19}$$

with p integer ≥ 0. This means the mode $(l, 0, 0)$ will exhibit exactly l nodes.

Numerical simulations are performed by imposing a sinusoidal hard source at $(0.1, 1, 1)m$ whose frequency is set equal to a certain modal frequency of the duct. The step sizes are $h = 0.1715m$ and $\delta t = 2.8867e-04s$, corresponding to maximum frequency of interest $f_{max} = 200Hz$ with 10 mesh elements in its wavelength. α is set to 0.000015 for each wall, in order to define a very reverberant environment. Figure 3.15 - 3.20 show the top views of the SPL in the plane $z = \frac{L_z}{2}$ after $1s$ of simulation by exciting the duct at the natural frequency of axial modes $(1, 0, 0)$,$(2, 0, 0)$ and $(3, 0, 0)$ along with the expected theoretical mode shapes.

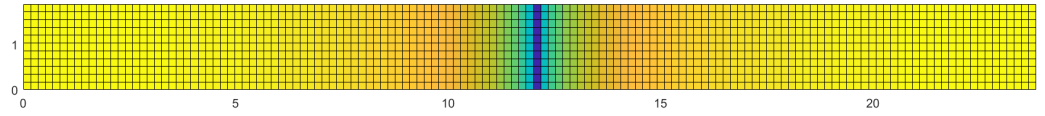

Figure 3.15: Mode 1 - Theoretical

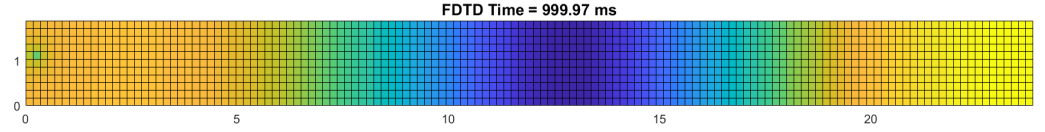

Figure 3.16: Mode 1 - Numerical

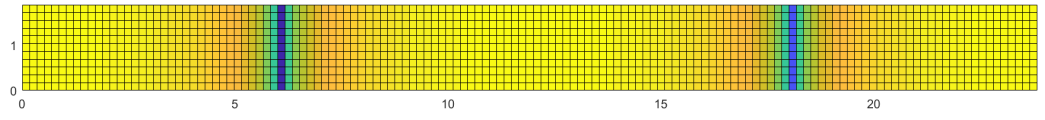

Figure 3.17: Mode 2 - Theoretical

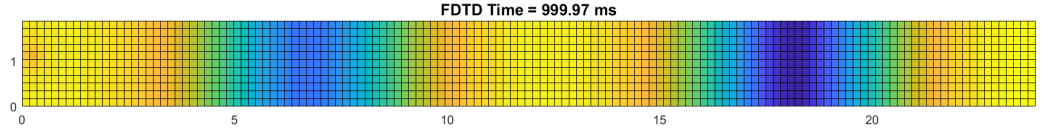

Figure 3.18: Mode 2 - Numerical

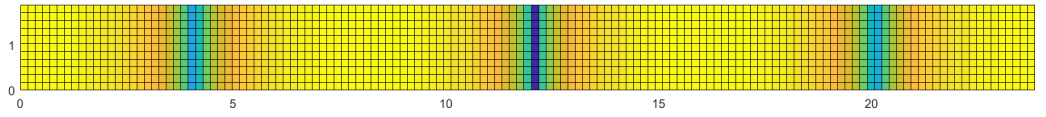

Figure 3.19: Mode 3 - Theoretical

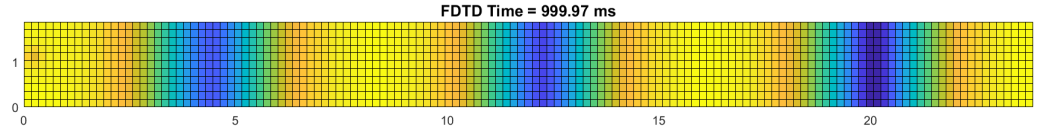

Figure 3.20: Mode 3 - Numerical

These plots show that the excitation of a rectangular rigid walled duct at its natural frequencies results in a noticeable modal response, where the single dominant mode has the expected shape.
In conclusion, the simple simulation tool written for the activity provides quite accurate results with respect to theoretical ones from classical acoustics. Celestinos [23] also provided an experimental validation of the FDTD acoustical simulation in a real closed environment. This simplicity and precision comes with the prize of a computational cost which rapidly increases for finer meshes and thus with the frequency of interest. The number of computations in a 3D grid in fact grows as the cube of the number of points in the mesh. Moreover, a linear increment is subsequent to grid refinements since the spatial and temporal steps are related by the CFL condition. All the analysis have been carried out on a domestic computer with limited hardware capabilities, therefore the interest will be focused only on small enclosures and low excitation frequencies.

3.4 The implementation of the control scheme

The control algorithm discussed in Chapter 2 is used to provide desired output pressures to a set of four control loudspeakers occupying a given position in the FDTD mesh, which act as hard pressure sources. The simulated space is a small rectangular enclosure which might approximate a pilot cockpit, in which a control system is inserted with the aim to realize a small zone of noise attenuation around the pilot's head expected position. The disturbance is generated by a couple of loudspeakers as internal sound sources.

The control algorithm requires the pressure evaluated at four error stations, two of which are set as close as possible to the pilot's ears positions. Moreover, two narrowband signals are required as reference signals along with the pressure computed at a microphone reference sensor. Prior to the control it is necessary to estimate the secondary acoustical paths and the feedback paths. These identifications are also performed numerically by following the identification process described in Chapter 1, driving the control loudspeakers with band-limited (filtered) white noise in order to avoid aliasing. The control is performed at lower sampling frequencies with respect to the simulation frequency. In particular, it is activated every n_c simulation time steps, so while the simulation frequency is $f_{sim} = \frac{1}{\delta t}$, the control frequency is $f_{cont} = \frac{1}{n_c\ \delta t}$. This limits the possible range of choices in the control frequency. The pressure imposed to the loudspeakers is kept constant between one control action and the next one. The simulation is stopped if one or more acoustical pressures at the microphones become too high due to identification or control instabilities.

Chapter 4

The performed simulation and optimization results

The noise control algorithm and simulation described in the previous chapters have been implemented in order to perform a series of numerical tests in a simplified reverberant enclosure. The aim is to provide an optimized configuration of the control loudspeakers specifically for local noise attenuation. In an ANC system optimization framework, a hierarchy does exist, as can be seen from figure 4.1:

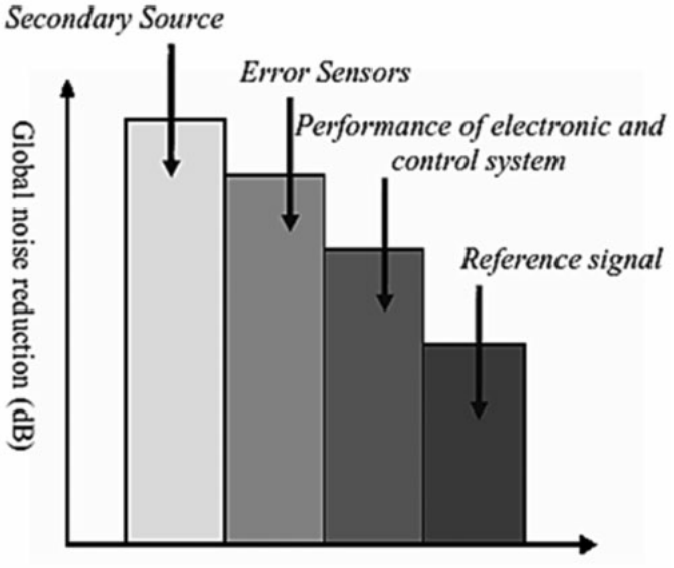

Figure 4.1: Hierarchy in ANC systems optimization (from [24])

The control loudspeakers are thus the most important components for the system optimization. The error sensors will be kept in fixed positions in order to give a certain spatial extension to the attenuation zone, in addition to noise reduction in the vicinity of the pilot's ears. The components placement is performed taking into account some positioning constraints, in order not to fall inside the pilot's head or body or hinder his sight during the flight.

4.1 Simulation settings

4.1.1 The cabin

The rectangular enclosure defined for the activity has dimensions $L_x = 1.8\ m, L_y = 1.2\ m$ and $L_z = 1.4\ m$, corresponding to a small environment that might represent the pilot cockpit of a medium-sized aircraft or helicopter (the considered cabin is based on the data of a Sikorsky UH-60 Black Hawk helicopter). The transmission media is air at room temperature, so $\rho_0 = 1.225 \frac{kg}{m^3}$ and $c = 343 \frac{m}{s}$. Each wall is represented by a single absorption coefficient according to what described in subsect. 3.2.3. A real cabin is actually much more complicated, due to non homogeneous material distribution and the presence of leaks, instrumentation, pilot, copilot and the seats themselves. For these reasons, the description of a cabin acoustics by means of six absorption coefficients only might appear as a strong approximation. Nevertheless, for this activity only a simple preliminary study is intended to be performed, so mean values will be estimated in order to approximately catch the reflections behavior. The considered boundary walls are:

- Front and lateral walls in plexiglass, with $2.5mm$ thickness
- Top wall in aluminum, with $3mm$ thickness
- Bottom wall (floor) is assumed to be highly reflective, so $\alpha_{bottom} = 0.001$
- Back wall is assumed to be quite absorbing, so $\alpha_{back} = 0.3$

Following the procedure described in subsection 3.2.3, and considering a frequency of $f_{alpha} = 400Hz$, the following coefficients are obtained:

- $\alpha_{front} = \alpha_{lateral} = 0.165$
- $\alpha_{top} = 0.063$

The value for the frequency used to estimate the absorption coefficients is the largest between the narrowband noise components (see subsect. 4.1.2), corresponding to the lowest values for the absorption coefficients and thus a more reflective cabin. The density values of lateral and top panels are $\rho_{plex} = 1180\frac{kg}{m^3}$ and $\rho_{al} = 2700\frac{kg}{m^3}$.
A more precise boundary description in a FDTD framework can be realized by introducing an irregular enclosure shape ([23], [54]) and defining a realistic distribution of the absorption coefficient over each boundary wall.

4.1.2 The excitation sources

For this Thesis the attention is focused on the low-frequency noise generated by the propellers of a medium-sized turboprop aircraft. It is also possible to extend the studies to a tiltrotor cabin noise application by simply changing the frequencies of interest, which are typically lower for these vehicles [45]. An example of the external noise spectra induced by an aircraft propeller is shown in figure 4.2. As it can be seen, the narrowband peaks are at the fundamental frequency (BPF) and its harmonics: the propeller blades induce a pressure fluctuation over the aircraft fuselage which results in an internal cabin noise at these specific frequencies as well [2]. The tonal contribution is progressively modulated at higher frequencies due to atmospheric attenuation, as stated for instance by Marte and Kurtz in [40]. The broadband noise is instead associated to vortex noise and flow turbulence. A schematic representation of propeller noise physics is summarized in fig. 4.3. Turbofan propellers RPMs typically range from 900 to 2500 $\frac{rev}{min}$. For what concerning the sound pressure intensity, the typical noise level inside a turboprop cabin can be found to be quite variable, depending on the aircraft design, engines, propellers and flight conditions [41]. For long-range turboprops a sound pressure level of $85-95dB$ (corresponding to $72-82dB(A)$) is a desirable comfort objective. Higher levels may be acceptable for shorter flights, but levels over $100dB$ or $85dB(A)$ are considered uncomfortable, as stated by Wright and Kidner [42].

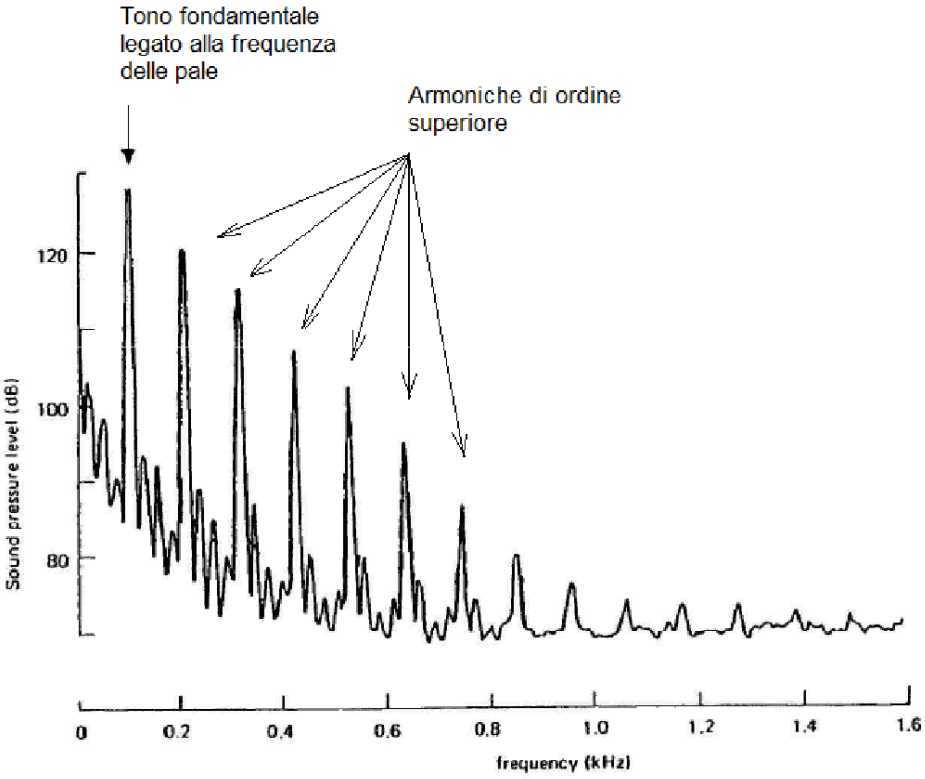

Figure 4.2: Typical propeller-induced noise (from [6])

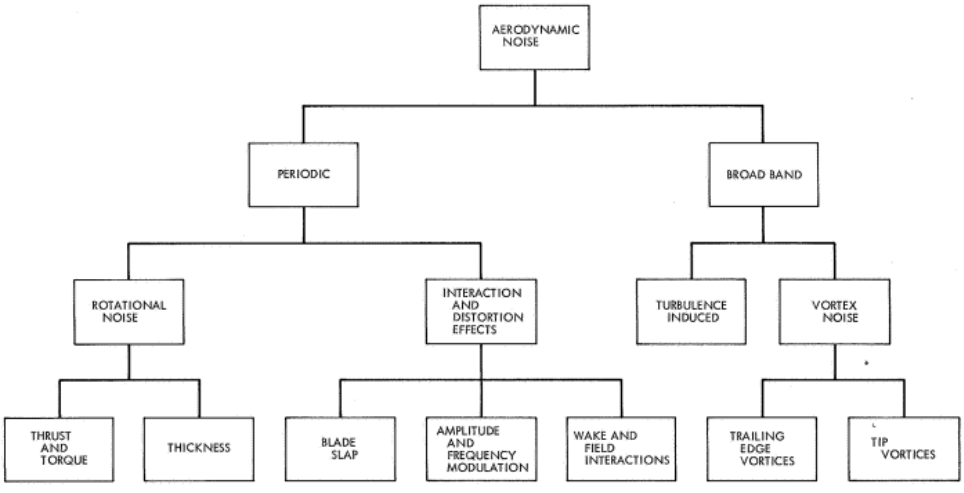

Figure 4.3: Aerodynamic noise sources in turboprops (from [40])

In the numerical simulations, the disturbance is generated by a couple of loudspeakers emitting broadband pressure signals with high narrowband peaks. They are placed in the lower angles of the back wall to simulate the presence of two aircraft propellers. Turboprop cabins sound pressure level can easily overcome the $85dB(A)$ limit in most commercial solutions without suitable low-frequency noise control techniques. The sound sources amplitudes are then set in order to provide cabin noise in this unpleasant range. This source modelling is very minimalist, since only the overall noise level is of interest for local attenuation. To obtain more detailed sound distributions in the cabin it is necessary to introduce realistic boundary vibration in the model to represent structural radiation. This could also be achieved by distributing a set of loudspeakers to simulate diffuse emission. A value of $RPM = 1500\frac{rev}{min}$ is here assumed. Considering 4-bladed propellers, the BPF can be evaluated as $BPF = \frac{RPM\ n_{blades}}{60} = 100Hz$. Moreover, three of its multiple harmonics are considered with their frequency modulation. Broadband noise is also added as band-limited white noise with a frequency content up to $700Hz$. Fig. 4.4 and 4.5 show the sources spectra of the forcing pressure that has been chosen in order to generate cabin noise level at the pilot's ears around $105dB$, corresponding to a noise between 85 and $100dB(A)$ in the considered frequency range $(100 - 400Hz)$.

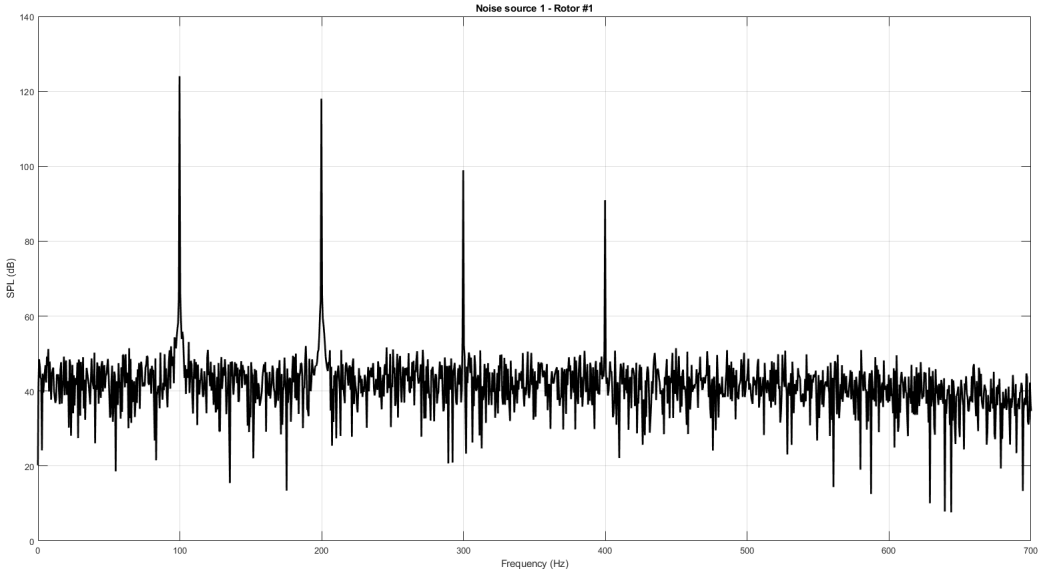

Figure 4.4: Noise spectra - 1st propeller

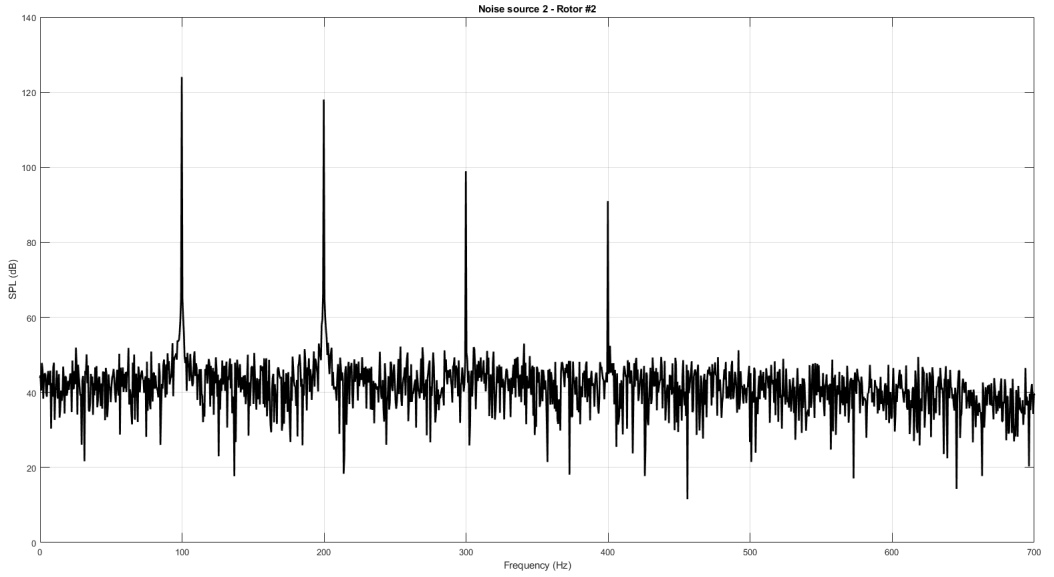

Figure 4.5: Noise spectra - 2nd propeller

The resulting sound pressure at pilot's ears level along the cabin directions x and y is represented in figure 4.6:

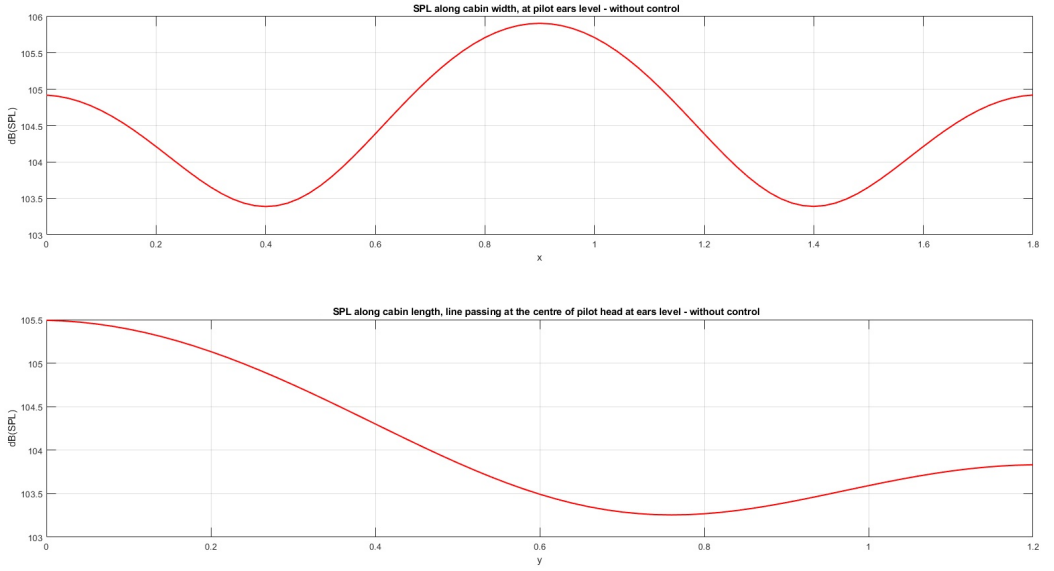

Figure 4.6: Noise SPL at pilot's ears level

The upper subplot represents the SPL along a line in the direction of the cabin width passing through the pilot's ears stations.

The lower subplot is instead the SPL along a line in the cabin length direction which passes through the center of the pilot's head. Both plots show an unacceptable noise level overcoming $100dB$.
Fig. 4.7 shows the noise frequency content at the pilot's ears stations.

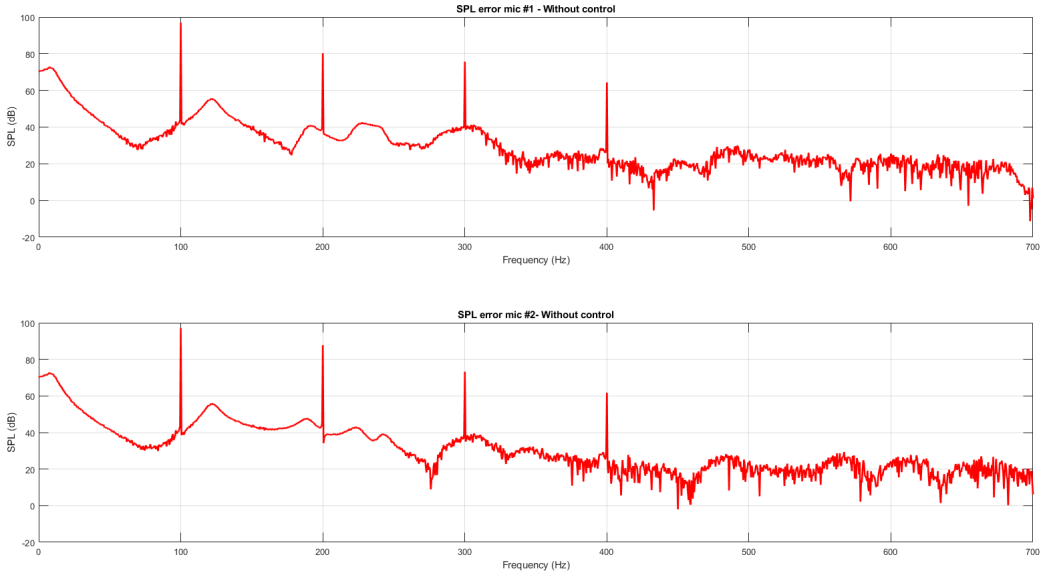

Figure 4.7: Noise spectra at pilot's ears

It is evident that the main noise contributions are at the BPF and its multiple harmonics as expected.

4.1.3 The microphones position

In order to successfully create a zone of attenuation around the pilot's head it is required to carefully place the error microphones which are used as stations where the acoustical pressure is minimized by the control algorithm. Two of the four error microphones are placed as near as possible to the pilot's ears expected positions, while the other two microphones are placed above the pilot's head in order to provide a certain spatial extension to the attenuation region, thus leaving a certain freedom of movement before being subjected to unpleasant noise levels. The reference microphone is instead placed in the cabin back wall upper vertex, at $x_{ref} = \frac{L_x}{2}$. As discussed in subsection 2.2.3, its function is to provide a certain robustness with respect to frequency mismatches that may arise during the mission. Steady engine-produced tones tend in fact to fluctuate to some extent.

Moreover, deviations between the propeller-induced noise and the reference signal frequency may be due to a wrong tachometer measure or unsynchronized propellers rotation. A picture showing the enclosure and the components defined up to this point is given in fig. 4.8. The error microphones are represented as green dots while the reference microphone as a blue one. The black squares represent the noise sources. The control loudspeakers are not present yet, since their position will be defined after an optimization process described in section 4.2.2.

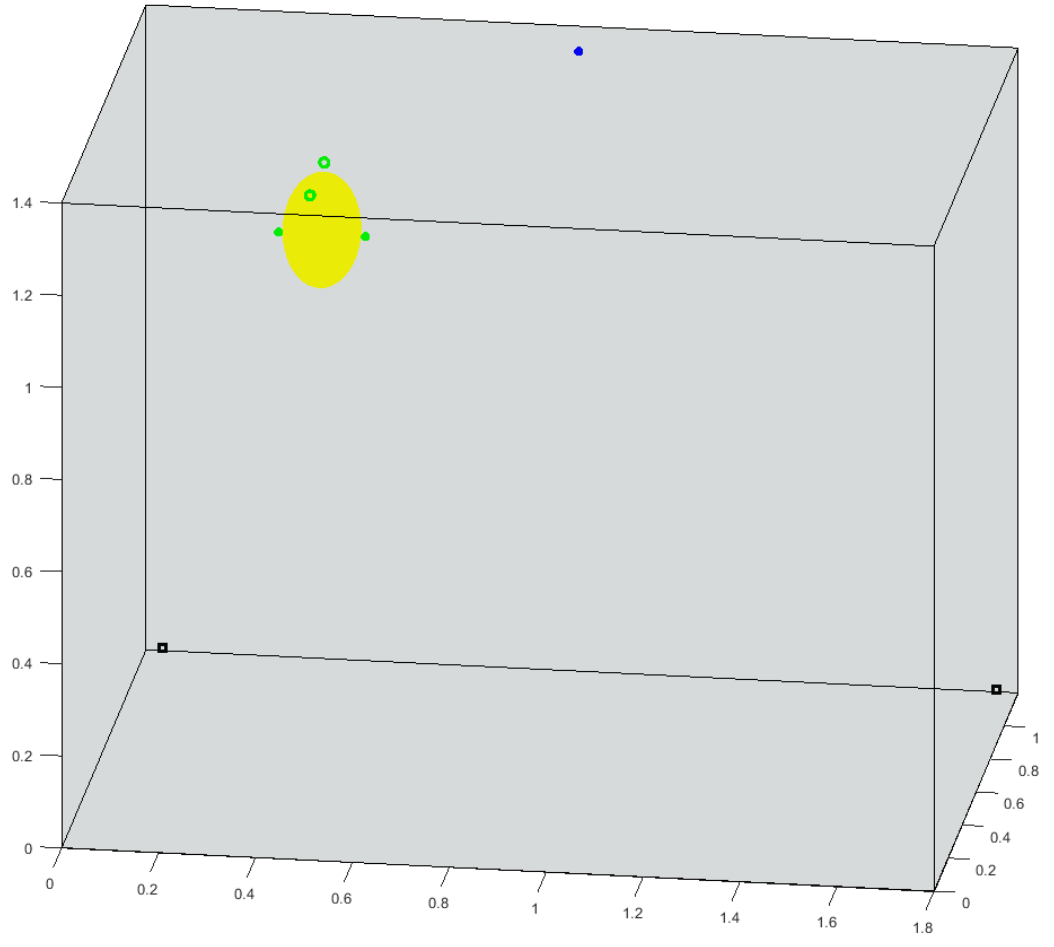

Figure 4.8: The considered cabin, microphones, and sources

With respect to the reference axes defined in fig. 4.8, the error microphones are at the following coordinates:

- Right ear error microphone (mic n°1) at
  $x_{e,1} = 0.36m, y_{e,1} = 0.6m, z_{e,1} = 1.14m$
- Left ear error microphone (mic n°2) at
  $x_{e,2} = 0.54m, y_{e,2} = 0.6m, z_{e,2} = 1.14m$
- Forward microphone (mic n°3) above pilot's head at
  $x_{e,3} = 0.45m, y_{e,3} = 0.7m, z_{e,3} = 1.26m$
- Backward microphone (mic n°4) above pilot's head at
  $x_{e,4} = 0.45m, y_{e,4} = 0.5m, z_{e,4} = 1.26m$

The pilot's head is shown in fig. 4.8 as a yellow ellipsoid with centre set in $x_{head,c} = 0.45m$, $y_{head,c} = 0.6m$ and $z_{head,c} = 1.15m$. Its dimensions are defined by its three axes, which have the following values: $l_{head,x} = 0.16m$, $l_{head,y} = 0.22m$ and $l_{head,z} = 0.24m$. These measures are provided as mean estimates for the 97.5 percentile human head, and can be found for instance in [43] and [44]. The head position has been estimated from the data on a UH-60 helicopter [68] and the work described in Goossens [69].

4.2 The performed optimization and results

The control loudspeakers configuration has been defined by means of an optimization process that will be described in this section along with the obtained results. In order to formulate a feasible resulting control system, some positioning constraints on the analysis are set: the components (error microphones and control loudspeakers) must be at a minimum distance of $5cm$, in order to keep into account real components encumbrance. Moreover, the secondary sources cannot lay inside, below or in front of the pilot's head. In addition, two or more components cannot occupy the same position. This is to avoid unrealistic configurations as well. Furthermore, the solution is constrained to be be symmetrical with respect to a plane parallel to the YZ plane and passing through the centre of the pilot's head, unless mistakes due to the finite spatial step size of the mesh.

The control sources are free to move behind, next to and above the pilot's head, by moving on planes parallel to the enclosure ones with a maximum distance from the pilot head centre of $15cm$. As a matter of fact, the attenuation performances are enhanced by keeping the loudspeaker positions as near as possible to the error microphones [8]. However, as stated for instance in David and Elliott [49], the dimensions of the quiet zone are increased as the distances between the cancelling stations and the secondary sources are increased. Since both the attenuation and the size of the quiet zone are important performance indicators, a compromise will be the object of the research in the optimization framework. In practical applications however, other phenomena typical of local noise attenuation are likely to reduce the predicted performances, mainly the acoustical coupling between the pilot's head and the error microphones (Garcia et al., [46]) and the pressure gradient near the control loudspeakers (Joseph et al., [48]). These effects have not been taken into account for the following analysis, but might be addressed as future activities.

4.2.1 The parameters for identification and control

The parameters for the acoustical paths identification are $\mu_{iden} = 0.3$, $\nu_{iden} = 0.999999$ and $L_{iden} = 512$. The total time of identification is set to $T_{iden} = 1s$. An high order filter is then used since the identification is performed offline and it does not affect the computational cost of the real time control. The adequacy of this parameters combination is evaluated in the aftermath, by checking the identification errors behavior (see for instance fig. 4.14 - 4.16). The considered narrowband signals are

$$\begin{aligned} x_A(t) &= 0.5cos(2\pi\ BPF\ t) + \sum_{i=2}^{4} 0.1cos(2\pi\ i\ BPF\ t) \\ x_B(t) &= 0.5sin(2\pi\ BPF\ t) + \sum_{i=2}^{4} 0.1sin(2\pi\ i\ BPF\ t) \end{aligned} \tag{4.1}$$

More effort is then targeted in the BPF cancelling, consequently to its relevance in the spectra in fig. 4.7. No frequency mismatches are introduced (perfect tachometer estimation). The control frequency is about $f_{contr} = 5660Hz$.

Control parameters have been tuned on the basis of a previous series of analysis with a trial & error approach, with the idea of searching for a combination of μ_{contr}, ν_{contr} and L_{contr} showing the best tradeoff in terms of stability, performances and number of control filter taps. More precisely, in order to lower the computational burden and thus allowing faster implementation, L_{contr} is kept under 200 taps. Observations on μ_{contr} and L_{contr} changes could be made relying of simplified analytical consideration in sect. 1.3 and 1.4. Formulas 1.54 and 1.45 show that an increase in L_{contr} negatively affects the stability and thus the convergence rate, while formulas 1.52 and 1.39 show that L_{contr} should be increased for overall performances enhancement. A possible practical approach is then to fix ν_{contr} and L_{contr} instead, set a small μ_{contr} and increase this learning rate progressively by half of an order of magnitude until signs of instability can be detected in the time behavior of the error microphones pressures performing simulations over a random admissible sources configuration. This tuning is rather simplified and time-consuming, but it is indeed required also during experimental activities for complex environments and control configurations. Variable step size could be used to reduce the tuning effort. The control parameters values that have been chosen of the basis of these considerations over a set of trial simulations are $\mu_{contr} = 0.000035$, $\nu_{contr} = 0.9999$ and $L_{contr} = 180$. The total control time for the optimization simulations is set to $T_{contr} = 1s$. Performances enhancement with proper loudspeakers placement will be instead the task of the following subsection.

4.2.2 The optimization simulations

Applying conventional optimization schemes (such as gradient-based or genetic optimization) to a real-time evolving model is no easy task. An optimization based on the genetic algorithm has been proposed for example in [24]. For this activity however, another approach has been chosen. Due to the relatively small amount of possible configurations in such a limited region, a series of analysis is automatically performed on all the admissible combination of positions. The final configuration is associated to the lowest value of a function v evaluated after each run:

$$v = \sqrt{1.5\ SPL_1^2 + 1.5\ SPL_2^2 + SPL_3^2 + SPL_4^2 + SPL_{o1}^2 + SPL_{o2}^2} \tag{4.2}$$

The definition of v contains the SPL computed for 6 microphones over a limited time ($1s$), in order to reduce the total cost of the analysis. Four microphones out of six are the error microphones, two of which (the ones near the pilot's ears stations) are weighted by a factor 1.5. The remaining two microphones are in the plane parallel to the $y-z$ plane containing also the microphones above the pilot's head, thus extending the expected quiet zone along the cabin height dimension too. A plot of the microphones used for the optimization process is provided in fig. 4.9, where the additional virtual microphones are plotted as white dots.

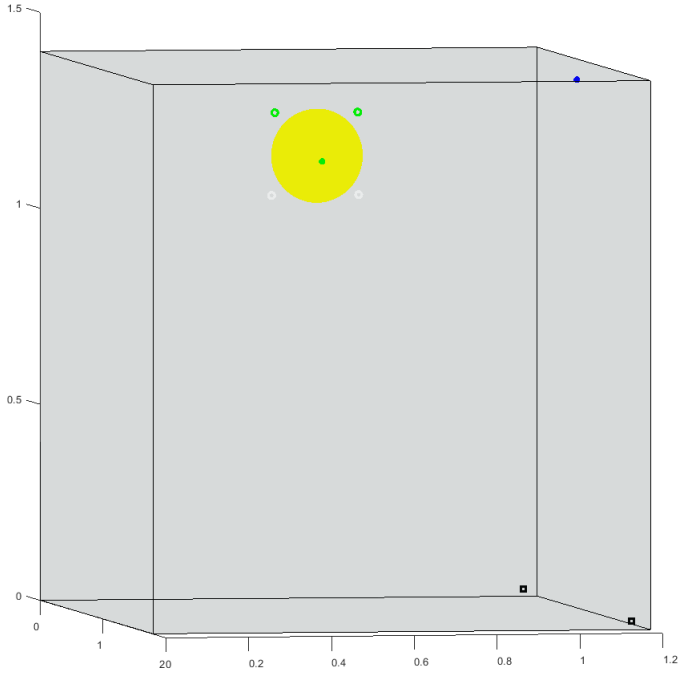

Figure 4.9: View on the error and virtual microphones used for optimization

The acoustical analysis parameters are $h = 0.035m$ and $\delta t = 5.8913e-05s$, corresponding to $f_{max} = 980Hz$ with 10 elements in its wavelength. This mesh is quite coarse with respect to the small characteristic dimensions involved in this local control application, but it has been used in order to compute the optimization results within seven hours of single-core serial computing. Parallel computing or GPU implementation might drastically speed up the process. In subsect. 4.2.3 the resulting configuration will be tested on a finer mesh to provide more reliable results. $n_{contr} = 3$ acoustical simulations are performed between two control actions.

A random error on the measures provided by the reference microphone and error microphones is also added. Its magnitude ranges from -5% to $+5\%$ of the measured value. It is now worth noting that the number of loudspeakers ($K = 4$) of the control algorithm described in Chapter 2 and here exploited has been chosen as a reasonable tradeoff between computational effort and the formulation of an optimization with a sufficient number of free parameters (the loudspeakers positions) to tune. The resulting configuration is shown in fig. 4.10-4.13, where the control loudspeakers are represented as red squares. As it can be seen, the resulting optimized configuration is almost symmetrical apart from a small asymmetry due to the finite stepsize h. The control sources do not penetrate the dome nor they overlap with the error microphones, and do not fall below or in front of the pilot's head. Two loudspeakers are placed $5cm$ behind the ears, so as close to them as possible, as might be expected to obtain significant local attenuation. Two additional loudspeakers above the pilot's head are placed at roughly the same distance from the cancelling microphones leading to a quite regular distribution, in order to provide also spatial extension to the quiet zone in addition to acoustic attenuation.

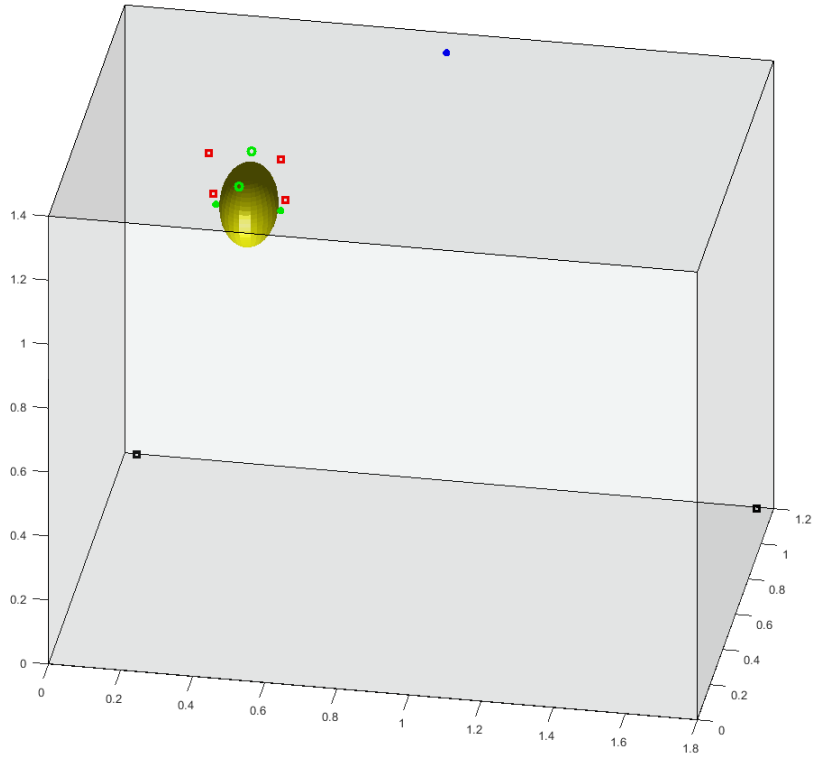

Figure 4.10: The optimized configuration - Isometric view

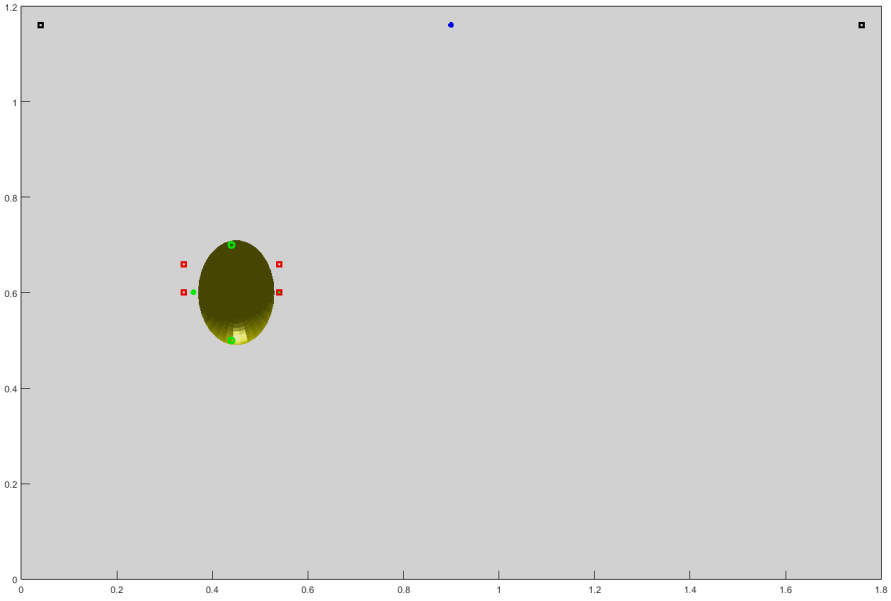

Figure 4.11: The optimized configuration - Top view

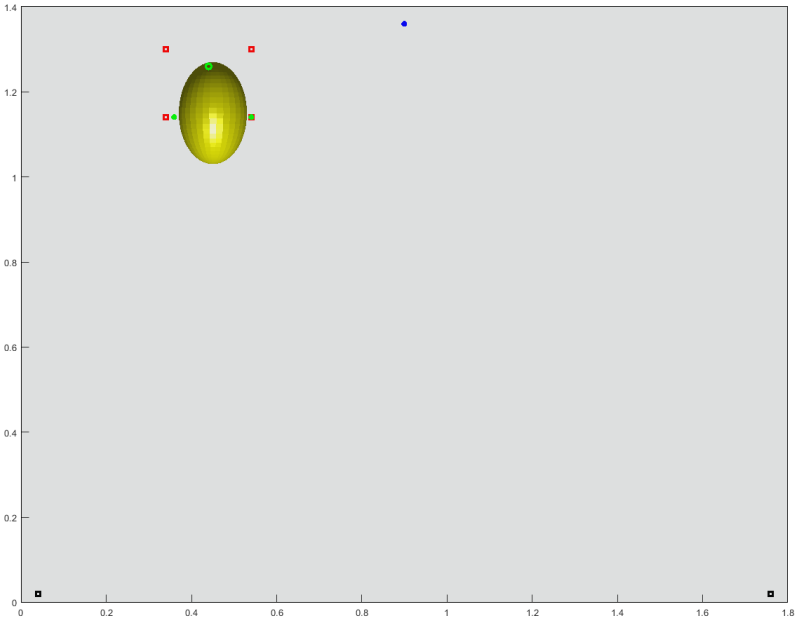

Figure 4.12: The optimized configuration - Front view

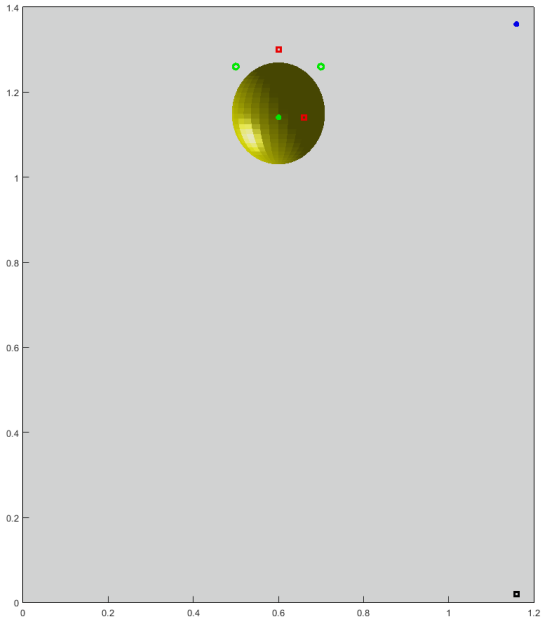

Figure 4.13: The optimized configuration - Lateral view

The optimized control loudspeakers positions (in the reference system defined in fig. 4.10) are:

- Right ear loudspeaker at
  $x_{s,1} = 0.35m, y_{s,1} = 0.65m, z_{s,1} = 1.15m$
- Left ear loudspeaker at
  $x_{s,2} = 0.55m, y_{s,2} = 0.65m, z_{s,2} = 1.15m$
- Right loudspeaker above pilot's head at
  $x_{s,3} = 0.35m, y_{s,3} = 0.6m, z_{s,3} = 1.3m$
- Left loudspeaker above pilot's head at
  $x_{s,4} = 0.55m, y_{s,4} = 0.6m, z_{s,4} = 1.3m$

4.2.3 Results on a finer mesh

The configuration obtained in subsect. 4.2.2 has then been tested by considering a finer mesh in order to provide more reliable results in terms of performances and SPL distribution. The acoustical simulation parameters are set to $h = 0.02m$ and $\delta t = 3.3665e-05s$, corresponding to a $f_{max} = 1715Hz$ with 10 elements in its wavelength. The same parameters with respect to the optimization phase are set for the identification and control sessions, with the only difference that the control simulation is performed over 2 seconds. Longer simulation times are computationally heavy, and are not required: the practical interest is in the the rapidity of the control system to reduce effectively the noise, so a small simulation time of only 2 seconds is reasonable. After a quick transient, a stable control configuration will be able to keep the steady error from there on. The control frequency is $f_{contr} = 9900Hz$, corresponding to $n_{contr} = 3$ simulation steps between each control action. The same measurement error on the microphones added in the optimization phase is considered for this analysis as well. The identification results are shown in fig. 4.14, 4.15 and 4.16. These plots represent the acoustical pressures at the error and reference microphones stations. A correct estimation is associated to a small residual error (green line) during a suitable identification time. It is evident that the identification of the acoustical feedback paths is not precise as expected from the numerical simulations presented in subsection 2.2.1. This may be due to the placement of the reference microphone in a vertex of the enclosure, which results in an heavily modal response. A periodicity in the measured noise is in fact appreciable, and this may reduce its correlation with respect to the reference signal (white noise). Nevertheless, Kuo [8] suggested to place the reference microphones where the modal contribution is maximixed (i.e. the enclosure angles), as far as possible from the control region (to reduce acoustical feedback effects) and as near as possible to the noise sources. In addition, the control configuration must be stable. On the basis of these aspects, this reference microphone position is kept. On the contrary, secondary paths identification errors behavior resembles the one obtained in the numerical simulations in Chapter 2. It is also possible to insert in the numerical model experimentally-evaluated feedback or secondary paths to enhance the simulation accuracy.

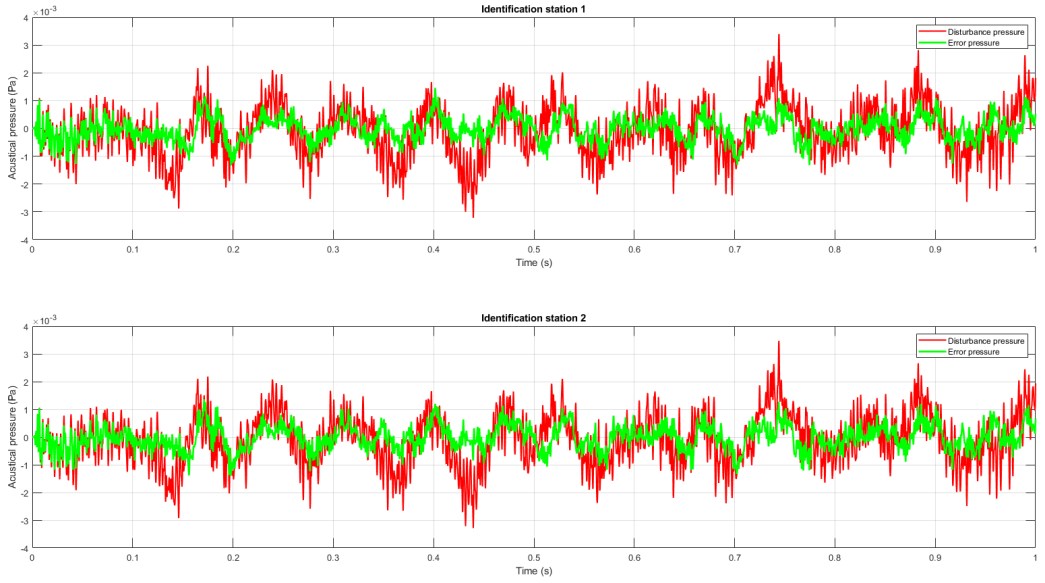

Figure 4.14: Identification error at microphones near pilot's ears

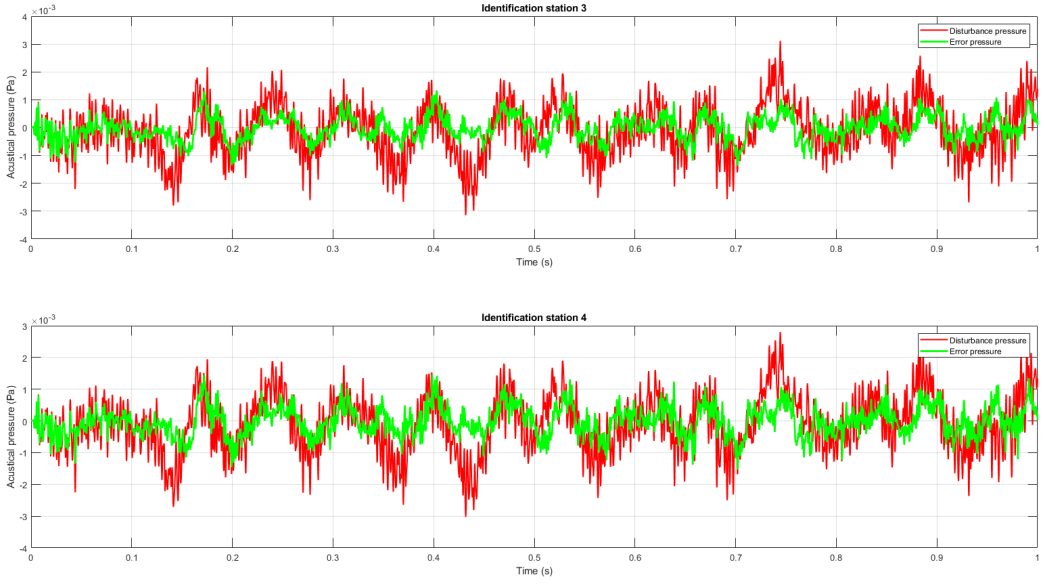

Figure 4.15: Identification error at microphones above pilot's head

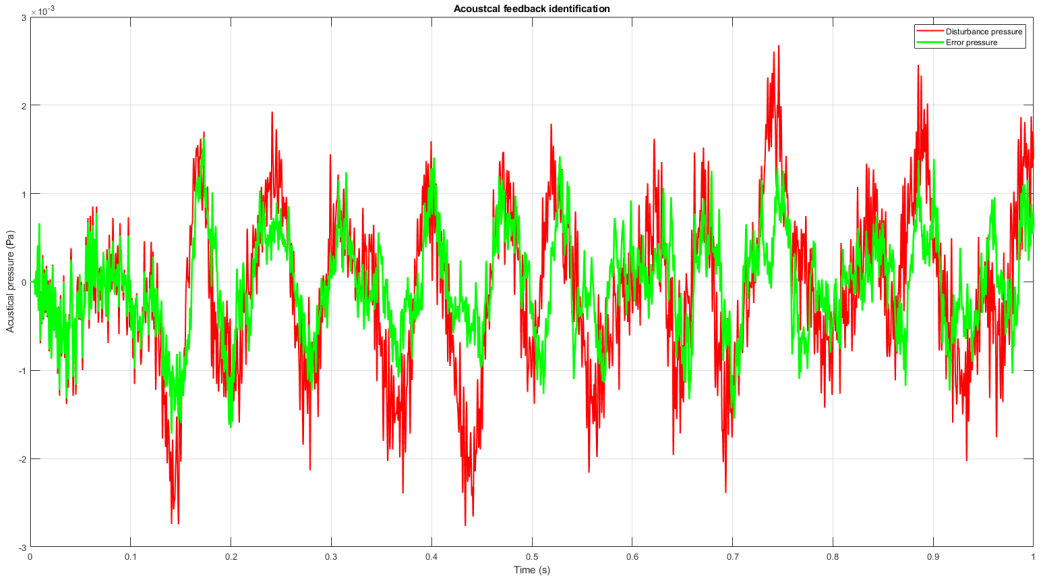

Figure 4.16: Acoustical feedback error identification

The final configuration results in terms of noise reduction and attenuation region size are shown in figures 4.17 and 4.18. Red curves represent cabin noise without control while green ones are the cabin noise with the ANC system enabled. Fig 4.17 shows the behavior along cabin width and length of the acoustical pressure evaluated after 2 seconds in dB, thus it does not take into account the frequency weighting performed by the human auditory system.

Figure 4.18 represents the very same results but the noise levels are plotted as bands ranging from the pressure values A-weighted at $100Hz$ to the pressure values A-weighted at $400Hz$. This provides a subjective noise measure that can be easily related to the ones present in literature and certification documentation. The considered A-weighting filtering function [50] is $A = A(f)$:

$$A = 20log_{10}\left(\frac{12194^2 f^4}{(f^2+20.6^2)\sqrt{(f^2+107.7^2)(f^2+737.9^2)}(f^2+12194^2)}\right) + 2 \tag{4.3}$$

corresponding to the blue curve in figure 1.3. Its value evaluated for a given frequency and added to the SPL gives the sound pressure as perceived from our auditory system.

Vertical green lines represent the error microphones positions while red vertical lines are plotted at the control loudspeakers stations. The plots are obtained in the very same manner as the ones in fig. 4.6.

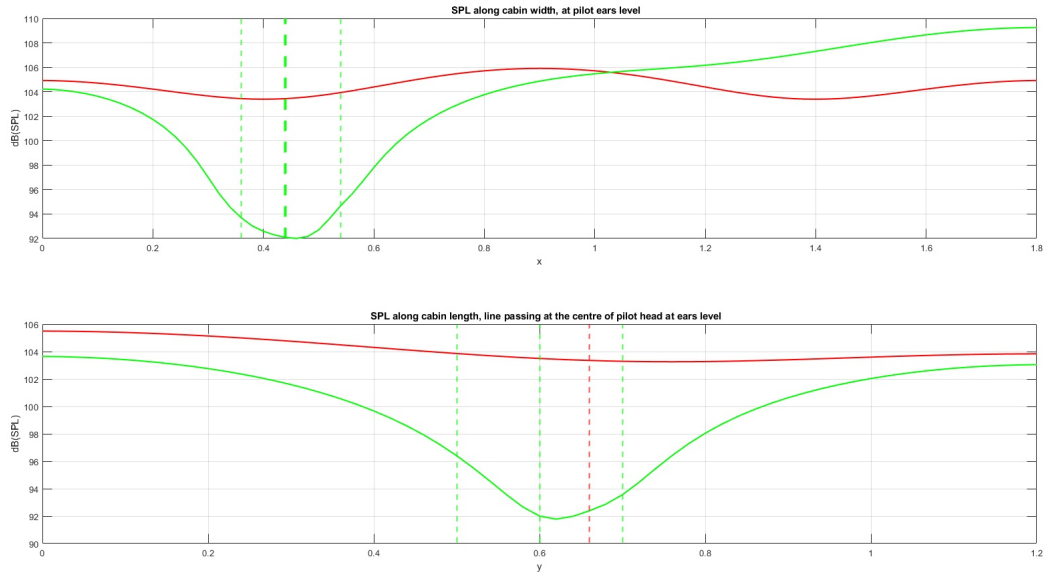

Figure 4.17: Cabin noise distribution - Optimized configuration dB

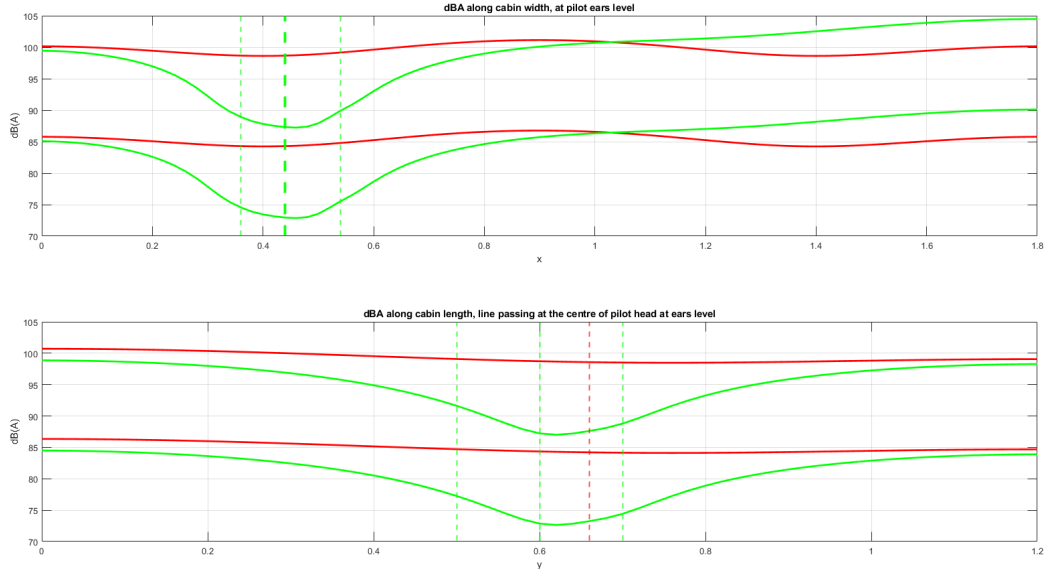

Figure 4.18: Cabin noise distribution - Optimized configuration dB(A)

The attenuation recorded at the error microphones is summarized in table 4.1:

	SPL (dB) without control	**SPL (dB) with control**	**Noise reduction in dB**
Mic 1	103.4	93.7	9.7
Mic 2	103.9	94.7	9.2
Mic 3	103.9	96.4	7.5
Mic 4	103.3	93.6	9.7

Table 4.1: Noise attenuation after 2 seconds at the error microphones

Results from table 4.1 and figure 4.17 and 4.18 show that almost $10dB$ of noise reduction can be obtained exploiting the proposed control configuration within $2s$ of simulation. Considering the imposed noise level, the comfort limits previously described can then be reached. The presence of a local attenuation zone is also evident from figures 4.17-4.18. Its spatial extension is quite limited though, since at about $10cm$ of distance from the head the pressure level still can overcome $100dB$. As a matter of fact, in local noise control systems the attenuation region size associated to a single secondary source in an enclosure diffuse sound field is estimated as $\frac{1}{10}\lambda$, where $\lambda = \frac{c}{f}$ is the wavelength of interest (Abbott, [47]).
Since the fundamental harmonic (the BPF) has a wavelength equal to $3.43m$, this corresponds to around $30cm$ of expected dimension of the attenuation region. The major drawback is however the increase of the noise level far from the control region. Nevertheless, the noise is still attenuated from an $85 - 100dB(A)$ range to a $75 - 90dB(A)$ one in the vicinity of the pilot's head, which can be considered a good comfort enhancement with respect to this system relatively low complexity.

A time domain representation of the acoustical pressures recorded at the reference microphones is given in figure 4.19 and 4.20. In this domain it is easier to check the stability of the control system:

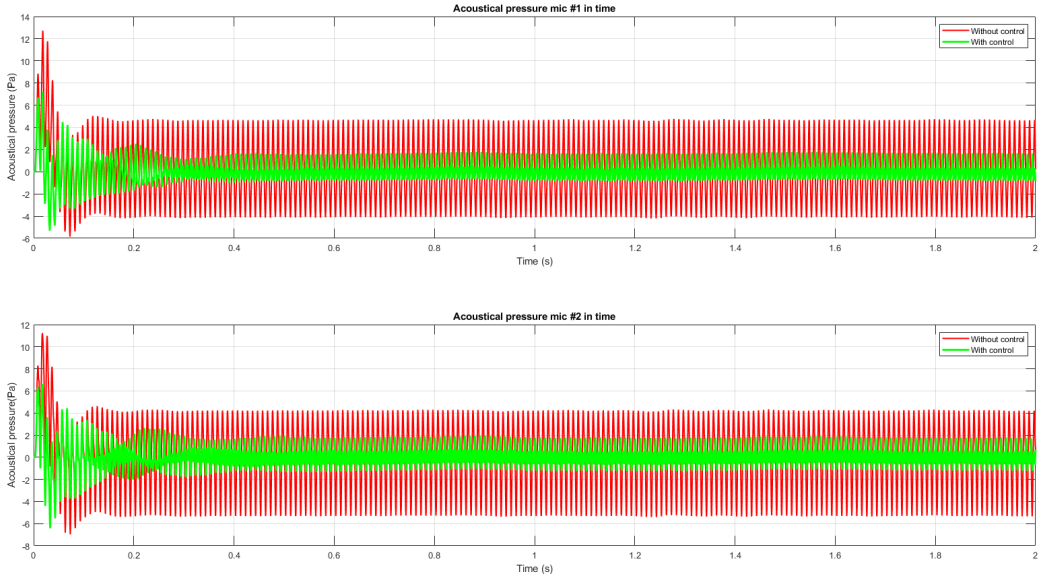

Figure 4.19: Pressure behavior in time at error microphones 1 and 2

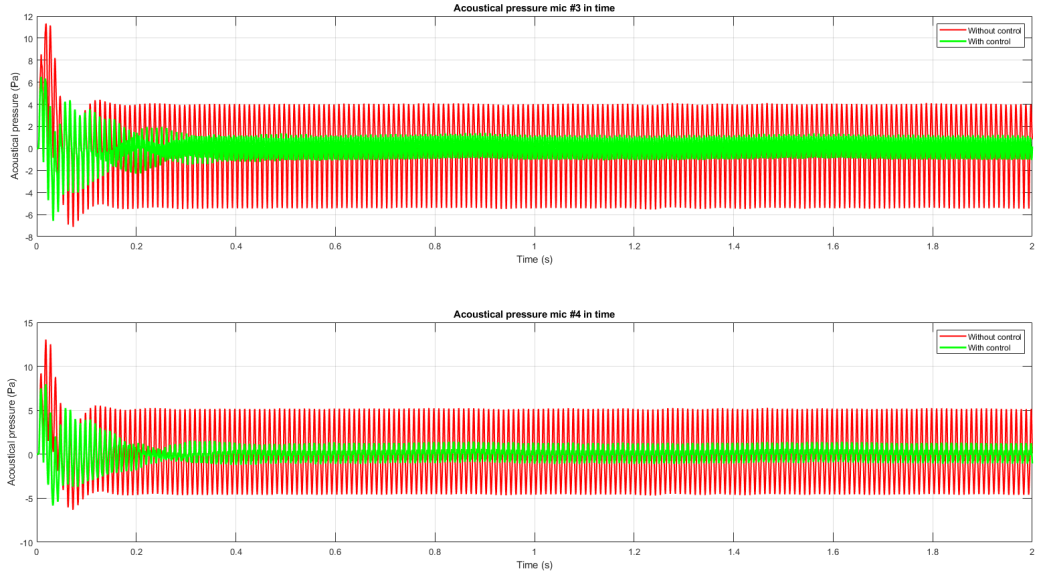

Figure 4.20: Pressure behavior in time at error microphones 3 and 4

Their frequency representation is instead provided in figure 4.21 and 4.22.

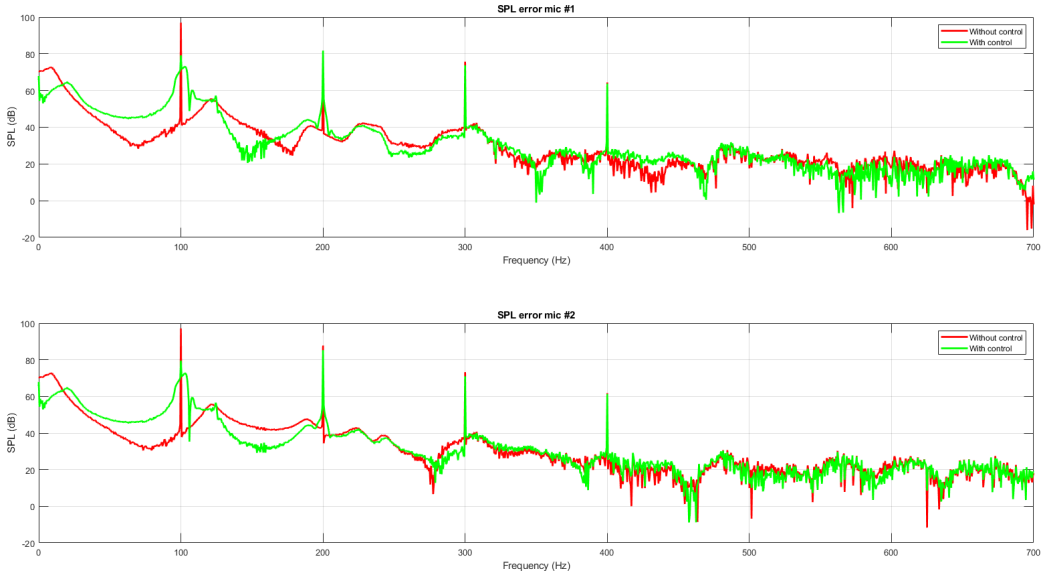

Figure 4.21: Noise spectra at error microphone 1 and 2

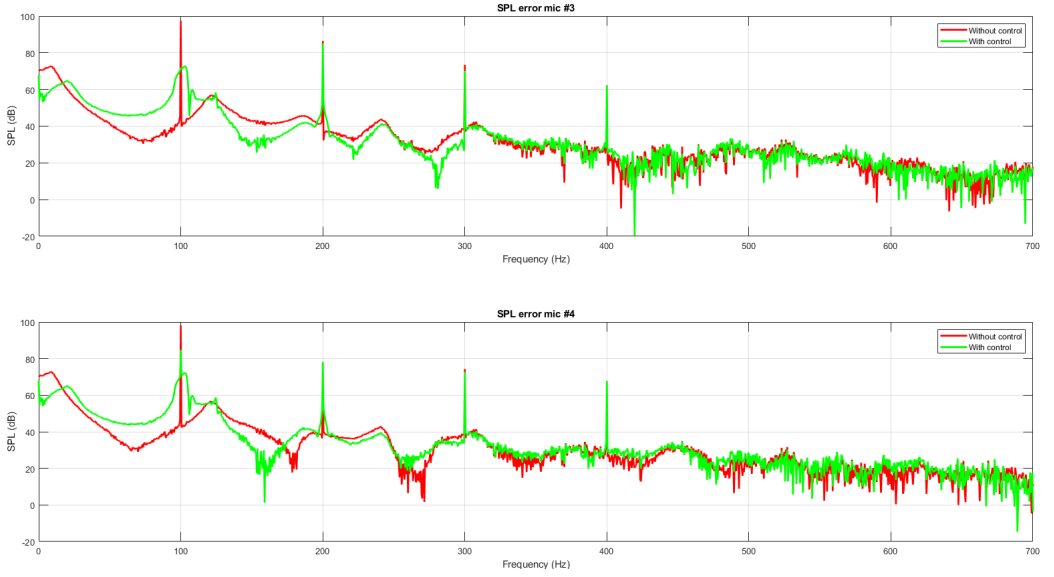

Figure 4.22: Noise spectra at error microphones 3 and 4

These results show the control system mainly affects the BPF, which is something to be expected due to the larger contribution of this spectral component in the reference signal. Moreover, adaptive tracking of the most prominent frequency content is desired.

4.3 Test with un-synchronized propellers

A case of practical concern may be the study of the performance degradation of the control when the propellers are not perfectly synchronized. While in a steady cruise condition the synchrophaser unit is able to keep the same rotation rate, during non-stationary flight conditions (such as the climb to steady cruise flight condition), it may be unable to keep the propellers fully synchronized at all times, resulting in slight deviations in the RPM. This topic has been discussed also by Johansson in [2].
For the following analysis, two reference signals at the nominal BPF ($100Hz$) are given as a reference for the controller, but the propeller #2 is assumed to be rotating at $105Hz$, thus introducing a frequency mismatch equal to $5Hz$. The cabin noise level considered for this analysis is again around the discomfort level previously defined ($100dB$). A part from these differences, the simulation settings are identical to the ones defined in subsection 4.2.3. Rotor #2 spectrum is plotted in figure 4.23, while the cabin SPL distribution is shown in figure 4.24 and the noise spectrum at the pilot's ears is shown in figure 4.25.

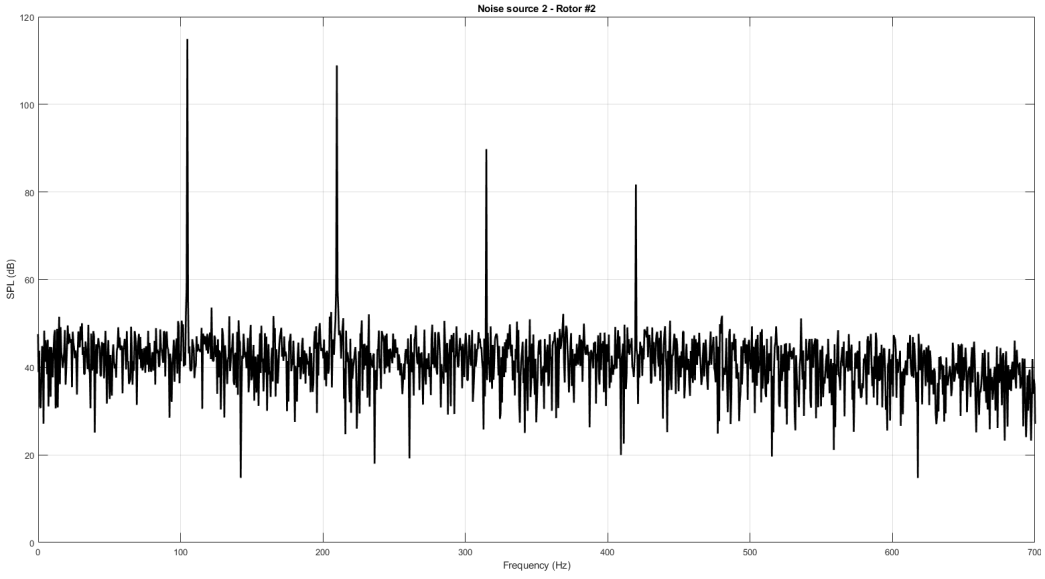

Figure 4.23: Noise spectra - 2nd propeller

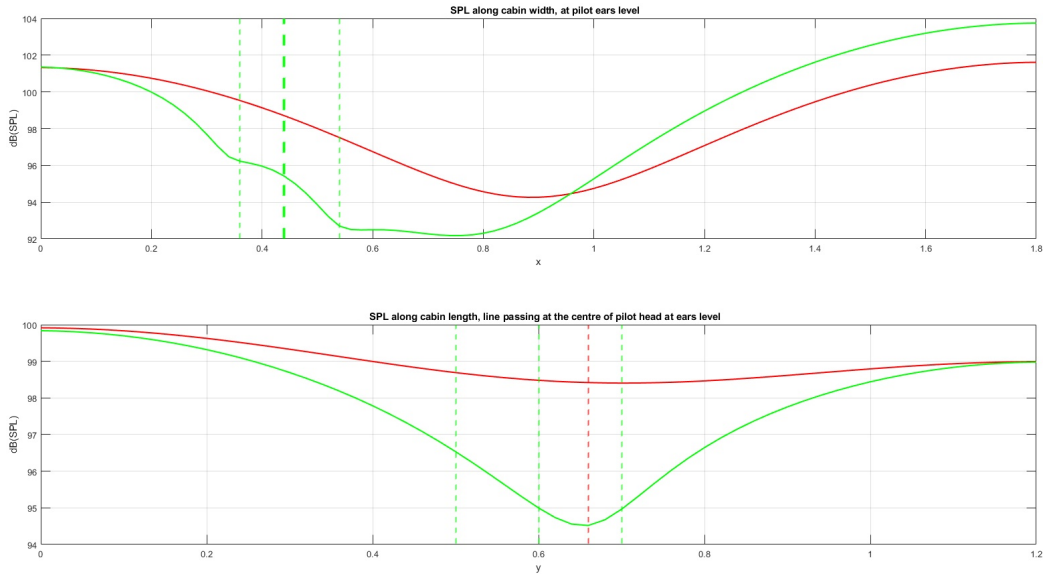

Figure 4.24: Cabin SPL distribution (dB) - Optimized configuration, different propeller velocities

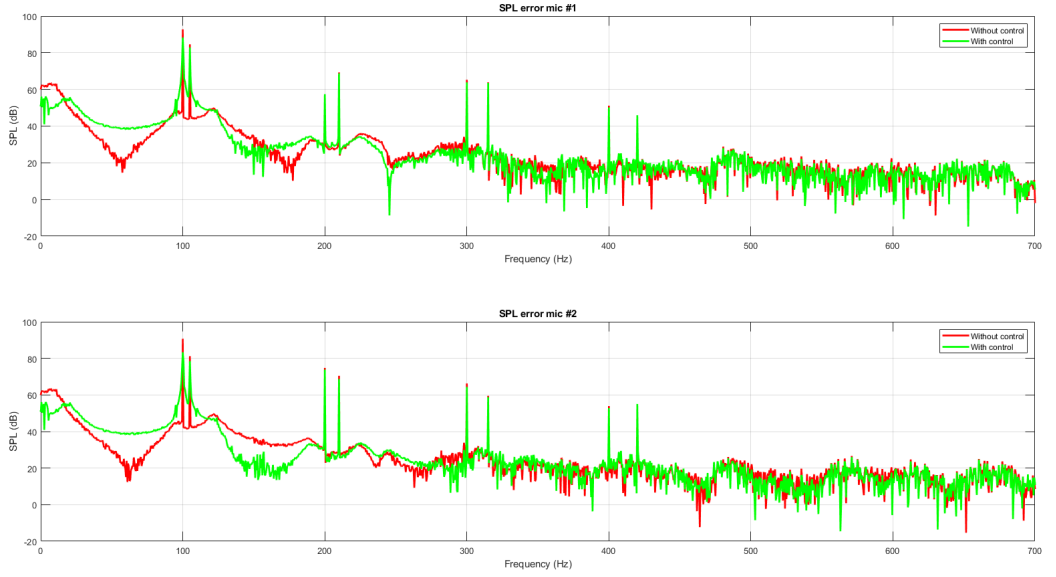

Figure 4.25: Noise spectra at error microphone 1 and 2 (dB), different propeller velocities

The attenuation recorded at the error microphones in this new condition is given in table 4.2. As it can be seen, the performance degradation in terms of overall attenuation and quiet region size is significant. An improvement in the convergence rate has been obtained by keeping this control configuration and increasing the first narrowband signals component amplitude. This result is

compliant with the adaptive notch filter theory presented in sect. 1.4.

	SPL (dB) without control	**SPL (dB) with control**	**Noise reduction in dB**
Mic 1	99.5	96.2	3.3
Mic 2	97.5	92.7	4.8
Mic 3	98.7	96.5	2.2
Mic 4	98.4	95	3.4

Table 4.2: Noise attenuation after 2 seconds at the error microphones, different propeller velocities - $A_1 = 0.5$

Table 4.3 shows the attenuation with a new control configuration in which the first reference signal amplitude is increased from 0.5 to 2, while keeping a single tachometer measure.

	SPL (dB) without control	**SPL (dB) with control**	**Noise reduction in dB**
Mic 1	99.5	93.2	6.3
Mic 2	97.5	89.4	8.1
Mic 3	98.7	94.4	4.3
Mic 4	98.4	91.9	6.5

Table 4.3: Noise attenuation after 2 seconds at the error microphones, different propeller velocities - $A_1 = 2$

An improvement in the overall noise reduction is obtained, but this control configuration did not turn out to stable in the previous case of both propellers rotating at the same speed. An external tuning for the reference amplitude would then be required on the base of the operational condition, but it might result unpractical. An alternative approach would be to exploit two separated tachometer measures, but the narrowband control configuration should be changed as well. In fact, direct configurations with single multicomponent signals and closely spaced tones do not perform well for low L_{contr}. Parallel configurations are more effective solutions for this cases, but they require the splitting of the frequency content into multiple reference signals in quadrature, requiring in any case an increment in the computational effort. Direct/parallel configurations represent a better tradeoff, balancing control performances and cost increases [8].

4.4 Test with two control systems

Another interesting case of study is the simulation of two close control systems for local noise attenuation. They're placed at a relative distance $d_c = 40cm$, in the centre of the enclosure defined in subsection 4.1.1. This could be representative of the application of the previously described control configuration for noise attenuation around two passengers heads. The simulation and control parameters are set in compliance with what described in subsections 4.1.2, 4.2.1, and 4.2.3. Fig. 4.26 shows this new solution layout:

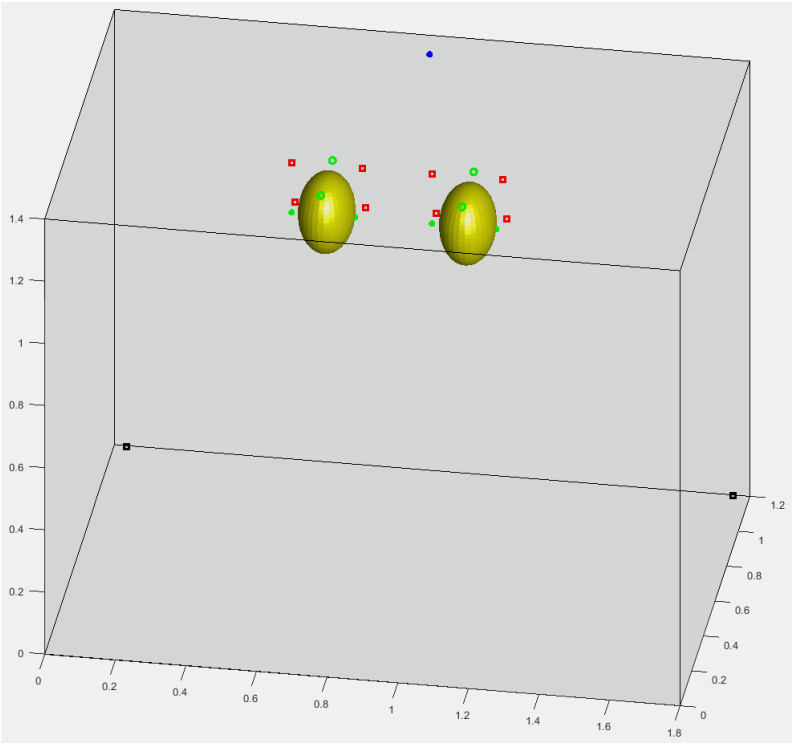

Figure 4.26: Coupling of two control systems - Isometric view

Results in terms of SPL distribution are given in fig. 4.27, while table 4.4 summarizes the attenuation at the 4 error microphones near to the ears for both the left control system and the right one.

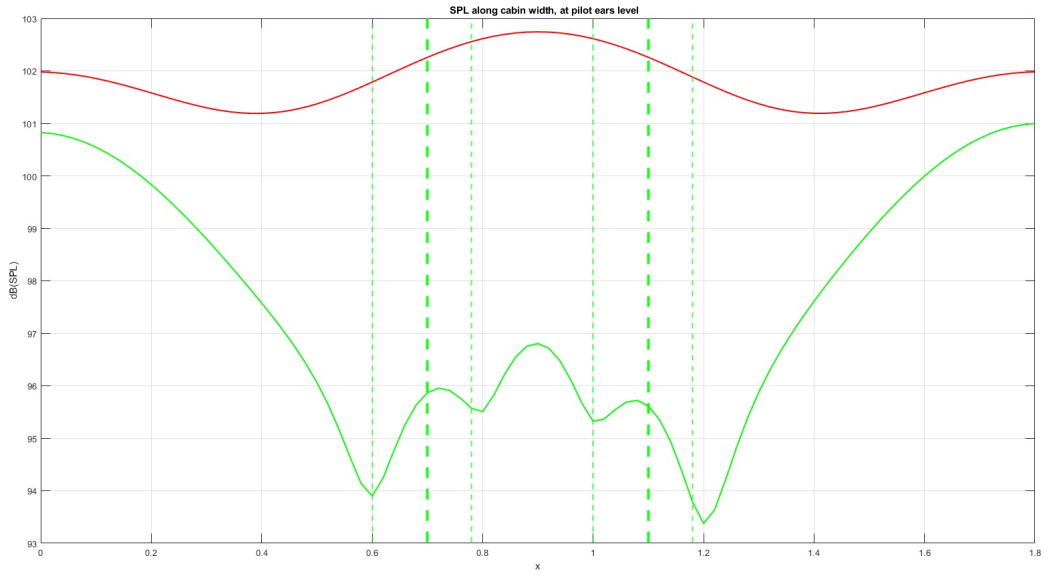

Figure 4.27: Coupling of two control systems - Red : SPL without control; Green : SPL with control

	SPL (dB) without control	**SPL (dB) with control**	**Noise reduction in dB**
Mic 1 - left	**101.8**	**93.9**	**7.9**
Mic 2 - left	**102.6**	**95.6**	**7**
Mic 1 - right	**102.6**	**95.3**	**7.3**
Mic 2 - right	**101.9**	**93.8**	**8.1**

Table 4.4: Noise attenuation at passenger's ears after two seconds, with both systems enabled

Around $7 - 8dB$ of attenuation can be obtained in vicinity of the ears, in contrast with $9 - 10dB$ of section 4.2.3. This slight change may be due to two reasons. The first is the performances are affected by the heads position in the enclosure. This holds for a single control system as well, and it is related to the reflections dynamics and how the control loudspeakers couple with this small acoustic space walls, meaning that an enhancement in the boundary modelling could affect the results of the proposed configuration even for local noise attenuation. The second reason is that in presence of two control systems there is a mutual interaction recorded as error pressures measures coming from the action of all the 8 control loudspeakers. As a matter of fact, this coupling has not been compensated by changes in the algorithm and can affect the control convergence rate within 2 seconds of run, as well as its stability.

Chapter 5

Conclusions and future work

A simulation tool has been developed in MATLAB environment in order to test a multi-channel noise control algorithm performances in a reverberant enclosure excited by typical propeller-induced noise. The interest has been focused on the attenuation of low-frequency turboprop cabin noise, in order to provide an optimized solution for an active headrest. For what concerning the results, the obtained optimized configuration shows an interior disturbance reduction going from 7.5 to $9.7dB$ at the error sensor stations within 2 seconds, for a cabin noise going from the range $85 - 100dB(A)$ to $75 - 90dB(A)$. The smallest sound variation our auditory system is capable of detecting is around $3dB$ [36]: under this perspective, the results show the obtainable performances are quite poor. Nevertheless, literature papers and current industrial solutions based on FxLMS algorithms certify an achievable noise reduction around $10 - 15dB$. Sometimes articles even refer specifically to $10dB$ quiet zones ([49], [48]). Better performances can be indeed achieved in active headphones, but at an higher cost. An active headrest like the one analyzed for this activity is cheap and relatively easy to build, and can act as a useful support to other preexisting noise control techniques for typically low frequency ranges in which they perform poorly, but it might not be sufficient as the only one to rely on, in particular outside nominal operational conditions. As a matter of fact, noise control in aeronautical applications consists in a variety of coexisting solutions ([7]). On the other hand, for some applications it may not even be necessary to reach higher performances, since the human auditory system is less sensible to low-frequency noise. This means that the BPF, which is the most prominent frequency content for turboprop or tiltrotor cabin noise, will be less impacting on the flight comfort then the

other harmonics at higher frequencies, thus leading to a presumably smaller required noise reduction. A value for the cabin noise under $85dB(A)$ is considered an acceptable flight condition (Wright and Kidner, [42]). As a final consideration, local active noise control systems are characterized by a fairly good portability, as confirmed by commercial solutions that can be installed on airplane cabins as well as on boats and cars.
Some additional work might be performed starting from this activity. Since the numerical method used for this Thesis is quite costly, a GPU implementation of the algorithm could considerably speed up the simulations providing results on finer meshes and larger environments in a reasonable time. This approach has been extensively used for FDTD based methods both in computational electrodynamics (Lopez et al., [51]) and acoustics ([70], [52]). For what concerning the simulation itself, the main improvement to be done to correctly analyze local noise attenuation is to include the acoustics of a simplified head model, in order to take into account its effects on the control loudspeakers configuration optimization. As stated for instance in [46], the head presence is likely to cause an increment in the distance between the error microphones and the pilot while keeping them relatively close to the secondary sources. In an FDTD framework it might be inserted as a small box with a given absorption coefficient. A human head is expected to be quite absorbing due to the hair presence (in analogy on test performed on haired laboratory animals, for which sound is converted into heat in the small pores between the hairs) while the human tissues are more reflective [53]. Other improvements might be the introduction of irregular boundaries and their modelling with a spatial distribution of the absorption coefficient. An interesting generalization of the FDTD method is given in [54]. Even for local zone attenuation, reflections in small environments affects the control performances, as stated in sect. 4.4. Moreover, the loudspeakers generating the disturbances might be substituted by a given velocity imposed to one (or more) vibrating boundary wall(s) representing the fuselage panels vibration, or could be distributed to simulate diffuse radiation. The optimization might be performed with time-varying noise frequency content to check for differences in non-stationary flight conditions with respect to stationary ones. Finally, the control algorithm itself can be changed in any of its aspects, in order to enhance its stability, convergence rate and steady error performances. Slightly more complicated FxLMS algorithms are the normalized one (NFxLMS), the block-LMS and the signed-LMS [9]. Other

possible approaches are the implementation of variable-size LMS based algorithms (VSS-FxLMS) or frequency-based FxLMS algorithms. Kwong and Johnston proposed an interesting law of adaptation of the control step-size μ regulating it in proportion of the residual error [55]. A novel frequency-FxLMS algorithm has been instead derived by Yang et al. [56]. Johnasson [2] proposed a multichannel complex-LMS algorithm for turboprop and helicopter cabin noise attenuation, involving the use of a considerable amount of error microphones for a cabin noise attenuation around $20dB$. An instantaneous frequency estimation procedure can also be added: a suggestion is given in Appendix A. In addition, results in section 4.3 show that frequency mismatches degrade the performances, as it may be expected: a change in the narrowband control configuration from a direct to a parallel one with two non-acoustic sensors measures might improve the system attenuation capabilities in presence of unsynchronized propellers motion.
An experimental implementation of the obtained configuration can be carried out in order to perform a comparison with the numerical results. Deviations are foreseen due to real life effects, in particular the pressure gradients in the loudspeaker vicinity are expected to cause a performance degradation on the control system [48]. The simulated loudspeaker near-field might be corrected on the base of measurements to compensate for this effect (Celestinos [23]). Another aspect to be studied is the head acoustics as well, by means of the introduction of a mannequin or a person. The computational burden of this control solution should be sustainable by medium cost current technology: the filters length has been kept quite low while the control sampling frequency can be modified in a more flexible way in a real life application with respect to the one set for this activity. Moreover, a single reference microphone has been used. However, for practical applications the secondary sources signal computation and filters updating must be fast enough to guarantee the control is not delayed with respect to the problem physics, which could be a troublesome aspects in small reverberant enclosures. This suggest that a suitable environment should be considered in order to check for the causality constraint performing realistic experimental testing. In addition, all the audio chain transfer functions will affect the secondary paths identification while measurement errors are expected to degrade the system performances. All these aspects may be recorded and used to critically evaluate the reliability of the proposed numerical simulation as an analysis tool for the preliminary design of an active noise control system.

Appendix A

Frequency estimation algorithms

Narrowband ANC systems heavily rely on the quality of the estimation of the frequency content of the noise signal. In particular, when the noise spectrum basically consists in one predominant frequency and its multiples embedded in broadband noise, the problem might be reduced in finding the signal fundamental frequency behavior in time. Different approaches for the estimation of the fundamental frequency (also known as pitch estimation / tracking / detection) can be found in literature.
The most simple approach is the pulse counting. It is based on the fact that signal periodicity is associated to a zero crossing. An input frequency can then be estimated as

$$f = \frac{1}{2\ CT} \tag{A.1}$$

where CT is the time between two consecutive signal zero crossing. This method can easily be implemented for DSP applications but it heavily suffers from noise perturbation and does not perform well in presence of multiple harmonics contributions
Another class of time domain methods for pitch estimation are based on the autocorrelation ([57]). Their name derives from the fact that a periodicity in the signal is associated to a maximum in its autocorrelation function. In particular, the original method is based on finding an estimate of the fundamental period τ by minimization of the expected value of the squared error $e(n)^2$, where

$$e(n) = x(n) - x(n - \tau) \tag{A.2}$$

A different approach is comb filtering, which is based on the minimization of the mean squared error [58]. Another variation of the autocorrelation method more suitable for real-time implementation is the AMDF algorithm [57], which requires no multiplication. These approaches still cope badly with multiharmonic and noisy signals. An improved autocorrelation method is the YIM method, described in [59]. Other options in time domain are based on Hilbert transform, Haar wavelet, and generalized pencil of function (GPOF) [60]. Adaptive frequency tracking is also an option described in [61] and [62]. Frequency domain based methods typically provide better results in terms of estimation accuracy and robustness with respect to noise but are indeed limited by the computational cost of the FFT implementation, so suitable schemes for its calculation must be considered. An efficient algorithm for DSP implementation is the sliding FFT described in [63]. Some possible approaches for IF estimation are the interpolated fast Fourier transform (IFFT),the iterative weighted phase averager (IWPA) and the ESPRIT method [65].
Parametric estimation are also an option and are described in [58] and [66]. They include Maximum Likelihood Method (MLM, or Non Linear Least Squares Method, NLS), Recursive Bayesian methods, and harmonic summation. The latter in particular might represent a convenient choice for real time fast implementation. In order to estimate an harmonic multicomponent signal $x(n)$, a periodic model of it is defined in the following form:

$$s(n, \boldsymbol{\theta}) = \sum_{l=1}^{L} A_l \; cos(l\omega_0 n + \phi_l) \tag{A.3}$$

With $\boldsymbol{\theta} = [A_1 ... A_L, \phi_1 ... \phi_L, \omega_0]$, where A_i, ϕ_i and ω_0 are the unknown amplitudes, phases and fundamental frequency respectively of the signal. L is the model order (which must be known a priori) while n is the discrete time index. The estimation error is defined as

$$e(n) = x(n) - s(n, \boldsymbol{\theta}) \tag{A.4}$$

In order to estimate $\boldsymbol{\theta}$, a least square based estimation can be employed finding $\hat{\boldsymbol{\theta}}$ minimizing the cost function

$$J(\boldsymbol{\theta}) = \sum_{n=0}^{N-1} |e(n)|^2 \tag{A.5}$$

This approach is quite costly in this form. Applying Parseval's theorem the cost function can be rewritten as:

$$\lim_{N\to\infty} \sum_{n=0}^{N-1} |e(n)|^2 = \frac{1}{2\pi} \int_{-\pi}^{\pi} |E(\omega)|^2 d\omega \tag{A.6}$$

Since the model signal is a sum of cosines, the error expression in frequency domain is:

$$E(\omega) = X(\omega) - 2\pi \sum_{l=1}^{L} [\alpha_l \delta(\omega - \omega_0 l) + \alpha_l^* \delta(\omega + \omega_0 l)] \tag{A.7}$$

with $\alpha_l = A_i \frac{e^{j\phi}}{2}$. These coefficients depending on amplitudes and phases can be estimated as

$$\hat{\alpha_l} = \frac{1}{2\pi} X(\omega_0 l) \tag{A.8}$$

Inserting this value in $J(\boldsymbol{\theta})$ yields

$$J(\omega_0) = \frac{1}{2\pi} \int_{-\pi}^{\pi} |X(\omega)|^2 d\omega - \frac{1}{\pi} \sum_{l=1}^{L} |X(\omega_0 l)|^2 \tag{A.9}$$

This leads to the conclusion that ω_0 can be estimated as the frequency maximizing the function

$$J_{\omega_0} = \sum_{l=1}^{L} |X(\omega_0 l)|^2 \tag{A.10}$$

Thus harmonic summation requires a finite amount of data on which compute the DFT at certain spectral lines only. This can be efficiently implemented on cheap hardware architecture.
A shifting FFT algorithm has been used in subsect. 2.2.4 to provide an estimate of the input signal instantaneous frequency. It simply consists in the extraction of the higher frequency content by computing a FFT on time-shifting samples of constant length N. The frequency estimate can be evaluated for each sample window by means of harmonic summation based on a customized frequency grid ranging from a minimum expected value to a maximum one with a desired accuracy. A similar spectrum peak detection - based algorithm can be found in [64].

Bibliography

[1] L. L. BERANEK, "Acoustics", American Institute of Physics, 1993.

[2] S. JOHANSSON, "Active Noise Control in Aircraft - Algorithms and Applications", Ph.D Thesis at University of Karlskrona/Ronneby, 1998.

[3] R.R. LEITCH and M.O. TOKHI, "Active noise control systems", IEE Proceedings, Vol. 134, Pt. A, No. 6, June 1987.

[4] S. M. KUO and D. R. MORGAN, "Active Noise Control: A Tutorial Review", Proceedings of the IEEE, VOL. 87, NO. 6, June 1999.

[5] A. GUPTA, S. YANDAMURI and S. M. KUO, "Active vibration control of a structure by implementing filtered-X LMS algorithm", Noise Control Eng. J. 54 (6), pp : 396-405, 2006.

[6] R.ANDRIANI, "Dispense del corso di Motori Per Aeromobili", Politecnico di Milano.

[7] L.DOZIO and G.L.GHIRINGHELLI, "Noise & Vibrations : Passive and active methods for internal noise", Postgraduate Course in Rotary Wing Technologies at Politecnico di Milano.

[8] S.M.KUO and D.R.MORGAN, "Active Noise Control Systems: Algorithms and DSP implementations", John Wiley & Sons, 1st Edition, 1996.

[9] L.PIRODDI, "Active Noise Control", Ph.D course lecture slides at Politecnico di Milano, 2015.

[10] R. T. GORDON and W. D. VINING, ACTIVE NOISE CONTROL: A REVIEW OF THE FIELD, American Industrial Hygiene Association Journal, 53(11), pp: 721–725, 1992.

[11] S.J. ELLIOTT and M.E. JOHNSON, "Radiation modes and the active control of sound power", J. Acoustical Society of America 94 (4), pp: 2194-2204, October 1993.

[12] O. TOKHI and S. VERES,"Active Sound and Vibration Control : theory and applications", The Institution of Electrical Engineers, 2002.

[13] D.A.RUSSELL, "Acoustic monopoles, dipoles, and quadrupoles: An experiment revisited", American Journal of Physics 67(8), pp: 660-664 , August 1999.

[14] V. C HENRIQUEZ and P. JUHL, Course slides in geometrical acoustics :"The Boundary Element Method", EAA winter school.

[15] M.VORLANDER, "Auralization : fundamentals of acoustics, modelling, simulation, algorithms and acoustic virtual reality", Springer, 2007.

[16] A. DE FENZA, "EXPERIMENTAL AND NUMERICAL ESTIMATION OF DAMPING IN COMPOSITE PLATES WITH EMBEDDED VISCOELASTIC TREATMENTS", Ph.D. in Aerospace Engineering at University of Naples FEDERICO II, November 2011.

[17] J.Q.SUN, M.R. JOLLY and M. A.NORRIS, "Passive, Adaptive and Active Tuned Vibration Absorbers-A Survey", Journal of Mechanical Design, 117(B), 234, 1995.

[18] R. I. WRIGHT and M. R. F KIDNER, "Vibration Absorbers: A Review of Applications in Interior Noise Control of Propeller Aircraft", Journal of Vibration and Control, 10, pp: 1221-1237, 2004.

[19] B. WIDROW, J.R. GLOVER and J.R ZEIDLER, "Adaptive noise cancelling: Principles and applications",Proceedings of the IEEE, 63(12), 1975.

[20] S.M. KUO and D. R. MORGAN, "Active noise control: a tutorial review", Proceedings of the IEEE, 87(6), pp: 943–975, 1999.

[21] J.R. GLOVER, "Adaptive noise canceling applied to sinusoidal interferences", IEEE Transactions on Acoustics, Speech, and Signal Processing 25(6), pp: 484–491, 1977.

[22] Y. XIAO, A. IKUTA, L. MA, and K.KHORASANI, "Stochastic Analysis of the FXLMS-Based Narrowband Active Noise Control System", IEEE Transactions on Audio, Speech, and Language Processing, 16(5), pp: 1000–1014, 2008.

[23] A. CELESTINOS; "Low frequency sound field enhancement system for rectangular rooms, using multiple loudspeakers", Ph.D Thesis at Aalborg Universitet, 2007.

[24] F. ASLAN and R. PAUROBALLY, "Modelling and simulation of active noise control in a small room", Journal of Vibration and Control, pp: 1-12, 2016.

[25] M. MIROSLAW, " Acoustics of small rectangular rooms: Analytical and numerical determination of reverberation parameters", Institute of Fundamental Technological Research, Polish Academy of Sciences, 2017.

[26] S.SILTANEN, T. LOKKI and L.SAVIOJA, "Rays or Waves? Understanding the Strengths and Weaknesses of Computational Room Acoustics Modeling Techniques", Proceedings of the International Symposium on Room Acoustics, ISRA 2010.

[27] L.SAVIOJA, "Modeling Techniques for Virtual Acoustics", Ph.D Thesis at Helsinki University of Technology, 1999.

[28] S.GEDNEY, "Introduction to the Finite-Difference Time-Domain (FDTD) Method for Electromagnetics", Synthesis Lectures on Computational Electromagnetics, 2011.

[29] K. KOWALCZYK and M.V. WALSTIJN, "A comparison of nonstaggered compact FDTD schemes for the 3D wave equation", acoustics Speech and Signal Processing (ICASSP), 2010 IEEE International Conference.

[30] K.S. KUNZ and R.J. LUEBBERS, "The Finite Difference Time Domain Method for Electromagnetics", CRC Press, 1993.

[31] J. SHEAFFER, M.V. WALSTIJN and B.FAZENDA "A physically-constrained source model for FDTD acoustic simulation", 15th Intl. Conference on Digital Audio Effects (DAFx-12), September 2012.

[32] D.T.MURPHY, A.SOUTHERN and L.SAVIOJA, "Source excitation strategies for obtaining impulse responses in finite difference time domain room acoustics simulation", Applied Acoustics, Volume 82, pp: 6-14, August 2014.

[33] D. ORLIS, M.GIOUVANAKIS, C. SEVASTIADIS and G. PAPANIKOLAOU, "Simulation of active low frequency noise control in closed spaces using the FDTD method ", Euronoise 2018 - Conference.

[34] J. BORWICK , "Loudspeaker and Headphone Handbook", Routledge, 3rd edition, 2001.

[35] H. JEONG and Y. W. LAM , "FDTD modelling of frequency dependent boundary conditions for room acoustics", Proceedings of 20th International Congress on Acoustics, ICA 2010.

[36] Y. KIM, "Sound Propagation: An Impedance Based Approach", John Wiley & Sons (Asia), 1st edition, 2010.

[37] H. KUTTRUFF, "Room Acoustics", Spon Press, Fifth Edition, 2009.

[38] M. YAIRI, T. KOGA, K. TAKEBAYASHI and K. SAKAGAMI, " Transmission of a spherical sound wave through a single-leaf wall: Mass law for spherical wave incidence ", Applied Acoustics 75, pp: 67-71, 2014.

[39] R.PARISI, "Dispense del corso di Metodi numerici per l'acustica", Sapienza Università di Roma.

[40] J.E. MARTE and D. W. KURTZ , "A Review of Aerodynamic Noise From Propellers, Rotors, and Lift Fans", National Aeronautics and Space Administration Technical Report 32-1462, Jet Propulsion Laboratory at California Institute of Technology Pasadena, California, 1970.

[41] D. MILJKOVIC, J. IVOSECIC and T. BUCAK, "Two Vs. Three Blade Propeller - Cockpit Noise Comparison", 5th Congress of Alps-Adria Acoustics Association, Petrčane, Croatia 12-14 September 2012.

[42] R.I.WRIGHT and M.R.KIDNER, "Vibration Absorbers : A Review of Applications in Interior Noise Control of Propeller Aircraft", Journal of Vibration and Control 10, pp: 1221-1237, 2004.

[43] M. F. CATAPAN, M. L. OKIMOTO, M. V. BOAS and R. WALDHAUER, "Statistical Analysis of the Height of Human Head in the Use of Ballistic Helmets", Proceedings of the 5th International Conference on Applied Human Factors and Ergonomics AHFE 2014, Kraków, Poland, 19-23 July 2014.

[44] A. N. VASAVADA, J. DANARAJ and G. P.SIEGMUND, "Head and neck anthropometry, vertebral geometry and neck strength in height-matched men and women", Journal of Biomechanics 41, pp: 114–121, 2008.

[45] G. DROANDI, "Wing-rotor aerodynamic interaction in tiltrotor aircraft", Ph.D Thesis at Politecnico di Milano, 2014.

[46] J. GARCIA-BONITO, S. J. ELLIOTT and C.C BOUCHER," Generation of zones of quiet using a virtual microphone arrangement", The Journal of the Acoustical Society of America, 101(6), pp: 3498–3516, 1997.

[47] J.F. ABBOTT, "Acoustical design criteria for active-noise control systems", Proc. ICASSP, Vol. V, pp: 630-633, 1993.

[48] P. JOSEPH, S.J. ELLIOTT and A. P. NELSON, "Near Field Zones of Quiet", Journal of Sound and Vibration, 172(5), pp: 605–627, 1994.

[49] A. DAVID and S. J. ELLIOTT, "Numerical studies of actively generated quiet zones", Applied Acoustics, 41(1), pp: 63–79, 1994.

[50] ANSI Standards S1.4-1983 and S1.42-2001.

[51] J.J.LOPEZ, D.CARNICERO, N. FERRANDO and J. ESCOLANO, "Parallelization of the finite-difference time-domain method for room acoustics modelling based on CUDA", Mathematical and Computer Modelling Volume 57, pp: 1822-1831, April 2013.

[52] L. SAVIOJA, "Real-time 3D finite-difference time-domain simulation of low - and mid - frequency room acoustics", Proceeding of the 13th International Conference on Digital Audio Effects (DAFx-10), Graz, Austria, September 6-10, 2010.

[53] H.E.V. GIERKE, "Acoustic absorption coefficients of human body surfaces", BIOMEDICAL LABORATORY -AEROSPACE MEDICAL RESEARCH LABORATORIES - AEROSPACE MEDICAL DIVISION-AIR FORCE SYSTEMS COMMAND, WRIGHT-PATTERSON AIR FORCE BASE, OHIO TECHNICAL DOCUMENTARY REPORT No. MRL-TDR-62-36, April 1962.

[54] J. SHRAGGE, "Solving the 3D acoustic wave equation on generalized structured meshes: A finite-difference time-domain approach", Geophysics 79(6), pp: 1-16, November 2014.

[55] R. H. KWONG and E. W. JOHNSTON, " A variable step size LMS algorithm ", IEEE Transactions on Signal Processing, 40(7), pp: 1633–1642, 1992.

[56] F. YANG , Y. CAO, M. WU, F. ALBU and J. YANG, "Frequency-Domain Filtered-x LMS Algorithms for Active Noise Control: A Review and New Insights", Applied Sciences, 2018.

[57] L. TAN and M. KARNJANADECH, "Pitch detection algorithm: autocorrelation method and AMDF", January 2003.

[58] J. K. NIELSEN, T. L. JENSEN, J. R. JENSEN, M. G. CHRISTENSEN and S. H. JENSEN, "Fast and Statistically Efficient Fundamental Frequency Estimation", ICASSP 2016.

[59] H. KAWAHARA and A.D. CHEVEIGNE, "YIN, a fundamental frequency estimator for speech and music", J. Acoust. Soc. Am.111(4), pp: 1917-1930, April 2002.

[60] J. C. GOSWAMI and A. E. HOEFEL, "Algorithms for estimating instantaneous frequency", 2004.

[61] B. BOASHASH, "Estimating and Interpreting the Instantaneous Frequency of a Signal-Part 2: Algorithms and Applications", Proceedings of the IEEE, VOL. 80, NO. 4, April 1992.

[62] J. VAN ZAEN, "Efficient Schemes for Adaptive Frequency Tracking and their Relevance for EEG and ECG", Ph.D Thesis at ÉCOLE POLYTECHNIQUE FÉDÉRALE DE LAUSANNE, 2012.

[63] E.JACOBSEN, "Understanding and Implementing the Sliding DFT ", https://www.dsprelated.com/showarticle/776.php, 2015.

[64] E.JACOBSEN and P. KOOTSOOKOS, "Fast, Accurate Frequency Estimators", IEEE SIGNAL PROCESSING MAGAZINE [123], May 2007.

[65] I. SANTAMARIDA, C. PANTALEON and J. IBANEZ, "A comparative study of high-accuracy frequency estimation methods", Mechanical Systems and Signal Processing 14(5), pp: 819-834, 2000.

[66] M. LINDFORS, "Frequency Tracking for Speed Estimation", Ph.D Thesis at Linkoping University, 2018.

[67] L. COHEN, "Time-frequency analysis", Prentice-Hall PTR, 1995.

[68] https://www.globalsecurity.org/military/library/policy/army/fm/55-450-2/Ch1.htm

[69] R. GOOSSENS, "Biomechanical analysis of the dimensions of pilot seats in civil aircraft", Applied Ergonomics 31(1), pp: 9-14, 2000.

[70] J.SAARELMA, "Finite-difference time-domain solver for room acoustics using graphics processing units", Master Thesis at Aalto University, 2013.

[71] R. C. RUMPF, "EM Analysis Using FDTD", Course lectures at University of Texas at El Pas, 2018.